

PENNSSTATE



Pennsylvania State University

---

Engineering Science and Mechanics

**2013**

**ESM TODAY**

Abstract Book

# PRESENTATIONS

# HIGH RESISTIVITY AND HIGH TCR VANADIUM OXIDE THIN FILMS FOR INFRARED IMAGING PREPARED BY BIAS TARGET ION BEAM DEPOSITION

*Yao Jin,<sup>1</sup> Thomas N. Jackson,<sup>2,3</sup> and Mark W. Horn<sup>1,2</sup>*

<sup>1</sup>Department of Engineering Sciences, Penn State University, University Park, PA 16802, USA

<sup>2</sup>Materials Research Institute, Penn State University, University Park, PA 16802, USA

<sup>3</sup>Department of Electrical Engineering, Penn State University, University Park, PA 16802, USA

As the main imaging materials for uncooled microbolometers, Vanadium oxide (VOx) thin films have been intensively studied for several years due to their low resistivity, high temperature coefficient of resistivity (TCR) and low 1/f noise. VOx thin films for commercial infrared imaging cameras have been exclusively prepared by ion beam deposition. Our group has studied pulsed DC reactive sputtered VOx thin films with imaging grade resistivity in the range of 0.1 to 10 ohm-cm and TCR from -2%/K to -3%/K.

In this study, a new biased target ion beam deposition (BTIBD) tool is first reported to prepare VOx thin films. In this system, Ar ions with energy about 25eV generated remotely and metallic vanadium targets are negatively biased independently for sputtering. This novel deposition tool is used to prepare VOx thin films with

different composition and electrical properties by manipulating different processing parameters such as ion beam energy, processing pressure, source Ar flow rate, oxygen flow rate, target bias voltage, target pulse width and pulse period. Oxygen partial pressure is monitored by a residual gas analyzer (RGA) to control depositions. The controllability of nanocomposition and electrical properties of VOx thin films is compared between pulsed DC magnetron sputtering and biased target ion beam sputtering. High TCR (>-5%/K) and high resistivity in the range of 1000 to 100000 ohm-cm VOx thin films have been prepared, which may be useful for next generation through-film imaging layers in uncooled microbolometers. Controlled addition of alloy materials and their effects on electrical properties of VOx thin films are also reported.

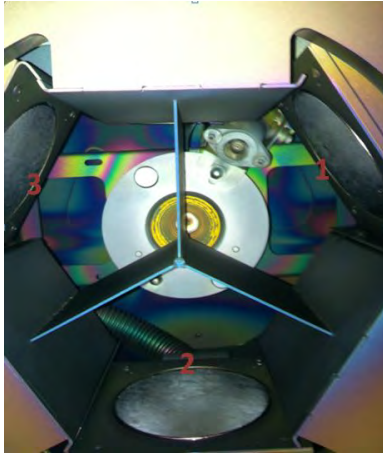


Fig. 1 Picture of BTIBD system process chamber

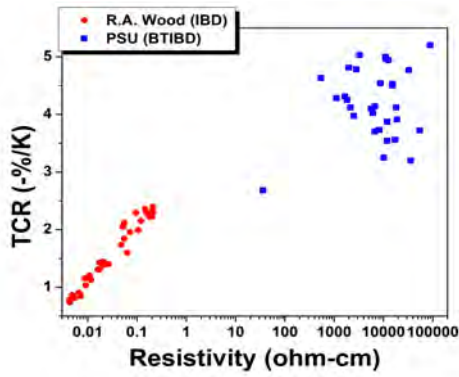


Fig. 2 TCR vs. Resistivity data of VOx thin films compared between Wood's IBD and BTIBD.

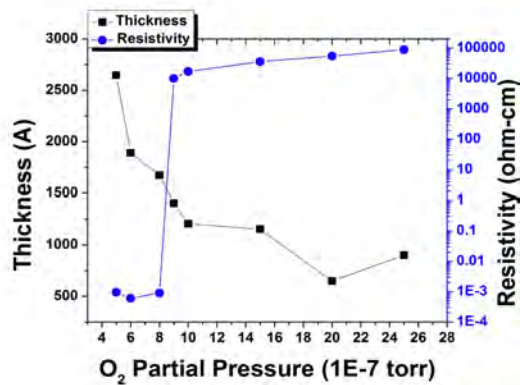


Fig. 3 At certain parameters, BTIBD prepared VOx thin films' thickness and resistivity change as a function of oxygen partial pressure.

## REFERENCES:

- [1] R.A.Wood, "Monolithic Silicon Microbolometer Arrays", *Semiconductors and Semimetals* 47, 1997, pp. 43.

## High-efficiency cells separation using novel acoustic tunnel

*Xiaoyun Ding and Tony Jun Huang*

Engineering Science and Mechanics Department, Penn State University, PA

To date, many methods capable of particle and cell separation in microfluidic systems, such as centrifugal methods [1], magnetic force [2], hydrodynamic force, dielectrophoretic (DEP) [3], and bulk acoustic waves (BAW) [4] have been developed. Previously we demonstrated continuous particle separation through standing surface acoustic wave (SSAW)-induced acoustophoresis in a microfluidic channel [5]. However, the separation efficiency in our previous studies [5] is only 85%. Built upon our previous work, here we demonstrated a tilted interdigital transducer (TIDT) based particle separation technique that achieves a separation efficiency of 98% or higher.

The TIDT-based particle separation device (Fig. 1) consists of a polydimethylsiloxane (PDMS) channel and a piezoelectric substrate with a pair of tilted interdigital transducers (IDTs). The channel locates in between the two IDTs with a specific angle so that there is an angle between the flow direction and the 1-dimensional (1D) standing wave. Applying AC signals to the IDTs generated two series of identical-frequency surface acoustic waves (SAWs) which propagated in opposite directions toward the channel. The constructive interference of these two SAWs resulted in a SSAW in the area where the microchannel was bonded. Fig. 2 is an optical image of the TIDT-based particle separation device. When the particles enter the SSAW field, they will be pushed to the parallel 1D pressure nodes. Simultaneously, the hydrodynamic force will push the particles along the flow direction, which has an angle to the pressure node. Since the acoustic force is proportional to the particle size, by optimizing the amplitude of SAW and the flow rate, we can ensure that the acoustic force is large enough to confine big (10  $\mu\text{m}$ ) particles in the pressure node while allowing the small (2  $\mu\text{m}$ ) particles go through the standing SAW region with the main flow.

Figure 3 shows the separation process of 2 and 10  $\mu\text{m}$  particles. When the SSAW field is off, both small and big particles are mixed and follow the flow to lower outlet channel (Fig. 3 a, b). When the SSAW field is on, big particles are extracted from the main stream (Fig. 3c) and move to upper channel (Fig. 3d), while the small particles remain in the original flow and go to lower outlet channel. The separation efficiency is defined by the ratio of particles collected in the outlet to the particles in the inlet. Our preliminary experiments demonstrate a separation efficiency of 98% for big particles and a separation efficiency of 100% for small particles.

Our TIDT-based particle separation method features high separation efficiency (98%), low power consumption, easy fabrication and handling, low cost, versatility, and rapid response time. These characteristics make our method promising in many biomedical and chemical applications.

**Word count: 444**

### Reference:

1. "Continuous flow separations in microfluidic devices," N. Pamme, *Lab Chip*, **7**, 1644–1659. (2007)
2. "Label-Free Cell Separation Using a Tunable Magnetophoretic Repulsion Force" F. H. Shen, Hwang, Y.K. Hahn, J-K Park (2012). *Analytical chemistry*, dx.doi.org/10.1021/ac201505j.
3. "Continuous separation of breast cancer cells from blood samples using multi-orifice flow fractionation (MOFF) and dielectrophoresis (DEP)," Moon H-S et al. *Lab on a chip* **11**:1118-25. (2011).
4. "Continuous separation of cells and particles in microfluidic systems," A. Lenshof and T. Laurell, *Chem Soc Rev*, **39**, 1203–1217. (2010).
5. "Continuous particle separation in a microfluidic channel via standing surface acoustic waves (SSAW)," J. Shi, H. Huang, Z. Stratton, Y. Huang, and T. J. Huang, *Lab Chip* **9**, 3354-3359 (2009).

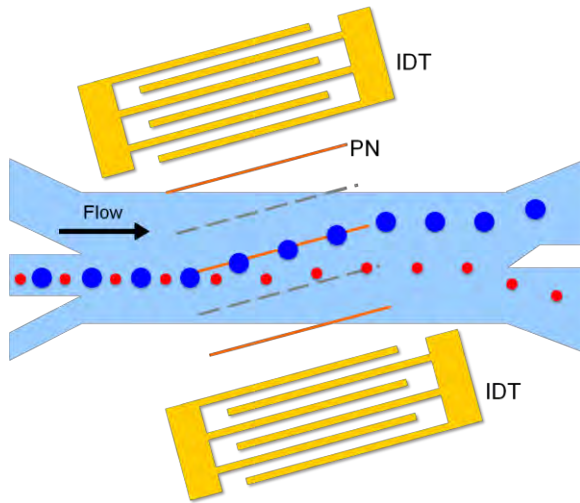


Figure 1: Schematic and working mechanism of the TIDT-based particle separation device.

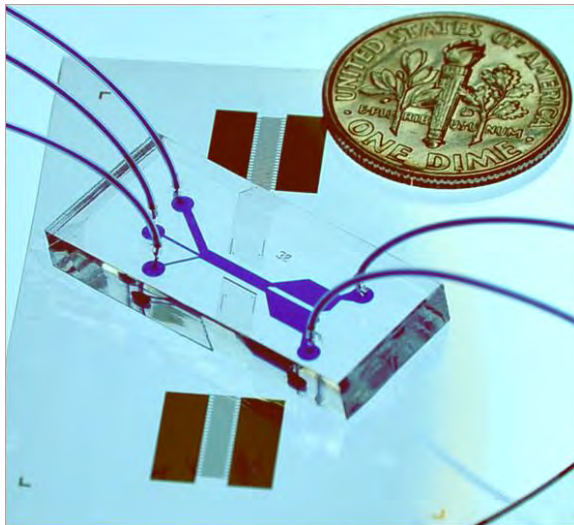


Figure 2: An optical image of the TIDT-based particle separation device.

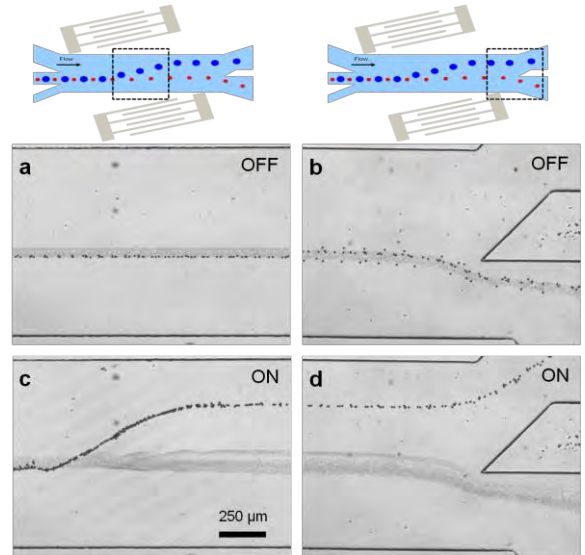


Figure 3: The trajectories of particles when the power is off (a and b) and on (c and d) at the SSAW region (a and c) and outlet (b and d).

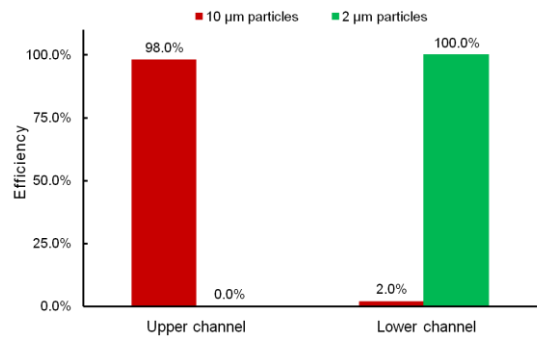


Figure 4: Separation efficiency of particles in each outlet channel based on preliminary results.

# SUPPRESSION OF CIRCULAR BRAGG PHENOMENON IN CHIRAL SCULPTURED THIN FILMS PRODUCED WITH SIMULTANEOUS ROTATION AND ROCKING OF SUBSTRATE DURING SERIAL BIDEPOSITION

*Stephen E. Swiontek, Jian Xu, and Akhlesh Lakhtakia*

Department of Engineering Science and Mechanics, Penn State, PA-16802, USA

**Introduction.** Chiral sculptured thin films (CSTFs) produced by substrate rotation during physical vapor deposition (PVD) exhibit the circular Bragg phenomenon, whereby normally incident left- and right-circularly polarized plane waves are discriminated in a spectral regime called the circular Bragg regime [1]. Theory had predicted that substrate rocking, in synchrony with substrate rotation, during deposition could suppress the propensity to exhibit the circular Bragg phenomenon [2]. Therefore, CSTFs of zinc selenide (ZnSe) were fabricated with/without substrate rocking, and their transmittance spectrums for incident linearly and circularly polarized plane waves were measured. With sufficient rocking amplitude, the discrimination between incident left- and right-circularly polarized light nearly vanished, whereas a Bragg phenomenon for all normally incident plane waves was observed. Thus, chiral STF technology can be used to produce both ordinary and circular-polarization Bragg filters.

**Fabrication of STFs with/without rocking.** During the deposition of a chiral STF, the substrate is tilted so that the collimated vapor flux makes a fixed angle  $\chi_v \in (0^\circ, 90^\circ]$  with respect to the substrate plane. In addition, either the substrate is rotated at a uniform rate during deposition or it is rotated in an incremental step-wise fashion, about a central normal axis which is called serial bideposition (SBD) and enhances the local linear birefringence. In SBD, sequential subdeposits are made either from two oppositely oriented source boats or from a real source boat and one simulated by a  $180^\circ$  rotation of the substrate [3]. Once the two subdeposits have been made, the substrate is incrementally rotated by a small

angle  $\Delta \xi$  about the central normal axis and two new subdeposits are made, and so on. The SBD procedure was adapted to grow tilt-modulated CSTFs for this work. ZnSe chiral STFs were fabricated using the serial bideposition version of PVD with/without synchronized rocking. Figure 1 is a schematic of the substrate motor which sinusoidally rocked the substrate during rotation. Transmittance spectrums for linear and circular polarized incident light were measured. Figure 2 shows the optical setup for measuring those transmittance spectrums. The collimated vapor flux was directed at  $25^\circ$  with respect to the substrate plane, which was rotated at 0.5 rpm in vacuum at  $1.5 \times 10^{-5}$  Torr. The substrate was rocked with the rocking period and the rotation period being the same in duration. All STFs produced had nine periods, each period of thickness 330 nm.

**Results.** The circular Bragg phenomenon was gradually de-emphasized as the amplitude  $\delta_v$  of tilt modulation increased, and the discrimination between the two circular polarization states of the incident plane wave became less significant as  $\delta_v$  increased as seen in Figures 3. Instead, a simple Bragg phenomenon that does not distinguish greatly between the two linear-polarization states emerged. Scanning-electron micrographs confirmed that structural chirality is maintained even when the substrate is rocked in addition to rotation as seen in Figure 4. At moderate values of  $\delta_v/\chi_v$ , the structural periodicity of the helical morphology is clearly evident, which is not normally seen in SBD-deposited chiral STFs with  $\delta_v = 0^\circ$ . At much higher values of  $\delta_v/\chi_v$ , the morphology suggests that columns resemble twisted ribbons.

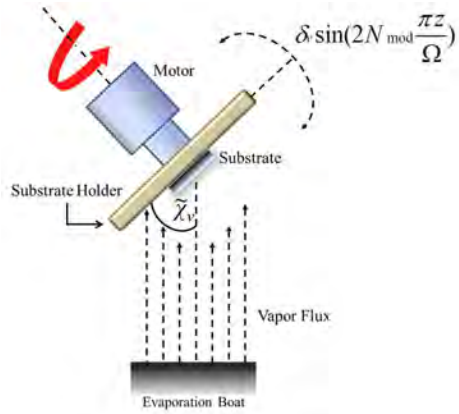


Figure 1: Schematic of the substrate holder programmed for a sinusoidally varying vapor flux angle with a mean value  $\tilde{\chi}_v$ , maximum  $\tilde{\chi}_v + \delta v$ , and minimum  $\tilde{\chi}_v - \delta v$ .

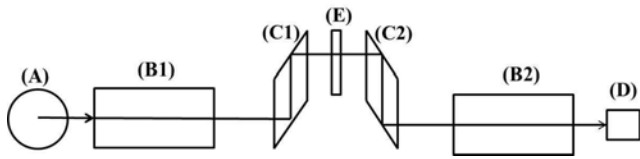


Figure 2: Schematic beam path used to measure optical transmittances

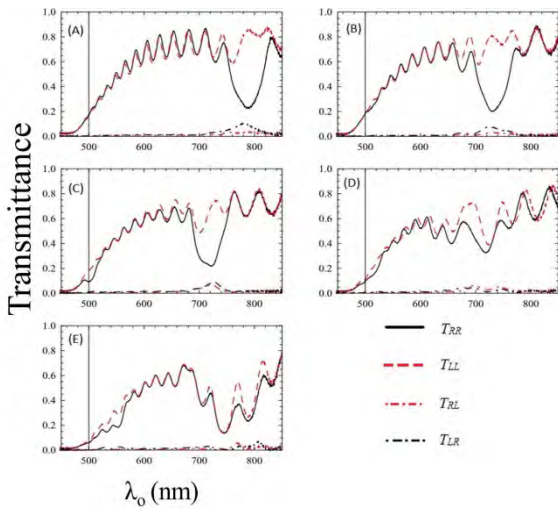


Figure 3: Circular transmittances for regular chiral STFs and tilt-modulated chiral STFs

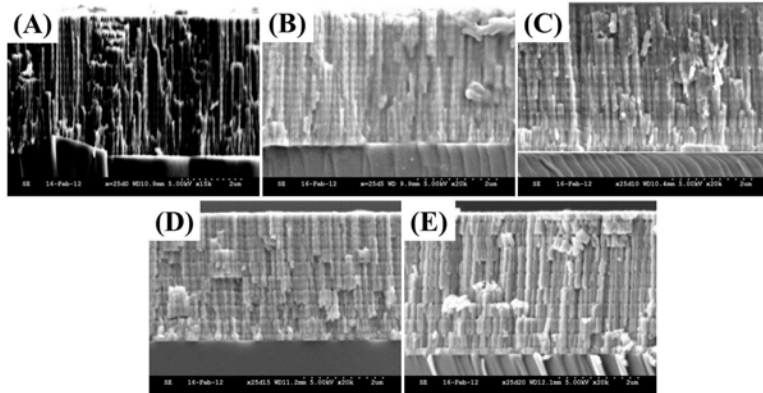


Figure 4: SEM images of chiral STFs (A) and tilt-modulated chiral STFs (B-E).

**References:**

- [1] A. Lakhtakia and R. Messier, *Sculptured Thin Films: Nanoengineered Morphology and Optics*, SPIE Press, Bellingham, WA, USA (2005).
- [2] J. A. Polo Jr. and A. Lakhtakia, “Tilt-modulated chiral sculptured thin films: an alternative to quarter-wave stacks,” *Optics Communications* **232**, 13–21 (2004).
- [3] I. Hodgkinson, and Q. h. Wu, “Serial bideposition of anisotropic thin films with enhanced linear birefringence,” *Applied Optics* **38**, 3621–3625 (1999).

# TRANSPORT OF DROPLETS AND GELS ON NANO-PPX SURFACE

Koray Sekeroglu<sup>1</sup>, Melik Demirel<sup>1,2,3</sup>

<sup>1</sup>Department of Engineering Science and Mechanics, Penn State University, University Park, Pennsylvania 16802, USA.

<sup>2</sup>Materials Research Institute, Pennsylvania State University, University Park, Pennsylvania 16802, USA.

<sup>3</sup>Department of Bioengineering, Penn State University, University Park, Pennsylvania 16802, USA.

In nature, droplet transport mechanisms exist in animal and plant kingdoms. Butterfly wings directing water droplets opposite the body and ryegrass leaves releasing water droplets unidirectionally are common examples. Surface ratchets in these mechanisms are built with pinning and release functions that can guide water droplets directionally. Being inspired from nature, we fabricated unidirectional polymeric (poly(p-xylylene)) nanorods using oblique angle polymerization technique in *vacuo*. The resulting surface is used to directionally transport water droplets via vertical vibrations of nanofilm coated half-pipes. The polymeric surface ratchets are able to transport cargo such as microgels, fabricated by photolithography, encapsulated in water droplets. The propulsion of micro-liter water droplets in a single

direction occur due to anisotropic surface properties. We observed the experimental results in terms of the relation among the water drop volumes, vibration frequency, and water drop speeds. Vibration frequency was found to be inversely proportional to the drop volume, which has a top-speed in a specific frequency interval. Ultimately, water encapsulated microgels, coated by planar parylene, are smoothly transported along the nanofilm coated half-pipes. As a result, controlling physicochemical properties of the nanofilm surface, directed assembly of soft cargo (i.e. microgels) can be achieved on nanoscale surfaces. Transport and 3D assembly of water encapsulated-cell attached microgels holds a great promise for medical, tissue engineering, and pharmaceutical applications.

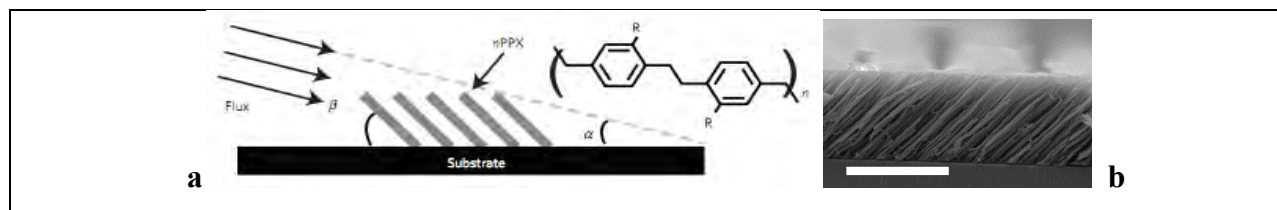


Fig1.a. Oblique angle deposition of parylene [3], b. SEM figure of deposited PPX on glass (Scale: 10 $\mu$ m) [1]

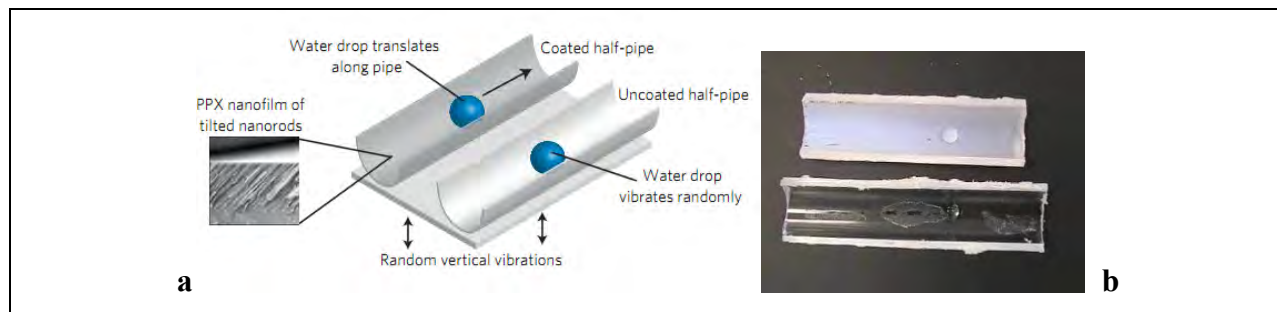


Fig2.a. Schematic representation of coated and uncoated half-pipes [3], b. Coated and uncoated half-pipes [3]

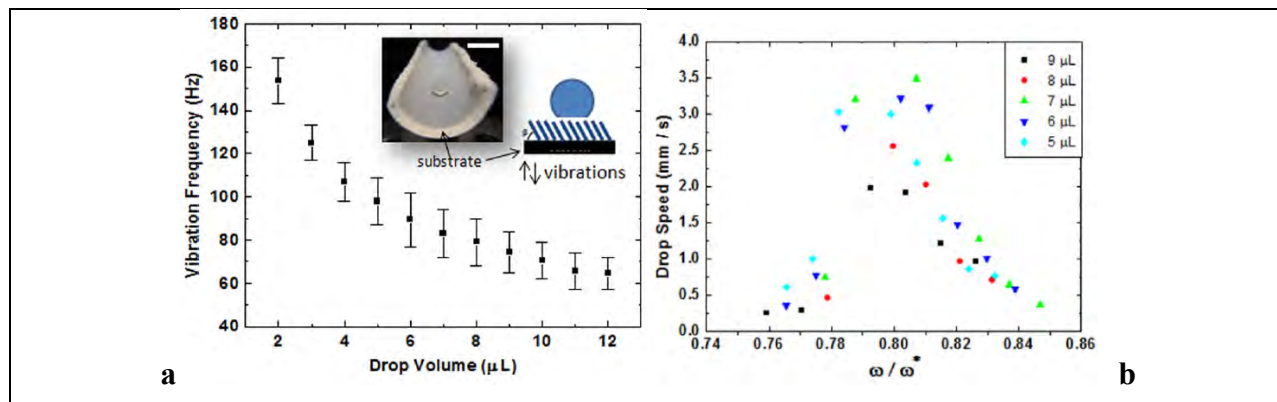


Fig3.a. Drop volume vs. vibrational frequency [2], b. Normalized vibration frequency vs. droplet speed [2].

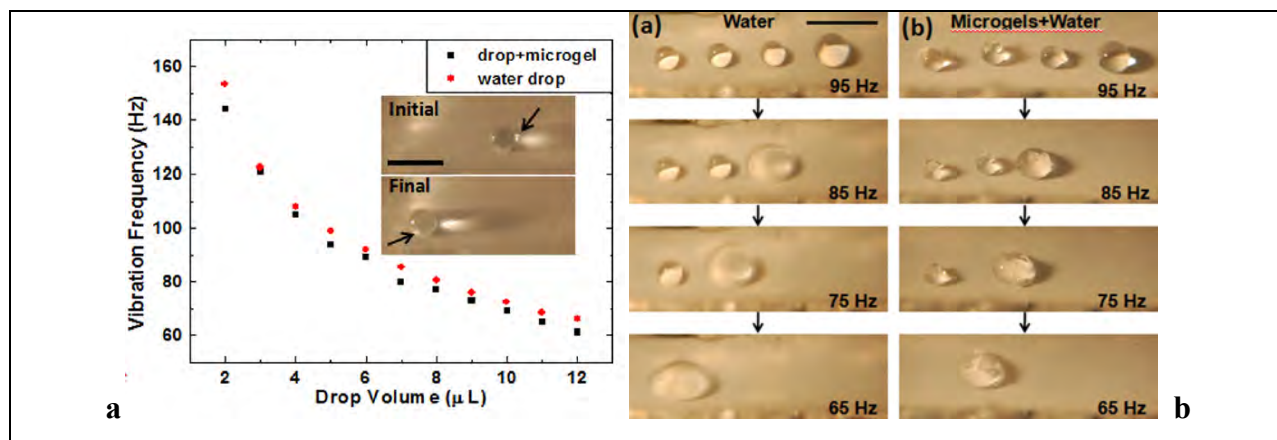


Fig4.a. Drop volume vs. vibrational frequency with microgels [2], b. Merging microgels into a single drop [2].

## REFERENCES

1. Hancock M.J., *Advanced Functional Materials*, **22**, 2223-2234 (2012).
2. Sekeroglu K. et al., *Applied Physics Letters*, **99**, 063703, (2011).
3. Malvadkar N.M. et al., *Nature Materials*, **9** (12), 1023 (2010).

# OPTIMAL CONTROL OF HUMAN DYNAMICS IN A VIRTUAL SHUFFLEBOARD GAME

Joseph M. Mahoney

PhD Candidate, Engineering Science and Mechanics, The Pennsylvania State University  
State College, PA USA

Sixteen subjects were recruited to participate in a virtual shuffleboard experiment. In this experiment, the subject manipulated a linear transducer that mapped their motion to a virtual environment that was projected onto a screen in front of them. The system can be seen in Fig. 1. By pushing the transducer, they are moving a shuffleboard cue on the screen, which in turn pushes a virtual puck. The subject's goal was to have the puck stop as close to the target line as possible. In the first version of the task, the puck was slowed simply by Coulomb friction. In the second version, there is a patch of ice after the target line that will cause the puck to stop farther from the target. For each version of the experiment, the subject repeated the task 250 times. The release position and -velocity of the puck was saved for each trial as well as the location where the puck stopped. The error,  $e$ , for each trial is calculated using Eq. 1.

$$e = x + v^2 - 1 \quad (1)$$

Here,  $x$  and  $v$  are normalized, unitless quantities and  $e$  is the error as a proportion of the total length to the target. A value of zero for  $e$  indicated hitting the target and it can be seen that there are a continuum of  $x$  and  $v$  values that will satisfy this. This collection of values that results in perfect performance is called the *Goal Equivalent Manifold* (GEM). A typical distribution of experimental data is shown in Fig. 2. In this figure, and for all subjects, it is observed that the *mean operating point* (MOP: the average  $x$  and  $v$  value across all trials) does not lie on the GEM. In fact, for the condition with ice, the MOP is, on average, farther from the GEM than the condition without ice.

An optimal controller is proposed to explain the location of a subject's MOP. For simplicity, a one-step update controller is employed as shown in Eq. 2:

$$\bar{x}_{k+1} = \bar{x}_k + \bar{u}_k + \bar{v}_k \quad (2)$$

Here, the next state,  $\bar{x}_{k+1}$  (pair of  $x$  and  $v$ ), is determined by the current state,  $\bar{x}_k$ , an input,  $\bar{u}_k$ , and a white Gaussian noise input,  $\bar{v}_k$ . The noise has a mean of zero and a covariance determined by the subject's empirical data. The value of the input at any step is found by minimizing a cost function,  $\Pi$ :

$$\min_{\bar{x}} \Pi = \underbrace{\eta P_x(\bar{x})^2 + \alpha e(\bar{x})^2 + \beta H^+[e(\bar{x})]}_{\Pi_S} + \underbrace{\gamma u_x^2 + \delta u_v^2}_{\Pi_D} \quad (3)$$

$P_x$  is the distance between an  $x$ -value and the  $x$ -value of the subject's POP.  $e$  is the error for the game type.  $H^+$  is the Heaviside function of the error.  $u_x$  and  $u_v$  are the  $x$ - and  $v$  inputs.  $\bar{x}$  is the vector of body-variables,  $(x, v)$ , at the next step. The cost function can be divided into the objective functions that govern the mean operating point ( $\Pi_S$ ) and the objective functions that govern the dynamics ( $\Pi_D$ ).

The estimation of the weights for each subject and scenario was done in two stages. First,  $\eta$ ,  $\alpha$  and  $\beta$  were estimated while  $\gamma$  and  $\delta$  were held at zero: the same as minimizing  $\Pi_S$  independently. Under this condition, the subject would aim to return to the Mean Operating Point after every trial and all fluctuations from the mean would be due only to additive noise in the system. Using a simulated annealing minimization, the weights were found that minimized the distance between the subject's empirically determined POP and the mean operating point found through simulation of 1000 trials (Eq. 4). The weight of  $P_x$  was arbitrarily fixed to one in this step to find a unique solution to the minimization. These weights were then normalized by their 2-norm to get the final estimated steady-state weights (Eq. 5). The normalization ensures that the strengths of the dynamic weights will be compared against a consistent strength of steady-state weights.

$$\underset{\alpha', \beta'}{\operatorname{argmin}} \left\| \underset{\bar{x}}{\operatorname{argmin}} E \left[ P_x(\bar{x} + \bar{v})^2 + \alpha' e(\bar{x} + \bar{v})^2 + \beta' H^+[e(\bar{x} + \bar{v})] \right] - \bar{x}_{POP} \right\| \quad (4)$$

$$(\eta, \alpha, \beta) = \frac{(1, \alpha', \beta')}{\|(1, \alpha', \beta')\|} \quad (5)$$

The ratios of  $\beta$  to  $\alpha$  that were estimated are shown in Fig. 3. The ratios are generally negative for **W** (trying to minimize undershooting) and slightly positive for **N** (trying to minimize overshooting). The variance of the subject's noise input correlates with the estimated weighting ratio as seen in Fig. 4.



**Fig. 1:** *Experimental set-up*

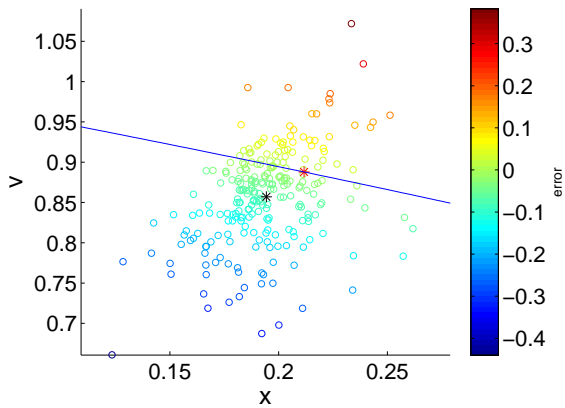


**Fig. 2:** *Typical trial-data distribution. The black star indicates the mean operating point, the blue line is the GEM and the red star is the closest point on the gem to the mean operating point. The coloration of the points indicates the error as calculated by Eq. 1*

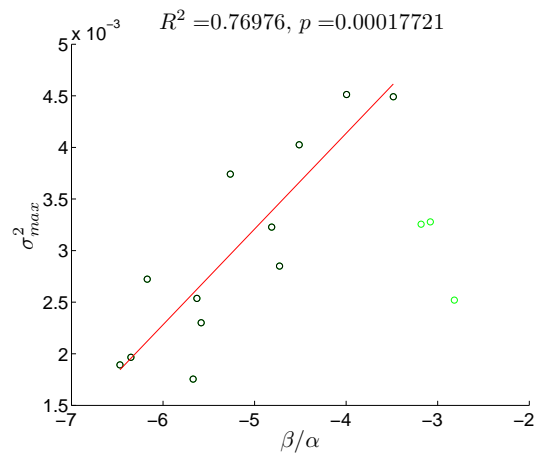


**Fig. 4:** *RMS of a subject's input noise correlated with the ratio of weights. In general, the higher the variance, the more effort a subject will place on not overshooting the target. Three outliers were removed for the linear correlation*

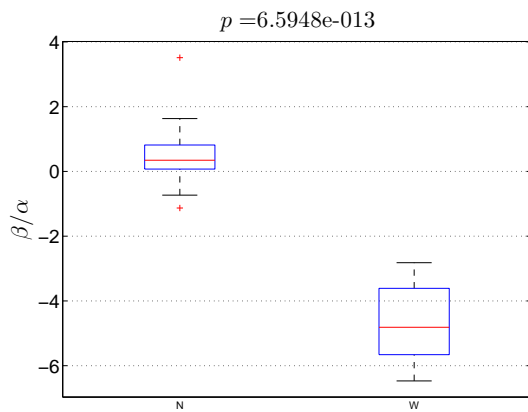


**Fig. 3:** *Ratio of weight on reducing overshooting to weight on reducing error. There is a significant difference in the means of the two conditions. Both the magnitude and sign changes between them.*

## THROUGH-FILM CONDUCTIVITY OF VOX THIN-FILMS FOR UNCOOLED IR IMAGING

*Hitesh A. Basantani,<sup>1,3</sup> Hang-Beum Shin,<sup>2</sup> Thomas. N. Jackson,<sup>2,3</sup> and Mark W. Horn<sup>1,3</sup>*

<sup>1</sup>Department of Engineering Sciences, the Pennsylvania State University, University Park, PA 16802, USA

<sup>2</sup>Department of Electrical Engineering, the Pennsylvania State University, University Park, PA 16802, USA

<sup>3</sup>Materials Research Institute, the Pennsylvania State University, University Park, PA 16802, USA

Uncooled IR bolometers form an integral part of thermal imaging cameras. Vanadium oxide material currently used for IR imaging has a resistivity between 0.1 and 1 ohm-cm and a TCR between  $-1.4\%K^{-1}$  to  $-2.4\%K^{-1}$ . Higher TCR materials are desired, however, such materials inevitably have higher resistivity and therefore higher electrical resistance in a lateral resistor configuration. A high resistance leads to an increase in the electrical (Johnson-Nyquist) noise of the bias-induced current, thereby limiting the performance of bolometers using high resistivity material. In this work, we propose the use of temperature dependent through-film conductivity as an alternate pixel structure design with lower Johnson noise when compared with the conventional lateral pixel design as shown in Figure 1.

In conventional sputtering methods either the plasma for sputtering can only be struck at higher operating pressures or at moderately low pressures (2-100 mTorr) using a permanent magnet. However, these methods are limited in their capability by operating pressures, limited parameter space in conditioning of the growing films.

The BTD technique on the other hand uses an external broad beam, unfocused, low energy ion source to remotely create plasma that illuminates the sputtering target and the substrate. Because the energy of the ions created is less than the sputter threshold, no sputtering as a result of this ion beam takes place. Because the ion gun geometrically faces the substrate, the ion energy of the gun can be tailored to 'condition' the growing film. The absence of a magnet facilitates the **uniform erosion** (>90%) of the target material. A built in Residual Gas Analyzer (RGA) offers real time monitoring and control of process gases making it

indispensable in reactive sputtering. The BTD tool used deposited highly uniform ( $>\pm 3\%$ ), extremely repeatable ( $\pm 2\%$ ), high resistivity  $VO_x$  thin-films  $\sim 85$  nm thick. The thin films deposited were amorphous (Grazing Incidence XRD Analysis), having an average stoichiometry of  $VO_{2.27}$  as determined by Rutherford Backscattering Spectroscopy (RBS).

Electrical characterization of lateral resistor structures showed resistivities ranging from  $1.2 \times 10^4$  ohm-cm to  $2 \times 10^4$  ohm-cm, TCR varying from  $-3.4\%K^{-1}$  to  $-4.4\%K^{-1}$ , Johnson noise (resistance of  $0.3G\Omega$  for an area of  $2000 \mu m^2$ ) of 4.7 to  $6 \mu V/\sqrt{Hz}$  and 1/f noise characterized by normalized Hooge's parameter ( $\alpha/n$ ) of  $5 \times 10^{-18}$  to  $1 \times 10^{-16} cm^{-3}$ .

In contrast, the through-film resistor structures showed significantly higher resistivities at  $9 \times 10^4$  Ohm-cm to  $1.55 \times 10^5$  Ohm-cm, TCR similar to lateral resistive structure between  $-3.4\%K^{-1}$  to  $-4.5\%K^{-1}$ , immeasurably low Johnson noise (resistance of  $48K\Omega$  for a pixel of  $1600 \mu m^2$ ) and normalized Hooge's parameter ranging from  $1 \times 10^{-18}$  to  $1 \times 10^{-21} cm^{-3}$ . The unexpectedly high resistivity of the through film pixel structures were investigated using Sentaurus simulation package as show in Figures 2a and 2b. The simulation results are indicative of the formation of extremely high resistivity initial-layers that impede current flow resulting in higher through film resistivities.

Figure 3 summarizes the results in comparison with other material systems using a lateral pixel design. Through film conductivity measurements make it possible to achieve higher TCR while maintaining reasonable electrical noise and possibly pose an alternative to the conventional lateral-resistor design currently used in uncooled imaging microbolometers.

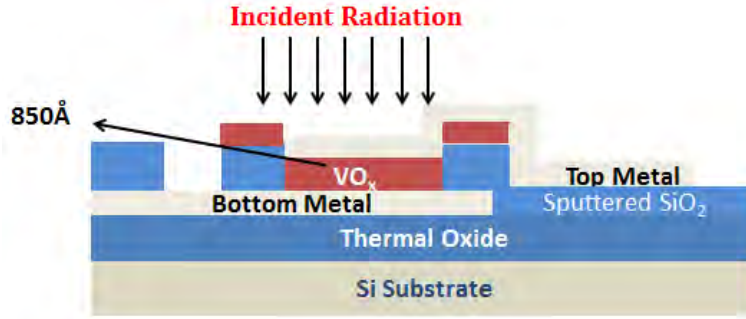


Figure 1. Proposed Through Film Pixel Design

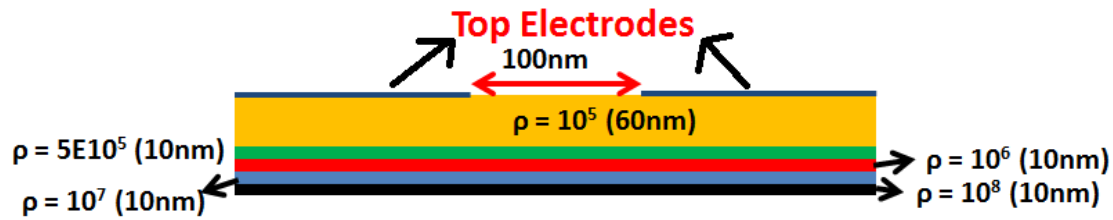


Figure 2a. Sentaurus Simulation structure of a typical lateral resistor pixel configuration. The simulation assumes higher resistivities of initial layers as in common Stranski–Krastanov growth mode

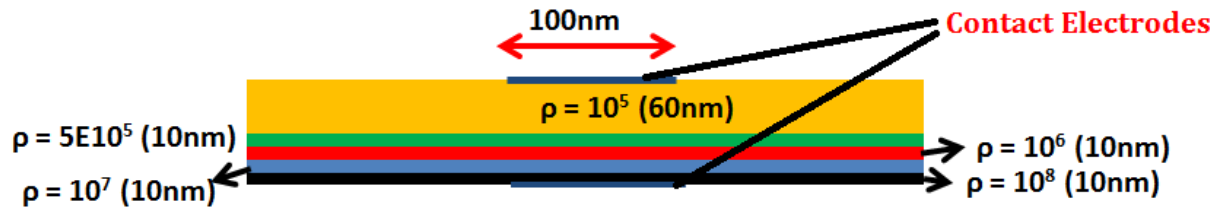


Figure 2a. Sentaurus Simulation structure of the proposed through film pixel configuration. The simulation assumes higher resistivities of initial layers as in common Stranski–Krastanov growth mode

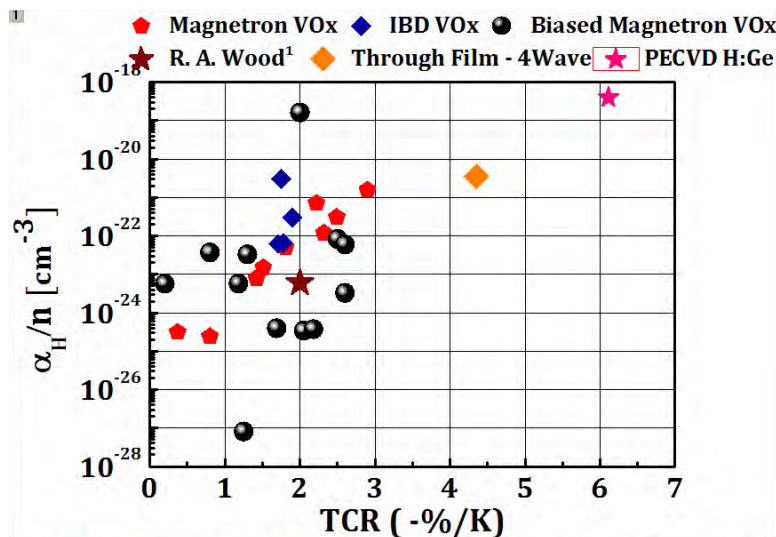


Figure 3: TCR vs.  $\rho$  of  $\text{VO}_x$  thin films deposited by substrate bias deposited vs. other deposition methods

# SUBSTRATE STIFFNESS REGULATES CELLULAR UPTAKE OF NANOPARTICLES

*Changjin Huang,<sup>†</sup> Peter J. Butler,<sup>‡</sup> Sheng Tong,<sup>§</sup> Hari S. Muddana,<sup>‡,±</sup> Gang Bao,<sup>§</sup>  
and Sulin Zhang<sup>†</sup>*

<sup>†</sup>Department of Engineering Science and Mechanics, The Pennsylvania State University,  
University Park, Pennsylvania 16802, USA.

<sup>‡</sup>Department of Bioengineering, The Pennsylvania State University, University Park,  
Pennsylvania 16802, USA.

<sup>§</sup>Department of Biomedical Engineering, Georgia Institute of Technology and Emory University,  
Atlanta, Georgia 30332, USA.

<sup>±</sup>Present address: Skaggs School of Pharmacy and Pharmaceutical Sciences, University of  
California San Diego, La Jolla, CA 92093, USA.

Nanoparticle (NP)-bioconjugates hold great promise for more sensitive disease diagnosis and more effective anticancer drug delivery compared with existing approaches. A critical aspect in both applications is cellular internalization of NPs, which is influenced by NP properties and cell surface mechanics. Despite considerable progress in the optimization of the NP-bioconjugates for improved targeting, to date, there have been no studies aimed at elucidating the role of local physical environments on endocytosis of NPs, despite the widely known effect of extracellular matrix (ECM) mechanics on cellular responses and disease states *in vivo*. Advances in mechanobiology have established that mechanical cues modulate many cell responses, though such modulation is cell-type dependent. In particular, substrate stiffness has been shown to be a regulatory factor for cell spreading<sup>1</sup>, locomotion<sup>2,3</sup>, differentiation<sup>4,5</sup>, and proliferation<sup>6</sup>. It is possible, therefore, that stiffness-regulated cell responses also modulate NP uptake kinetics, and this phenomenon could be utilized as a new avenue to optimize NP designs for more effective *in vivo* delivery.

The studies of the effect of substrate stiffness on cellular uptake of NPs have other significant implications. In relevant physiological conditions, tumor tissues have different stiffnesses as they go through different stages<sup>7</sup>. In addition, a metastatic cancer cell migrates along tissues of

varying stiffness<sup>8</sup>. If the mechanical properties of ECM indeed mediate cellular uptake, such an effect should be taken into account in the optimization of NP-based cancer cell targeting for inhibiting tumor growth and cancer cell metastasis.

Herein, we report, using PA hydrogels of varying stiffness as model substrates and fluorescent polystyrene NPs, that the total cellular uptake of NPs by bovine aortic endothelial cells (BAECs) increases with increasing gel stiffness. To gain insight into the underlying mechanisms, we characterized the relationship between substrate stiffness, spreading area, apical stress fiber formation, and apical membrane tension. By measuring fluorescence lifetime of a lipophilic dye using time-correlated single photon counting (TCSPC), we deduced that increasing substrate stiffness leads to increased membrane tension. The increased tension correlates increased apical actin fiber formation, as confirmed by confocal microscopy imaging. A thermodynamics model complementary to the experimental characterization was then established to rationalize the role of substrate stiffness on the cellular uptake. The model predicts that cell membrane surface area and membrane tension are the governing factors that dictate the cellular uptake of NPs, both of which are modulated by the substrate stiffness. The findings provide new insight into the rational design of NP-

based therapeutic and diagnostic agents for disease detection and treatment.

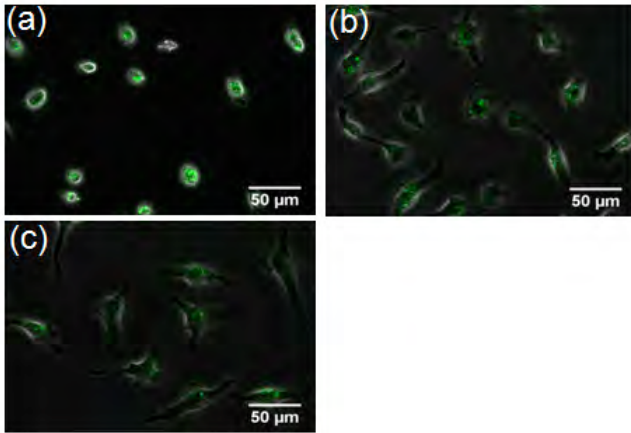


Figure 1. Cellular uptake of the fluorescent NPs by the cells on PA substrates of varying stiffness: (a) soft: 1.6 kPa, (b) intermediate: 3.8 kPa, and (c) stiff: 5.7 kPa. Cells were cultured on substrates for 12 hours before loading the NPs. Images were taken after loading the NPs for 6 hours.

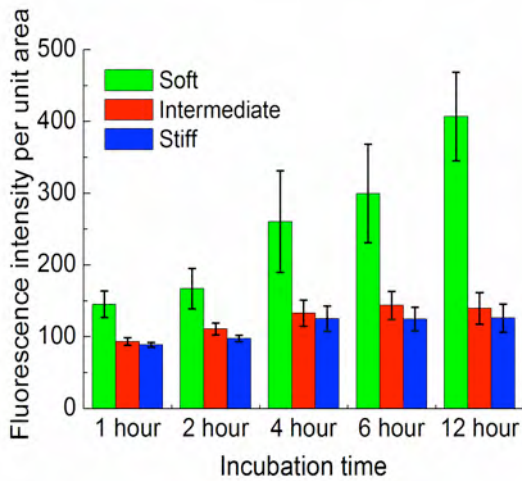


Figure 2. The fluorescence yield of individual cells on gels of varying stiffness normalized by the cell spreading area. The difference between any two groups at each time point is statistically significant ( $p < 0.01$  using student *t*-test).

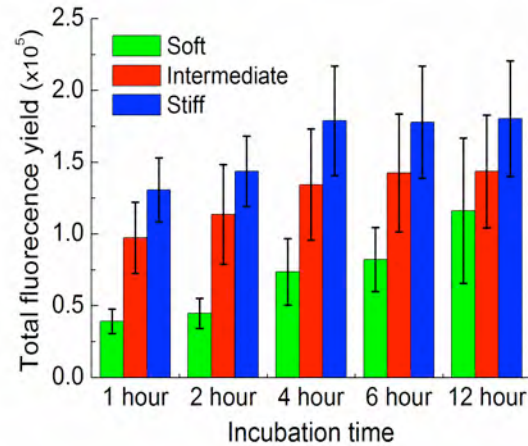


Figure 3. The fluorescence yield of individual cells on PA substrates of varying stiffness. The difference between any two groups at each specified time point is statistically significant ( $p < 0.01$  using student *t*-test).

#### REFERENCES:

- [1] T. Yeung *et al.* "Effects of substrate stiffness on cell morphology, cytoskeletal structure, and adhesion", *Cell Mobil. Cytoskel.* 60, pp 24-34, 2005.
- [2] C. M. Lo, H. B. Wang, M. Dembo, & Y. L. Wang. "Cell movement is guided by the rigidity of the substrate", *Biophys. J.* 79, pp 144-152, 2000.
- [3] M. H. Zaman *et al.* "Migration of tumor cells in 3D matrices is governed by matrix stiffness along with cell-matrix adhesion and proteolysis", *Proc. Natl. Acad. Sci. U. S. A.* 103, pp 10889-10894, 2006.
- [4] D. E. Discher, P. Janmey, & Y.-l. Wang. "Tissue Cells Feel and Respond to the Stiffness of Their Substrate", *Science* 310, pp 1139-1143, 2005.
- [5] A. J. Engler, S. Sen, H. L. Sweeney, & D. E. Discher. "Matrix Elasticity Directs Stem Cell Lineage Specification", *Cell* 126, pp 677-689, 2006.
- [6] R. W. Tilghman *et al.* "Matrix Rigidity Regulates Cancer Cell Growth and Cellular Phenotype", *PLoS One* 5, pp 13, 2010.
- [7] S. Huang & D. E. Ingber. "Cell tension, matrix mechanics, and cancer development", *Cancer Cell* 8, pp 175-176, 2005.
- [8] G. Y. H. Lee & C. T. Lim. "Biomechanics approaches to studying human diseases", *Trends Biotechnol.* 25, pp 111-118, 2007.

**Paper**

**Poster**

## **COARSE-GRAINED MODELING OF HUMAN ERYTHROCYTE MEMBRANE**

*Yao Zhang, Changjin Huang and Sulin Zhang*

Department of Engineering Science and Mechanics, Pennsylvania State University,  
University Park, Pennsylvania 16802, USA

The human erythrocyte (red blood cell, RBC) is the most common blood cell which transports oxygen from lung to human tissues through blood circulation. RBC frequently squeezes through narrow capillaries during its 120-days life span and shows remarkable ability to undergo reversible large deformation. This extraordinary ability stems from the unique structure of its membrane. Compared with phospholipid membranes of other cells, RBC membrane possesses an additional spectrin network tethered to phospholipid layer. This spectrin network provides extra resistance to the shear. In previous studies, RBC membrane

models only including fixed spectrin-network were used to capture the deformability of RBC. However, those models missed the fluidity of membrane and could not simulate the remodeling of cytoskeleton since the spectrin networks were fixed. Experiments show that the remodeling of spectrin network plays an essential role on the RBC shape and its remarkable deformability[1]. On the base of a one-particle thick membrane model[2], we propose a coarse-grained model of RBC membrane including both spectrin network and phospholipid layer to study mechanical properties of RBC membrane.

Paper

Poster

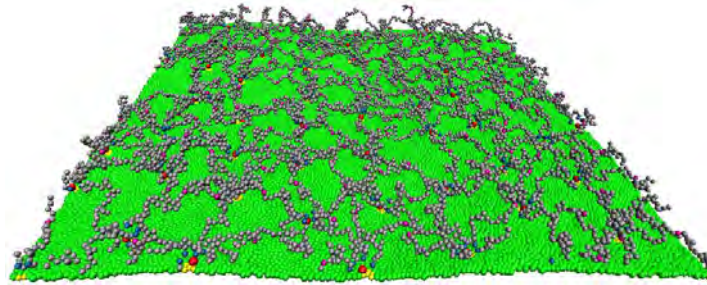


Figure 1. schematic of RBC membrane model

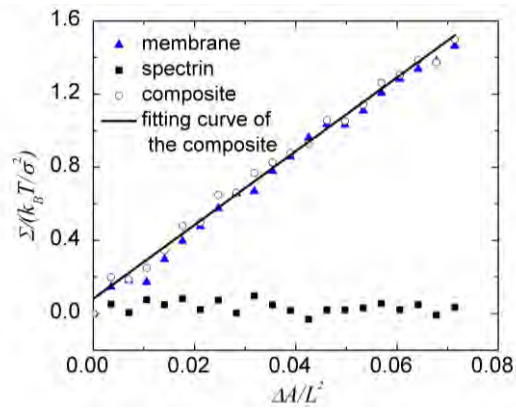


Figure 2. Area compression modulus of RBC membrane model

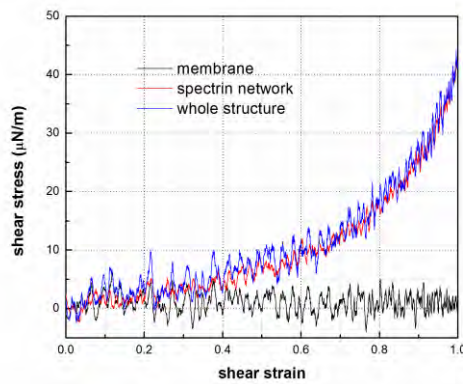


Figure 3. shear stress-strain response of RBC membrane model

## REFERENCE:

1. Li, J., et al., Cytoskeletal dynamics of human erythrocyte, in PNAS. 2007. p. 4937-4942.
2. Yuan, H., et al., One-particle-thick, solvent-free, coarse-grained model for biological and biomimetic fluid membranes. Physical Review E. **82**(1): p. 011905.

**Paper**  
**Poster**

## **IN SITU TEM STUDY LITHIATION-DELITHIATION OF GALLIUM NANODROPLETS**

*Wentao Liang, Sulin Zhang*

Department of Engineering Science and Mechanics, Pennsylvania State University,  
University Park, Pennsylvania 16802, United States

Anode materials, such as Si and Ge, have recently attracted enormous attentions for their much higher theoretical capacity than the conventional Li-graphite anodes. However, the potentiality of these anode materials is significantly comprised due to the lithium insertion/extraction induced huge volume change and subsequent fracture. Here we report in situ transmission electron microscopy (TEM) studies of the electro-chemical cycling behavior of gallium

nanodroplets. We observed void nucleation, growth and diminishment during the lithiation/delithiation cycles, demonstrating the self-repairability of the Gallium Nanodroplets (GaNDs). We attribute the void growth and diminishment to the repeated liquid-to-solid phase transitions during lithiation/delithiation cycles. The self-healing capability of liquid gallium suggests the promise of hybrid anodes consisting of high-capacity materials such as Si and liquid gallium.

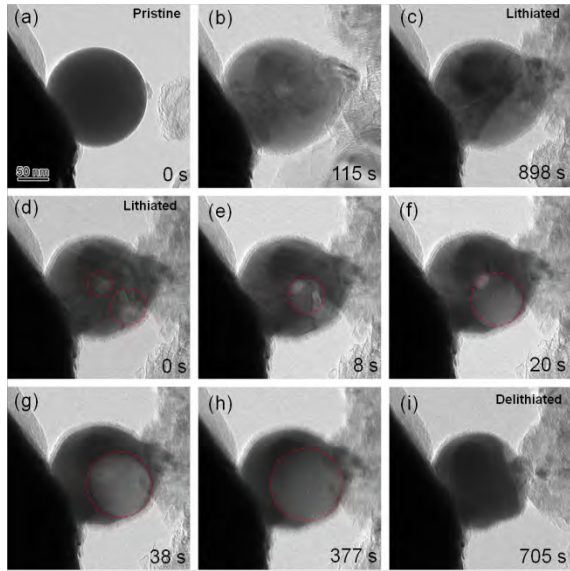


Fig. 1. Morphology evolution of the Gallium nanodrop during the first cycle.

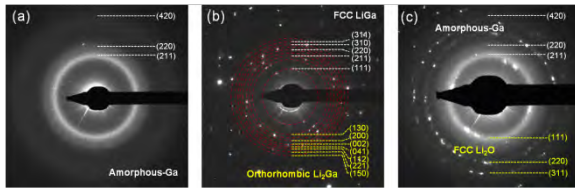


Fig. 2. The typical EDPs (Electron Diffraction Patterns) showing the phase transformations from amorphous Ga phase to crystalline  $Li_xGa$  phase and back to amorphous Ga phase during cycling process.

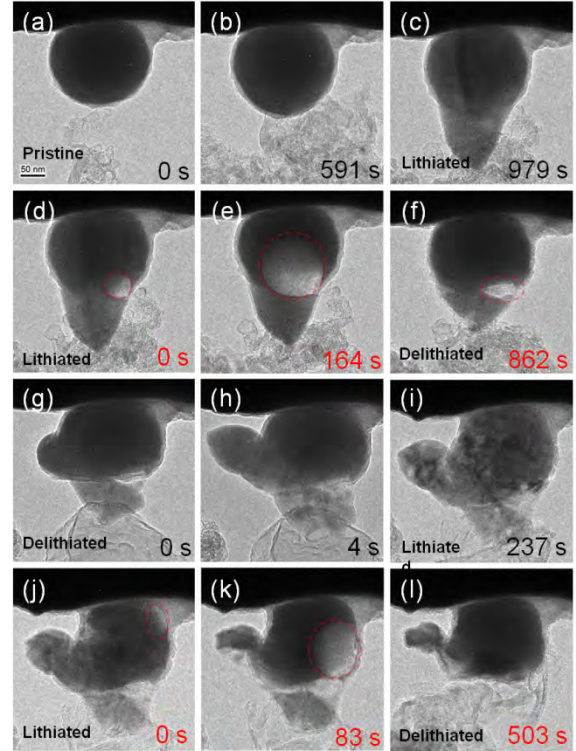


Fig. 3. Morphology evolution during multiple cycling process of Gallium nanodrop.

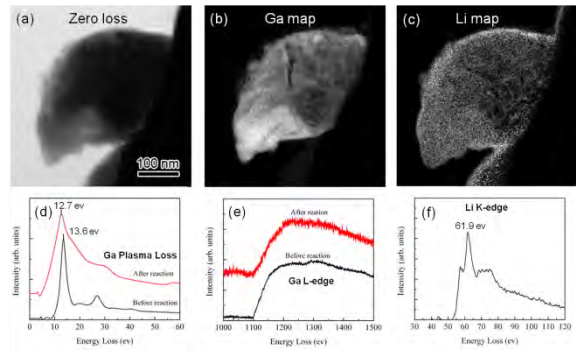


Fig. 4. EELS spectra and maps of Ga, and Li elements of Ga nanodrop after lithiation.

# Alkali Free Boroaluminosilicate Glasses for High Energy Density High Temperature Power Electronic Capacitors

*P. Dash<sup>1,2</sup>, E. Furman<sup>2</sup>, C. G. Pantano<sup>2,3</sup>, M. T. Lanagan<sup>1,2</sup>*

<sup>1</sup>Department of Engineering Science and Mechanics, Penn State, PA, 16802

<sup>2</sup>Materials Research Institute, Penn State, PA, 16802

<sup>3</sup>Department of Material Science and Engineering, Penn State, PA, 16802

One of the biggest engineering innovations in the 20<sup>th</sup> century was the development of capacitor, a solid-state power conversion device, which led to dramatic changes in the way electric power is stored and distributed. New technology in power electronic products like hybrid electric vehicles, implantable medical devices and high power microwave systems require ultra-capacitors with decreased volume, weight, cost and energy densities greater than 30 J/cm<sup>3</sup>. Recently, thin low alkali borosilicate glasses have shown promising trends to be used as high energy density material with energy density as high as 35 J/cm<sup>3</sup> owing to their high dielectric breakdown strength (12 MV/cm). These glasses maintain low dielectric loss up to temperatures of 200°C which is critical for automotive applications with extreme environmental conditions. In addition, thin glass sheets are sufficiently flexible to be wound into a compact capacitor structure. The possibility of fabricating multilayer storage capacitors with this thin glass has created considerable interest in recent years for potential application to DC-bus capacitors in electric vehicles. So far polypropylene is the most commonly used dielectric in hybrid vehicles but they have low relative permittivity (2.1), energy densities approaching 10 J/cm<sup>3</sup>, they occupy significant volume in the capacitors and have limited high temperature capabilities. If these polymer based capacitors are replaced by glass capacitors it would result in five times decrease in capacitor volume which would certainly have a significant impact on the growth of hybrid vehicles which have increased by more than ten fold over the last few years.

Therefore, this study focuses on understanding the complex phenomenon of dielectric breakdown by studying intrinsic material properties (electrical conductivity and dielectric constant), extrinsic microstructural features (surface roughness and inclusions) and experimental conditions. This would help in further enhancing the energy density of these glass capacitors.

Breakdown studies have shown increase in breakdown strength with decreasing glass thickness. The characteristic electrical breakdown field strength increased from 400 MV/m to 1100

MV/m as the glass substrate thickness decreased from 58  $\mu\text{m}$  to 5  $\mu\text{m}$ , respectively. To further investigate structural changes resulting in dielectric breakdown, the glass was poled under several voltage and temperature conditions. Thermoelectric treatment of these glasses under high voltage (500V-2000V) and temperature (250°C-550°C) leads to depletion layer formation beneath the anode due to migration of monovalent and divalent cations.

Activation energies for ionic conduction of alkaline earth and alkali ions in these glasses have been estimated using thermally stimulated depolarization current (TSDC) and AC impedance spectroscopy techniques. TSDC measurements confirm the transport of Na<sup>+</sup> and Ba<sup>2+</sup> cations from below the anode with activation energy of 0.8 eV and 1.7 eV for Na and Ba motion respectively. This ionic transport contributes to ionic conduction in glasses. Low frequency impedance spectroscopy results have also confirmed inhomogeneity in a poled glass due to formation of cation depleted space charge layer.

Migration of positive cations from the depletion layer increases the resistance of that layer resulting in all the voltage dropping across the thin depleted layer. This enables the glass to support fields closer to its intrinsic breakdown strength. Second order non-linear optical measurements demonstrate that the thickness of this depletion layer depends on mobile ion concentration in the glass, poling temperature, applied electric field and is limited by the intrinsic breakdown strength of the glass. Beyond this field, electronic conduction in the depleted layer results in eventual breakdown of the sample. The electronic conduction observed was mainly due to Pool Frenkel emission of electrons in the space charge region.

Using high field TSDC and low frequency AC impedance spectroscopy we have demonstrated a technique to determine the activation energy for alkali and alkaline earth ion transport in glasses. We have also reported mixed alkaline earth effect on electrical conduction in glasses, which to the best of our knowledge has not been reported elsewhere. Due to the high dielectric breakdown strength of these glasses we were also able to study

electronic conduction under high electric fields and understand mechanisms contributing to dielectric breakdown in glasses.

Summarizing these results it is suggested that the combination of high intrinsic breakdown strength, high intrinsic Weibull modulus, high-temperature performance stability, low dielectric loss and graceful failure observed in thin glass samples all point to their potential use as high energy storage devices.

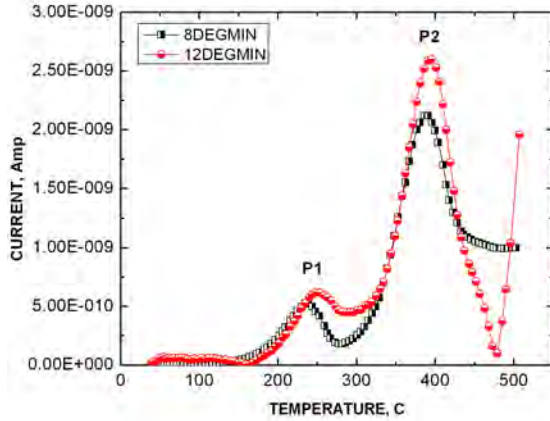


Figure 1: TSDC plot for 50  $\mu\text{m}$  thick AF45 glass poled under a DC bias of 2 kV for two hours at 550°C. P1 and P2 shows the peak associated with the relaxation of Na and Ba cations respectively.

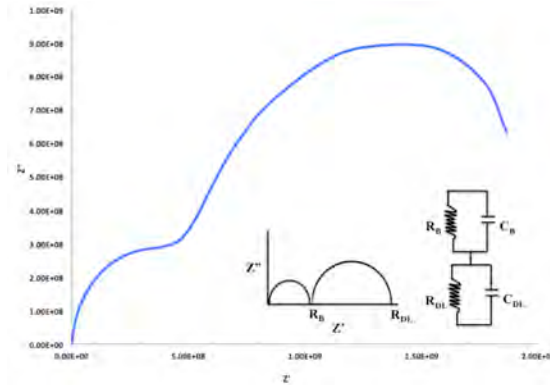


Figure 2: Complex resistivity plot of poled AF45 at 823  $^{\circ}\text{K}$  in a frequency range of 0.01 to 1000 Hz. The insets show an ideal Cole-Cole plot for a two RC circuit model.  $R_b$ ,  $R_{DL}$ ,  $C_b$ ,  $C_{DL}$  are the resistance and capacitance of the bulk and depletion layer respectively in the thermoelectrically poled glass.

Table 1 Variation of depletion layer thickness with applied electric fields.

Poling Field (kV)	Depletion Layer thickness ( $\mu\text{m}$ )	Internal Field ( $10^9 \text{ V/m}$ )
22	6.8	3.23
20	6.4	3.12
15	4	3.75
10	7	1.42

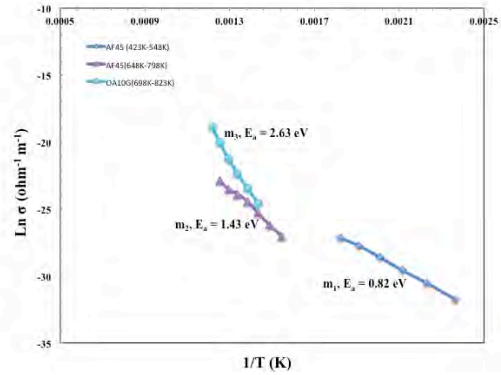


Figure 3: Variation of  $\ln$  conductivity with temperature for AF45 and OA10G at 0.05 Hz obtained from the complex capacitance data.



Figure 4: Second harmonic microscopy image showing depletion layer thickness in 50  $\mu\text{m}$  Ba-Boroaluminosilicate glass poled at 22 KV and 25°C.

### Reference

- [1] N. J. Smith, B. Rangarajan, M. T. Lanagan, C. G. Pantano, Materials Letters 63 (2009) 1245-1248.
- [2] D. E. Carlson, K. W. Hang, G. F. Stockdale, J. Amer. Ceram. Soc. 57 (1974) 295-300.
- [3] Akira Doi, J. of Mater. Sc. 22 (1987) 761-769.
- [4] G. De Mey and W. De Wilde, Elsevier sequoia S.A, (1974) 301-304.
- [5] A.E.Owen, Phys. and Chem. of Glasses 7 (1976) 174-192.
- [6] P.A. Timson, P. Wickens, Elsevier Sequoia S.A. (1970) R55-R58.
- [7] A. Servini, A. K. Jonscher, Thin Solid Films, 3 (1969) 341-365.
- [8] R. M. Catchings, J. Appl. Phys. 50 (1979) 2813-2816.

## **Composite Ni-Encapsulated Particles for Cold-Spray: Hexagonal Boron Nitride, Aluminum, Nickel**

Maryam Neshastehriz, Ivi Smid, Al Segall, Tim Eden

Self-lubricating coatings can improve the performance of contacting surfaces and extend component lifetimes by reducing the coefficient of friction and/or specific wear. In this study, self-lubricating coatings of several metal- and hexagonal-boron-nitride particles in a nickel matrix were investigated. The self-lubricating coatings were created via cold spray. Relatively thick nickel encapsulation was required to aid in coating bonding and formation, and was achieved via electroless Ni plating. The encapsulation process was found to be scalable and amenable to relatively small particles. Once deposited on (e.g.) aluminum or titanium substrates, the coatings were analyzed for bond-strength, micro-hardness, coefficient of friction, and reciprocating wear behavior. The cold spray process can be used for the deposition of such composite particles to produce coatings which possess very attractive physical and mechanical properties, such as reciprocating wear resistance, reduced friction, and high adhesive strengths relative to pure Ni coatings.

# A COMPARISON OF FLUID-STRUCTURE INTERACTION COUPLING ALGORITHMS USING THE FINITE ELEMENT METHOD

*J. Sheldon*

Engineering Science and Mechanics Department, Penn State, PA-16802, USA

The modern design process depends heavily on computational models which simulate experiments that would be difficult or expensive to perform physically. These models utilize governing equations which mathematically reproduce the desired physics. Structural experiments are often modeled using computational solid mechanics packages, while flow problems are simulated with computational fluid dynamics packages; however, there are many multi-physics problems which cannot be properly modeled without including the coupled fluid-structure interaction (FSI). Such models have been used in the medical field for blood flow through blood vessels [1] or heart valves [2], in the Naval field for underwater explosions [3] and implosions [4], and in the aerospace field for parachute clusters [5], to give only a few examples.

The main challenge in FSI is coupling the effects from solid deformation with those of the fluid flow on the fluid-structure interface. There are two canonical coupling methods for FSI, partitioned and monolithic. The partitioned method involves solving the governing equations in a segregated manner until an equilibrium solution is reached, while in the monolithic method they are solved simultaneously in a combined system of equations. The partitioned approach ranges from weakly-coupled to strongly-coupled, where the strength of coupling, from a physical sense, refers to how much deformation the fluid causes on the solid, with more deformation requiring stronger coupling and therefore more coupling iterations.

We present a third coupling strategy, which we call the “partly-monolithic” method, that combines aspects of both the partitioned and monolithic methods. In this approach, diagrammed in Figure 1, the physical domains (the solid and fluid domains) are solved monolithically, while the non-physical computational mesh is solved iteratively.

Typically, partitioned schemes for FSI are viewed as easier to implement than monolithic schemes and as requiring less computational resources. Conversely, monolithic schemes are viewed as challenging to implement and necessitating longer run-times [6]. The trade off comes in that monolithic coupling is always strongly-coupled, and therefore will generally produce more accurate results than a weakly-coupled partitioned method [7].

We developed a finite-element FSI model using the open source finite element library deal.ii. We model our fluids as incompressible, linearly viscous fluids with the Navier-Stokes equations in the arbitrary Lagrangian-Eulerian reference frame. Our solids are modeled as St. Venant-Kirchhoff materials with a two-field formulation of the elasticity equations in the Lagrangian reference frame. Our mesh is modeled by an elastostatics equation for a neo-Hookean material with arbitrarily defined material properties. The standard Galerkin finite-element formulation is used for the solid, fluid, and mesh, with Taylor-Hood elements used for the fluid. The Crank-Nicolson method is implemented for the time discretization.

Using the method of manufactured solutions, we verify that the individual fluid and solid components produce solutions which accurately solve their governing equations. We perform a numerical validation study against results provided by Turek and Hron [8].

Turek and Hron [8] also provide an FSI benchmark case with results. The domain for this benchmark is shown in Figure 2 and a visualization of results is shown in Figure 3. We present a comparison between Turek and Hron's results to this benchmark case and those from our FSI software, for each different coupling algorithm we implemented: partitioned coupling, monolithic coupling, and partly-monolithic coupling. We examine how the different algorithms perform based on their accuracy to Turek and Hron's results and the speed at which they generate a solution.

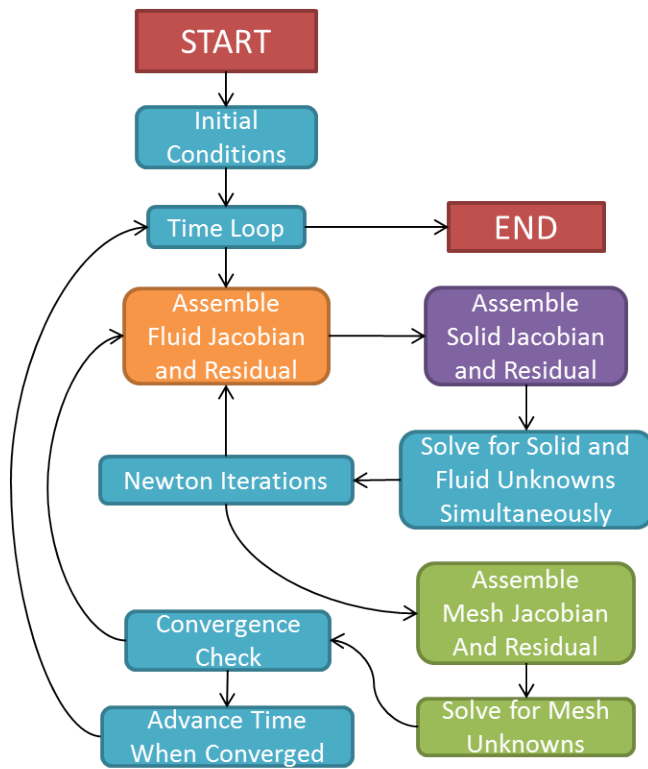


Figure 1. Flowchart demonstrating the partly-monolithic FSI algorithm.

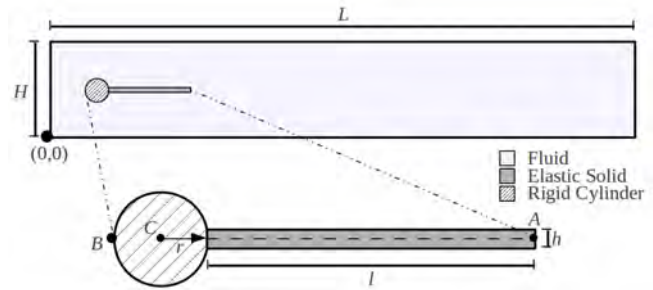


Figure 2. Turek and Hron [8] FSI benchmark domain: a two-dimensional FSI problem where a fluid is flowing through a channel from left to right. Slightly offset from the middle of the channel is a rigid cylindrical obstruction with an elastic flag attached to it.

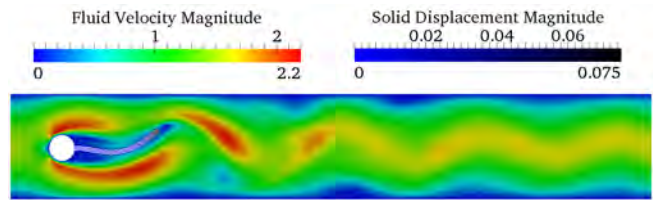


Figure 3. Visualization of FSI benchmark: flow field and solid deformation at  $t = 14.5[s]$ . Solid displacement and fluid velocity are shown with their own color scales.

## REFERENCES:

- [1] Bazilevs, Y., V. Calo, Y. Zhang, and T. Hughes (2006) "Isogeometric fluid–structure interaction analysis with applications to arterial blood flow," *Computational Mechanics*, 38(4), pp. 310–322.
- [2] De Hart, J., G. Peters, P. Schreurs, and F. Baaijens (2000) "A two-dimensional fluid-structure interaction model of the aortic valve," *Journal of Biomechanics*, 33(9), pp. 1079–1088.
- [3] McCoy, R. and C. Sun (1997) "Fluid-structure interaction analysis of a thick-section composite cylinder subjected to underwater blast loading," *Composite structures*, 37(1), pp. 45–55.
- [4] Wang, K., A. Rallu, J. Gerbeau, and C. Farhat (2011) "Algorithms for interface treatment and load computation in embedded boundary methods for fluid and fluid–structure interaction problems," *International Journal for Numerical Methods in Fluids*, 67(9), pp. 1175–1206.
- [5] Takizawa, K., S. Wright, C. Moorman, and T. Tezduyar (2011) "Fluid–structure interaction modeling of parachute clusters," *International Journal for Numerical Methods in Fluids*, 65(1-3), pp. 286–307.
- [6] Campbell, R. and E. Paterson (2011) *Fluid–structure interaction analysis of flexible turbomachinery*, Ph.D. thesis, The Pennsylvania State University.
- [7] Michler, C. (2004) "A monolithic approach to fluid-structure interaction," *Computers & Fluids*, 33, p. 839848.
- [8] Turek, S. and J. Hron (2006) "Proposal for numerical benchmarking of fluid-structure interaction between an elastic object and laminar incompressible flow," *Fluid-Structure Interaction*, pp. 371–385.

**Paper  
Poster**

**ESM TODAY**

**IN SITU LITHIATION MECHANICS OF SILICON NANO-ELECTRODES**

*Hui Yang and Sulin Zhang*

Department of Engineering Science and Mechanics  
The Pennsylvania State University  
University Park, PA 16802

**ABSTRACT**

We present an atomistically informed continuum chemo-mechanical model to study the phase evolution, morphological changes, stress generation, large plastic flow, and failure in lithiated silicon nanowires. Our model couples the reaction-diffusion of lithium with the lithiation-induced elasto-plastic deformation. The simulation results show that the lithiation-induced volume expansion in silicon nanowires is highly anisotropic, with predominant expansion along the  $\langle 110 \rangle$  direction, but negligibly small expansion along the  $\langle 111 \rangle$  direction, which agree striking well with existing independent experimental observations. Such kind of apparent anisotropic swelling is critically controlled by the orientation-

dependent lithiation reaction rate at the atomically sharp phase boundary between the crystalline core and amorphous shell, namely the mobility of an atomically sharp amorphous-crystal interface (ACI). Our modeling results also underscore the importance of structural relaxation by plastic flow behind the moving phase boundary. The atomistically informed modeling framework not only sheds light on the lithiation-mediated failure in nanowire-based electrodes, but also provides a basis for simulating the morphological evolution, stress generation, and failure in high-capacity electrodes for the next-generation lithium-ion batteries.

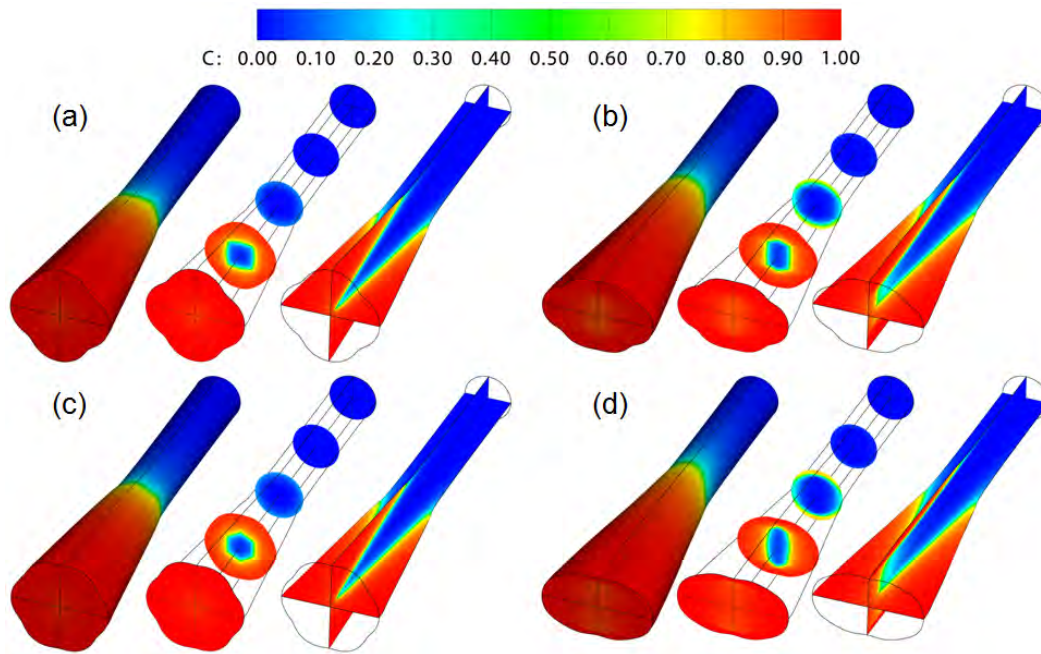


Figure 1: Chemomechanical modeling of the phase transitions and morphological evolutions in (a):  $\langle 100 \rangle$ , (b):  $\langle 110 \rangle$ , (c):  $\langle 111 \rangle$ , and (d):  $\langle 112 \rangle$  silicon nanowires upon lithiation. Colors in the image represent the normalized lithium concentration: red denotes the fully lithiated amorphous silicon ( $\text{Li}_{3.75}\text{Si}$ ), and blue the crystalline silicon. Lithium distributions on different cross-sections of the nanowires are also shown in the second and third columns of each case.

## References

- [1] S. W. Lee, M. T. McDowell, J. W. Choi, Y. Cui, "Anomalous Shape Changes of Silicon Nanopillars by Electrochemical Lithiation", *Nano Lett.*, vol. 11, pp. 3034-3039, 2011.
- [2] X. H. Liu, H. Zheng, L. Zhong, S. Huang, K. Karki, L. Q. Zhang, Y. Liu, A. Kushima, W. T. Liang, J. W. Wang, J.-H. Cho, E. Epstein, S. A. Dayeh, S. T. Picraux, T. Zhu, J. Li, J. P. Sullivan, J. Cumings, C. Wang, S. X. Mao, Z. Z. Ye, S. Zhang, J. Y. Huang, "Anisotropic Swelling and Fracture of Silicon Nanowires during Lithiation", *Nano Lett.*, vol. 11, pp. 3312-3318, 2011.
- [3] X. H. Liu, J. W. Wang, S. Huang, F. Fan, X. Huang, Y. Liu, S. Krylyuk, J. Yoo, S. A. Dayeh, A. V. Davydov, S. X. Mao, S. T. Picraux, S. Zhang, J. Li, T. Zhu, J. Y. Huang, "In situ atomic-scale imaging of electrochemical lithiation in silicon", *Nat. Nanotechnol.*, vol. 7, pp. 749-756, 2012.
- [4] H. Yang, S. Huang, X. Huang, F. Fan, W. Liang, X. H. Liu, L.-Q. Chen, J. Y. Huang, J. Li, T. Zhu, S. Zhang, "Orientation-Dependent Interfacial Mobility Governs the Anisotropic Swelling in Lithiated Silicon Nanowires", *Nano Lett.*, vol. 12, pp. 1953-1958, 2012.

## PROBING FAST BIOMOLECULAR PROCESS USING TIME-CONTROLLED CHEMICAL WAVEFORMS IN MICROFLUIDIC CHANNELS

Daniel Ahmed<sup>a</sup>, Hari S. Muddana<sup>c</sup>, Mengqian Lu<sup>a</sup>, Jarrod French<sup>b</sup>, Brian Kiraly<sup>a</sup>, Xiaole Mao<sup>a</sup>,  
Xiaoyun Ding<sup>a</sup>, Peter J. Butler<sup>c</sup>, Andreas Manz<sup>d</sup>, Stephen J. Benkovic<sup>b,1</sup> and Tony Jun  
Huang<sup>a,d,1,2</sup>

<sup>a</sup>Department of Engineering Science and Mechanics, <sup>b</sup>Department of Chemistry, <sup>c</sup>Department of Bioengineering, The Pennsylvania State University, University Park, PA 16802 USA

Generating chemical waveforms and switches in microfluidic devices with the flexibility to control the various signal attributes has important implications for high-throughput characterization of dynamic chemical<sup>1</sup> and biological processes<sup>2</sup>. For example, dynamic switching or concurrent application of different chemical stimuli is desired for studying dynamic systems such as cell signaling pathways<sup>1</sup> or cascades of chemical reactions.<sup>2</sup> Although considerable progress has been achieved in spatial regulation of chemical stimuli, *i.e.*, generation of chemical gradients<sup>1</sup>, the temporal regulation has received little attention. To date little progress has been made in achieving chemical waveforms or switching of multiple stimuli with milliseconds temporal resolution, which is important to study some of the fastest processes in cells.

In this work we demonstrated ultrafast, programmable chemical waveform and switching generation using acoustically activated bubbles. The schematic diagram of our chemical waveform concept is shown in Fig. 1a. The two inlets were infused with dye and buffer solutions respectively. An air bubble was trapped at the fluid-fluid interface within the horse-shoe structure. An air bubble trapped in a liquid medium acts as a focusing agent of acoustic energy in the presence of an acoustic field. Upon activation of the bubble, the microstreaming rapidly transported and interchanged the liquids in the double-ring recirculation regions. Consequently, when the bubble stops oscillating, the mixing developed by microstreaming stops and the concentrations revert to their original states. Direct translation of electrical signals into chemical waveforms enables programming all the typical features of a function generator (Fig. 2).

Fig. 3a shows the schematic diagram of the device used to demonstrate switching between two different chemical signals, *i.e.* a binary logic circuit. Two horseshoe traps with different dimensions with resonant frequencies of 29.5 kHz and 14.7 kHz respectively were positioned at the two liquid-liquid interfaces (Fig. 3a). The widths of these horse-shoe structures were selected based on their independent actuation. Minimal cross-excitation of these bubbles at the above frequencies was negligible as determined by a microstreaming bead test (Fig. 3b). When bubble A alone is activated at  $f = 14.7$  kHz, the red dye mixed with water filling the region of interest with red dye (Fig. 3c and d, bottom panel). Conversely, when bubble B alone is activated at  $f = 29.5$  kHz, the blue dye mixes with water filling the region of interest with blue dye (Fig. 3d, top panel). Switching between the red and blue dyes was achieved by programming the piezoelectric transducer to alternate between the two excitation frequencies in an oscillatory fashion, such that when bubble A is excited, bubble B remains stationary, and vice versa (Fig. 3e). One could program the transducer to achieve any desired combination of the two signals and each signal may independently access all of the functions of the waveform generator, including frequency and amplitude modulation.

**Word Counts: 440**

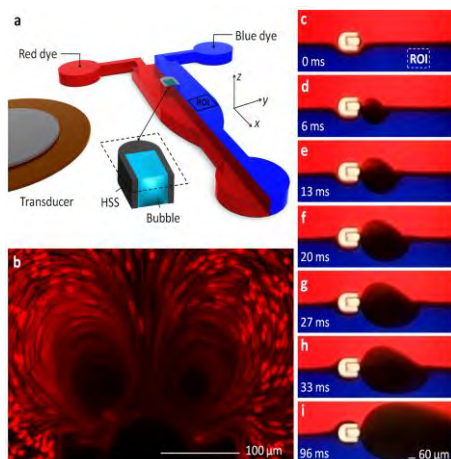


Figure 1: Concept of waveform generation. (a) Schematic of the experimental setup. The piezoelectric transducer, which generates low intensity acoustic waves, is placed adjacent to the microfluidic channel on a cover glass slide. The acoustic waves drive the bubble trapped in the HSS. (b) Microstreaming on particles during bubble oscillation on the x-y plane. (c-i) The mixing of red and blue dyes by microstreaming is captured by high-speed imaging technique.

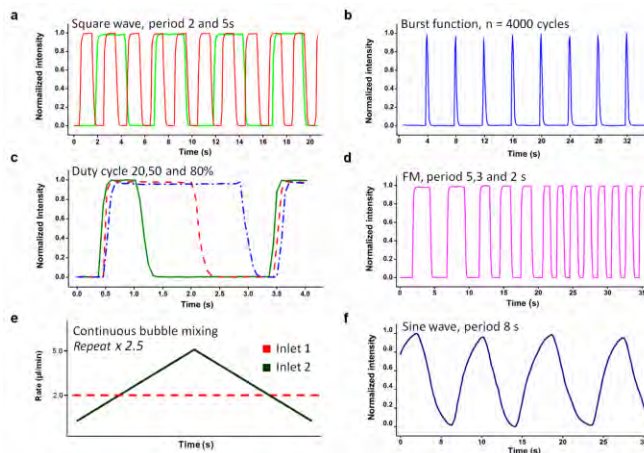


Figure 2: Generation of various chemical waveforms. The region of interest for the output waveform was chosen 500  $\mu\text{m}$  past the recirculation zone, in the bottom half of the channel, Fig 1(c). (a) Square wave. (b) Burst mode (c) Duty cycle. (d) Tunable frequency. (e) Graph of flow rate utilized in achieving amplitude modulation. (f) Sine wave.

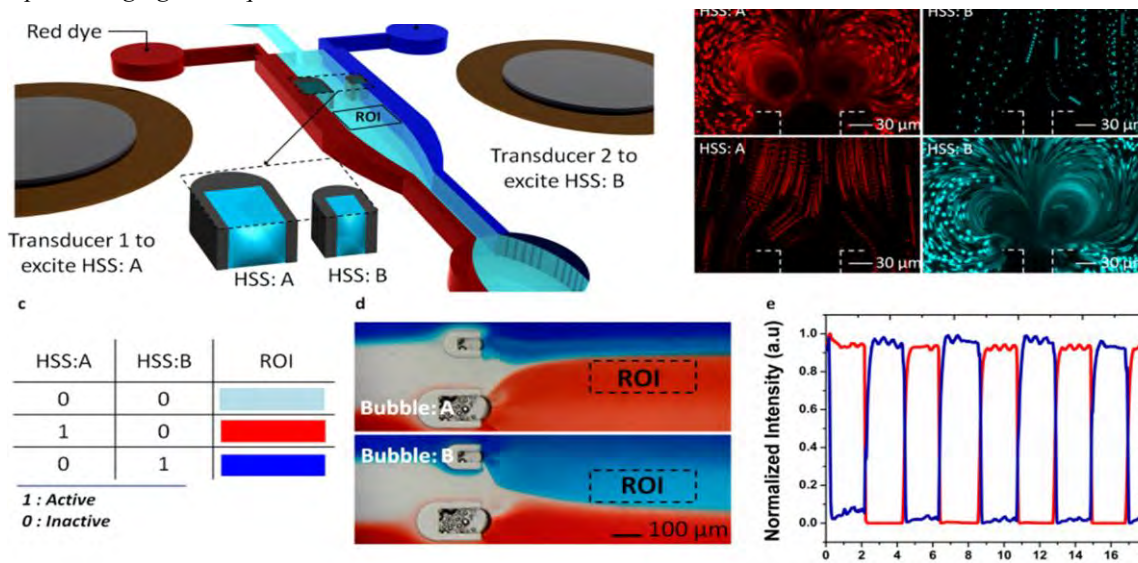


Figure 5: Bubble based switching of blue and red food dyes. (a) Schematic of the experiment setup. The microfluidic fluidic channel contains HSSs of different. (b), Top, microstreaming visualization (red) of bubble trapped in HSS: A, while no streaming is observed in bubble trapped in HSS: B at an excitation frequency of 14.7 kHz. Bottom, microstreaming effect (blue) in bubble trapped in HSS A and no effect on HSS: B at an excitation frequency of 29.5 kHz. (c) Table showing the concept of binary logic circuitry. (d) Result showing the switching mechanism between blue and red dyes. (e) Graph of experimental data for switching between red and blue food dyes in our selected ROI marked in d

## REFERENCES:

- [1] Rocheleau, J. V. *et al.*, Microfluidic glucose stimulation reveals limited coordination on intracellular  $\text{Ca}^{2+}$  activity oscillations in pancreatic islet. *Proc. Natl Acad. Sci. USA* **101**, 12899-12903 (2004).
- [2] T.S Shimizu, Y. Tu, and H. C Berg, "A modular gradient-sensing network for chemotaxis in *Escherichia coli* revealed by responses to time-varying stimuli". *Molecular system Biology*, 2010, **6:382**. doi:10.1038/msb.2010.37

## ACOUSTIC SOFT SWIMMERS AND ITS MOTION AT INTERFACES

*Daniel Ahmed<sup>1</sup>, Mengqian Lu<sup>1</sup>, Hari Mudanna<sup>2</sup>, Nitesh Nama<sup>1</sup>, Vincent Crespi<sup>3</sup>, and Tony Jun Huang<sup>1,2</sup>*

<sup>1</sup>Department of Engineering Science and Mechanics, <sup>2</sup>Department of Bioengineering, <sup>3</sup>Department of Physics. The Pennsylvania State University, University Park, PA 16802 USA

**Introduction:** Microswimmers promises in revolutionizing numerous aspects of medicine, such as, delivering drugs or radioactive sources to remote tumor sites within a body. Furthermore, these devices could potentially act as occlusions to intentionally clog a blood vessel to inhibit recirculation of circulating tumor cells (CTCs), and much more in a non-invasive fashion [1]. To this end, we fabricated hollow cylindrical containers that trap asymmetric bubbles. Excitation by an external acoustic field induces propulsion such as translation, rotation and revolution motion, and these characteristics were analyzed in this study.

**Materials and Methods:** The microswimmers were fabricated by sandwiching a droplet of poly (ethylene glycol) (PEG) containing photosensitive initiator within two glass slides separated by 1-150  $\mu\text{m}$  spacers. Hollow cylindrical structures are formed by exposing oligomer to ultraviolet (UV) light for  $< 0.2$  s through an array of ring-shaped transparency masks attached to the field stop of an inverted microscope. Asymmetrical bubbles were obtained by confining air within the cylindrical containers. The particles were then chemically treated, thus allowing repeatable trapping of asymmetric bubbles within the hollow structures when immersed in liquid.

**Results:** Two different PEG swimmers were designed to produce translational motion. One type contains a single bubble and the other contains two bubbles of equal size. The swimmers are placed in a water reservoir (**Fig 1a** for the experimental setup) and are excited by ultrasonic acoustic waves. The bubbles oscillate, acting like micro transducers, in the acoustic field and generate forces thus propelling the swimmer. **Fig 1d-i, Fig 1j-o** show the propulsion for a single-bubble PEG system and a two-bubble PEG system, respectively. The propulsion mechanism is based on the asymmetric bubble configurations. For a single bubble system, there exists one air-liquid interface at which a force can be developed, as seen in the free body diagram in **Fig 1b**. Thus, an unbalance force is applied to the system causing it to accelerate. In the case of two-bubble system, there exist four air-liquid interfaces and each generating force to the surrounding liquid, as shown in the free body diagram in **Fig. 4c**. Since both bubbles trapped within the hollow cylinders are asymmetric and identical, the two curvatures of air-liquid interface on one side are smaller than those on the other. Thus, an unbalanced resultant force is applied in-line with the center of mass. The direction of each swimmer is only determined by their initial orientation, as the force is applied in-line with the objects center of mass. To obtain revolution, a PEG structure was generated with two asymmetric bubbles of different sizes as shown in **Fig. 1p**. Since the bubbles are different in size each of the four air-liquid interfaces has difference curvature and each generates a different force. Again an unbalanced force is generated; however in this case the force is slightly off centre, generating revolution.

**Conclusion:** A novel concept of propulsion demonstrating different type of propulsion: translation, rotation and revolution. Though early stage, we believe that these swimmers will find themselves useful in non-invasive medical surgical needs such as targeted drug delivery, brachytherapy, ablation, etc.

**References:** 1. Nelson BJ, *et al.* 2010. Microrobots for minimally invasive medicine. *Annu. Rev. Biomed. Eng.* 12: 55-85.

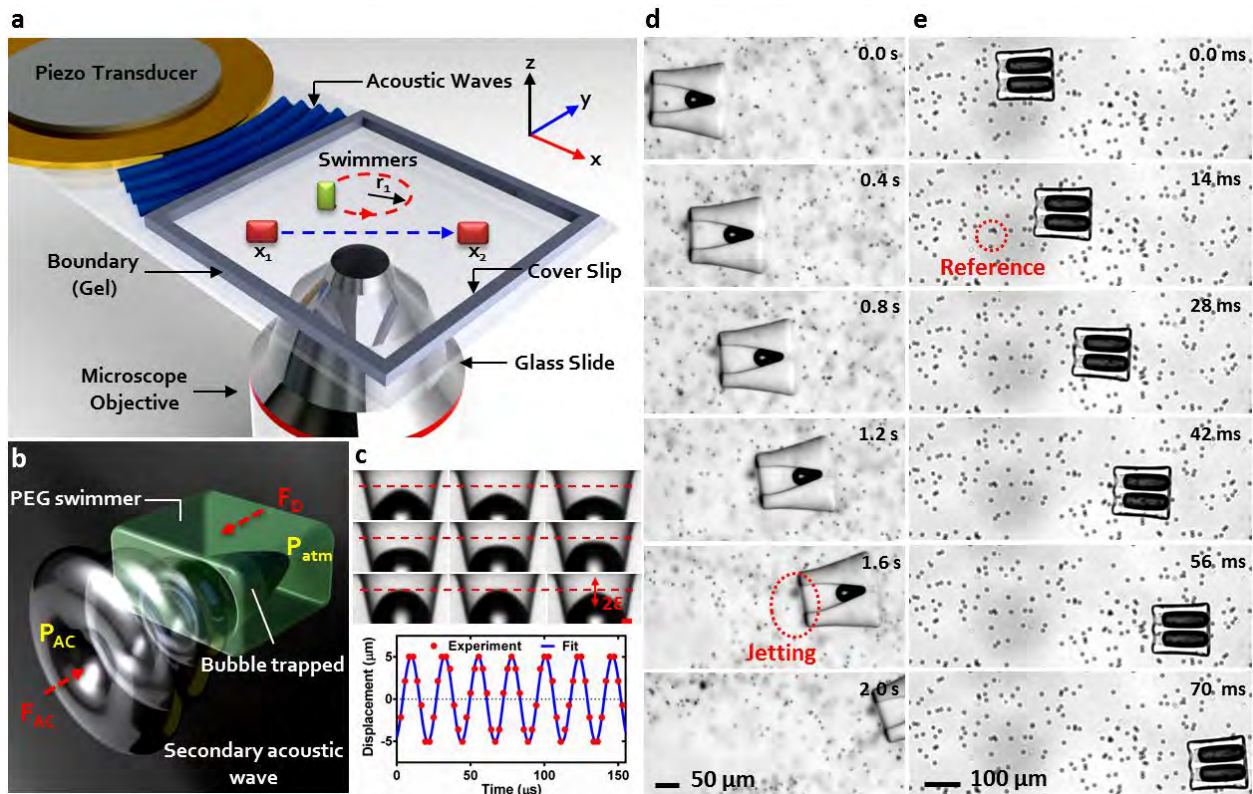


**Fig. 2 Setup, concept and linear motion.** *a.* Schematic of the experimental setup. A piezoelectric transducer, which generates low-intensity acoustic waves is placed adjacent to a cell (water reservoir). Gel or clay was used at the boundary to minimize reflection of acoustic waves. *b.* Free body force diagrams of a bubble PEG composite systems. *c.* Image sequence taken by high-speed recording at 360,000 fps demonstrating the oscillation of bubble, fitted to a sine (solid line). *d.* Image sequence of linear motion (moving left to right) of a PEG swimmer with a bubble trapped at the centre when exposed to an acoustic field (see also Supporting Movie M2). Note the expulsion of particles at 1.6 seconds. *e.* Image sequence of a linear motion (moving left to right) of a PEG swimmer trapping multiple bubbles within the containers (see also Supporting Movie M3). The swimmers propel in the same trajectory as their initial orientation. Note. Attached polystyrene particles on the substrate serves as a reference point for propulsion.

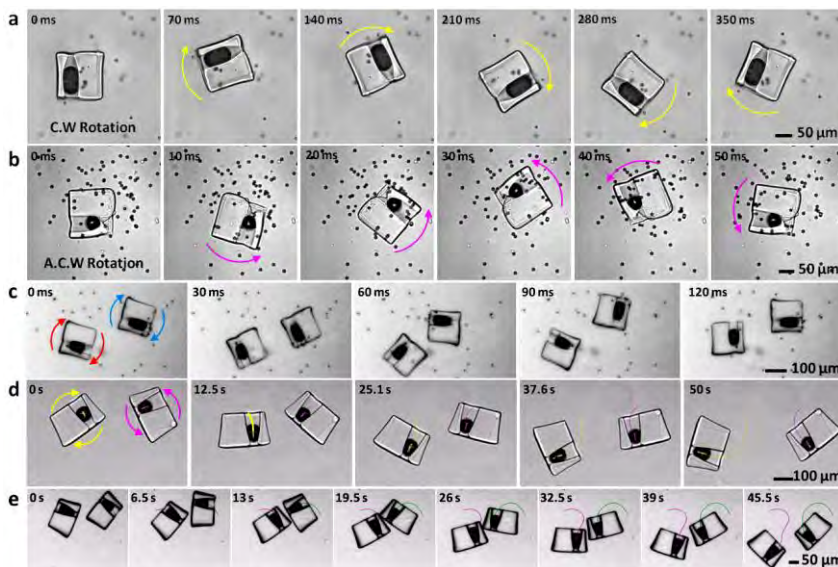


**Fig. 2 Rotational motion.** *a.* Clockwise rotation of a PEG swimmer in water mixed with beads with a bubble trapped off-centered from the center of the mass during bubble oscillation. *b.* Anticlockwise rotation of a PEG swimmer in water when the bubble is trapped opposite to the arrangement, shown in (figure 3a). *c.* Anticlockwise rotation of Multiple swimmer in water. Image sequence of *a, b* and *c* are taken by high-speed recording at 10,000 fps. *d.* Multiple swimmers rotating independently in clockwise and anticlockwise direction in gel. *e.* Swimmers come into contact with each other. *d* and *e* are taken by high-speed recording at 15 fps.

## CHARACTERIZATION OF TITANIUM NITRIDE FORMED VIA LASER-SUSTAINED PLASMA INTERACTION WITHOUT DIRECT IRRADIATION OF THE SUBSTRATE

*A. N. Black, S. M. Copley and J. A. Todd*

Engineering Science and Mechanics Department, Penn State, University Park, PA, 16802, USA

Industries ranging from aerospace to biomedical utilize titanium and its alloys due to their superior strength, high strength-to-weight ratio, low density, high melting point, excellent corrosion resistance, high fracture toughness, good heat transfer properties, gold appearance, and biocompatibility [1, 2]. The poor tribological characteristics of these metals, however, reduce their applicability under severe wear conditions [3]. To enhance these properties, titanium nitride (TiN) coatings are often employed due to their extreme hardness, excellent corrosion and wear resistances, high thermal conductivity, important transport properties, chemical inertness, and gold appearance [4]. Thus, TiN is commonly used for protective coatings on cutting tools and drill bits, diffusion barriers in microelectronics, metal smelting crucibles, optical coatings, and decorative features [5].

Laser nitriding is a process in which laser irradiation melts a titanium surface while under a nitrogen-containing atmosphere. It has been investigated since the 1980s because of its potential as a fast, effective TiN synthesis technique [6]. During laser nitriding, the interaction of the laser melt and species evaporated from the surface produces near-surface plasma. The impact of this laser-induced plasma is a subject of much discussion; some consider it to enhance the coating process [7-9], others say it is detrimental to nitridation [10, 11], while most ignore its potential effects [12-14]. The research to be presented investigates the effect of plasma on a Ti surface without direct laser melting by utilizing laser-sustained plasma (LSP).

LSP, originally referred to as a “continuous optical discharge” is plasma generated by a laser beam in a gaseous atmosphere that can be sustained indefinitely away from any potentially interacting surface [15]. While LSP has been successfully used to deposit diamond [16-18], its potential contributions to the formation of a broad range of hard coating compositions has not been systematically explored. LSP is an optical discharge plasma, similar to a laser-induced plasma. While this optical discharge plasma can be used to melt a surface, it also provides a novel method for studying the influence of plasma on a Ti substrate without the laser beam interacting directly with the surface.

There is an important distinction between the experimental process being presented and conventional laser nitriding. In laser nitriding, the main heat source responsible for melting is the laser beam. In the process under consideration, LSP is the heat source responsible for melting the titanium

substrate. The term LSP nitriding is used to indicate that LSP, and not the laser, is being used as the heat source. The laser is used only to maintain the LSP and does not have any direct interaction with the material being nitrided.

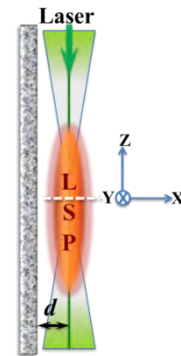


*Figure 1: A side view of the experimental setup showing  $d$ , the distance between the laser centerline (indicated by the green line) and substrate surface. The size and shape of the LSP are shown schematically. The green arrow indicates the direction of the laser beam, while the white, dashed line indicates the location of the laser's focal plane.*

In order to melt the surface without irradiating it, the LSP is translated to a location some distance,  $d$ , from the substrate, as shown in Figure 1. In all cases, it was determined there was no effect from the laser beam on the substrate without the LSP being present. Values for  $d$  tested were between 2 mm and 5 mm. Each distance produced a different melt pattern, as shown in Figure 2. These tests were performed on ASTM grade 2, commercially pure (< 99.5%) titanium plates. Some were processed with the as-received, unpolished, milled surface, while others were polished mechanically prior to LSP exposure. In addition, length of exposure was considered.

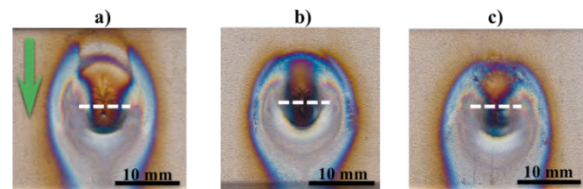


*Figure 2: Macroscale images for the LSP parallel configuration after 5 seconds at: a)  $d = 2$  mm; b)  $d = 2.5$  mm; and c)  $d = 3$  mm.*

During processing, images were collected via a CCD camera with appropriate filters to minimize oversaturation and modified frame-grabbing software, so processing could be visually monitored (see Figure 3). Scanning electron microscopy (SEM) with a backscattered electron (BSE) detector and energy-dispersive x-ray spectroscopy (EDS) were utilized to analyze the initial products of the process, as well as transverse and longitudinal metallographic cross-sections.

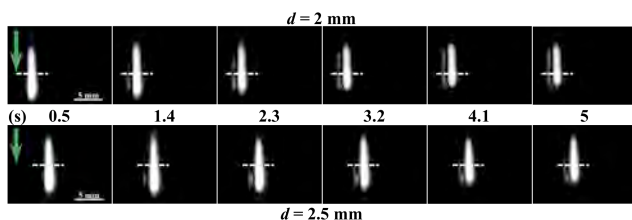


Figure 3: Progression of growth as seen through a 870 nm bandpass filter with 0.6 neutral density filter. The brightest portion of each image shows the LSP with the plate to the left. The green arrows indicate the direction of the laser beam, while the white, dashed lines indicates the location of the laser's focal plane.

Using EDS results in conjunction with the macroscale images seen in Figure 2 and previous literature on nitriding, it was determined that hypo-stoichiometric, near-stoichiometric [19], and hyper-stoichiometric [20] TiN developed at the main impact site. Also present were regions of TiO<sub>2</sub> [21] and locations where a nanoscale layer of TiO<sub>2</sub> covered a deeper layer of TiN [22].

Surface morphologies varied widely between the three values for  $d$  tested.  $d = 3$  mm showed little structure, while the  $d = 2$  mm and  $d = 2.5$  mm samples showed more mature crystallization and evidence of evaporative growth. Cross-sections showed solid and dendritic layers very similar to those seen in laser nitrided TiN. It was also noted that convection assists the permeation of nitrogen into the titanium melt, similar to the convective currents found in laser nitriding.

In addition to SEM and EDS, a focused ion beam was used to take cross-sections of the crystals on the surface for transmission electron microscope (TEM) examination. Diffraction indicates a deformed cubic structure, while electron energy loss spectroscopy (EELS) showed that the crystals have low levels of oxygen which may cause the deformation of the lattice and indicate that the crystals grow while the surface is cooling after the LSP was extinguished.

The regions of high nitrogen concentration, the convective movement within the melt pool, and the surface growth are the most significant structures seen in the LSP nitrided Ti. The faceted crystal growth on the surface and the dendritic layer below it suggest that there are two growth mechanisms

at work during LSP nitriding: one in the melt and another from the vapor.

**Word Count: 868**

- [1] Caron RN and Staley JT. Titanium and Titanium Alloys, in: Dieter GE (Ed.). ASM Handbook, vol. 20. Materials Park, OH: ASM International; 1997.
- [2] Zhang J, Fan D, Sun Y, Zheng Y. Key Eng Mater 2007; 353-358:1745.
- [3] Guo B, Zhou J, Zhang S, Huidi Z, Pu Y, Chen J. Mater Sci Eng A 2008;480:404.
- [4] Tavares J, Coulombe S, Meunier J-L. J Phys D: Appl Phys 2009;42:1020011.
- [5] Wu M. J Alloys Compd 2009; 486:223.
- [6] Spies H-J. Surf Eng 2010; 26:126.
- [7] Akarapu RK, Dua P, Campbell A, Scott D, Nassar A, Todd JA, Copley SM. Proc Mater Res Soc Symp 2007; 1040:Q08.
- [8] Höche D, Rapin G, Kaspar J, Shinn M, Schaaf P. Appl Surf Sci 2007; 253:8041.
- [9] Thomann AL, Sicard E, Boulmer-Leborgne C, Vivien C, Hermann J, Andreatza-Vignolle C, Andreatza P, Meneau C. Surf Coat Technol 1997; 97:448.
- [10] Chen X, Wu G, Wang R, Guo W, Yang J, Cao S, Wang Y, Han W. Surf Coat Technol 2007; 201:4843.
- [11] Kloosterman AB. Surface Modification of Titanium with Lasers. Groningen: Groningen University Press; 1998.
- [12] Jianglong L, Qiquan L, Zhirong Z. Surf Coat Technol 1993; 57:191.
- [13] Raaif M, El-Hossary FM, Negm NZ, Khalil SM, Kolitsch A, Höche D, Kaspar J, Mändl S, Schaaf P. J Phys D: Appl Phys 2008; 41:085208.
- [14] Mridna S, Baker TN. J Mater Process Technol 1998; 77:115.
- [15] Keefer D. Laser-Induced Plasmas and Applications. Radziemski LJ, Cremers DA (Ed.). New York, NY: Marcel Dekker, Inc.; 1989.
- [16] Bolshakov AP, Konov VI, Vostrikov VG, Dubrovskii VY, Kosyrev FK, Naumov VG, Shachkin LV. Quantum Electron 2008; 38:165.
- [17] Schwarz J, Meteva K, Grigat A, Schubnov A, Metev S, Vollertsen F. Diamond Relat Mater 2005; 14:305.
- [18] Varnin VP, Laptev VA, Ralchenko VG. Inorg Mater 2006; 42:S1.
- [19] Weerasinghe VM, West DRF, de Damborenea J. J Mater Process Technol 1996; 58:79.
- [20] Kato A, Tamari N. J Cryst Growth 1975; 29:55.
- [21] Kurtz SR, Gordon RG. Thin Solid Films 1986; 140:277.
- [22] Wu HZ, Chou TC, Mishra A, Anderson DR, Lampert JK, Gujrathi SC. Thin Solid Films 1990; 191:55.

# CHARACTERIZATION OF TITANIUM NITRIDE FORMED VIA LASER-SUSTAINED PLASMA INTERACTION WITHOUT DIRECT IRRADIATION OF THE SUBSTRATE

*A. N. Black, S. M. Copley and J. A. Todd*

Engineering Science and Mechanics Department, Penn State, University Park, PA, 16802, USA

Industries ranging from aerospace to biomedical utilize titanium and its alloys due to their superior strength, high strength-to-weight ratio, low density, high melting point, excellent corrosion resistance, high fracture toughness, good heat transfer properties, gold appearance, and biocompatibility [1, 2]. The poor tribological characteristics of these metals, however, reduce their applicability under severe wear conditions [3]. To enhance these properties, titanium nitride (TiN) coatings are often employed due to their extreme hardness, excellent corrosion and wear resistances, high thermal conductivity, important transport properties, chemical inertness, and gold appearance [4]. Thus, TiN is commonly used for protective coatings on cutting tools and drill bits, diffusion barriers in microelectronics, metal smelting crucibles, optical coatings, and decorative features [5].

Laser nitriding is a process in which laser irradiation melts a titanium surface while under a nitrogen-containing atmosphere. It has been investigated since the 1980s because of its potential as a fast, effective TiN synthesis technique [6]. During laser nitriding, the interaction of the laser melt and species evaporated from the surface produces near-surface plasma. The impact of this laser-induced plasma is a subject of much discussion; some consider it to enhance the coating process [7-9], others say it is detrimental to nitridation [10, 11], while most ignore its potential effects [12-14]. The research to be presented investigates the effect of plasma on a Ti surface without direct laser melting by utilizing laser-sustained plasma (LSP).

LSP, originally referred to as a “continuous optical discharge” is plasma generated by a laser beam in a gaseous atmosphere that can be sustained indefinitely away from any potentially interacting surface [15]. While LSP has been successfully used to deposit diamond [16-18], its potential contributions to the formation of a broad range of hard coating compositions has not been systematically explored. LSP is an optical discharge plasma, similar to a laser-induced plasma. While this optical discharge plasma can be used to melt a surface, it also provides a novel method for studying the influence of plasma on a Ti substrate without the laser beam interacting directly with the surface.

There is an important distinction between the experimental process being presented and conventional laser nitriding. In laser nitriding, the main heat source responsible for melting is the laser beam. In the process under consideration, LSP is the heat source responsible for melting the titanium

substrate. The term LSP nitriding is used to indicate that LSP, and not the laser, is being used as the heat source. The laser is used only to maintain the LSP and does not have any direct interaction with the material being nitrided.

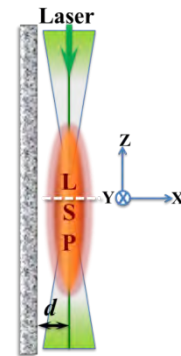


*Figure 1: A side view of the experimental setup showing  $d$ , the distance between the laser centerline (indicated by the green line) and substrate surface. The size and shape of the LSP are shown schematically. The green arrow indicates the direction of the laser beam, while the white, dashed line indicates the location of the laser's focal plane.*

In order to melt the surface without irradiating it, the LSP is translated to a location some distance,  $d$ , from the substrate, as shown in Figure 1. In all cases, it was determined there was no effect from the laser beam on the substrate without the LSP being present. Values for  $d$  tested were between 2 mm and 5 mm. Each distance produced a different melt pattern, as shown in Figure 2. These tests were performed on ASTM grade 2, commercially pure (< 99.5%) titanium plates. Some were processed with the as-received, unpolished, milled surface, while others were polished mechanically prior to LSP exposure. In addition, length of exposure was considered.

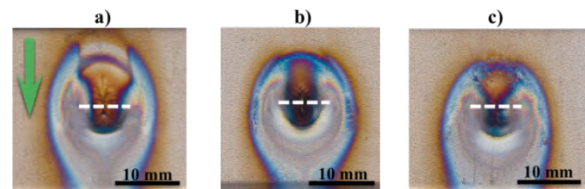


*Figure 2: Macroscale images for the LSP parallel configuration after 5 seconds at: a)  $d = 2$  mm; b)  $d = 2.5$  mm; and c)  $d = 3$  mm.*

During processing, images were collected via a CCD camera with appropriate filters to minimize oversaturation and modified frame-grabbing software, so processing could be visually monitored (see Figure 3). Scanning electron microscopy (SEM) with a backscattered electron (BSE) detector and energy-dispersive x-ray spectroscopy (EDS) were utilized to analyze the initial products of the process, as well as transverse and longitudinal metallographic cross-sections.

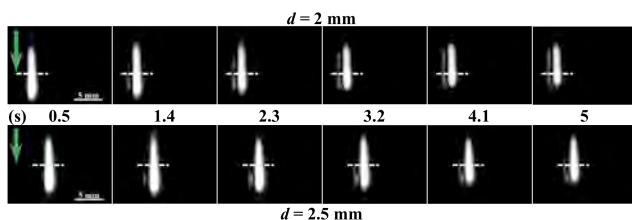


Figure 3: Progression of growth as seen through a 870 nm bandpass filter with 0.6 neutral density filter. The brightest portion of each image shows the LSP with the plate to the left. The green arrows indicate the direction of the laser beam, while the white, dashed lines indicates the location of the laser's focal plane.

Using EDS results in conjunction with the macroscale images seen in Figure 2 and previous literature on nitriding, it was determined that hypo-stoichiometric, near-stoichiometric [19], and hyper-stoichiometric [20] TiN developed at the main impact site. Also present were regions of TiO<sub>2</sub> [21] and locations where a nanoscale layer of TiO<sub>2</sub> covered a deeper layer of TiN [22].

Surface morphologies varied widely between the three values for  $d$  tested.  $d = 3$  mm showed little structure, while the  $d = 2$  mm and  $d = 2.5$  mm samples showed more mature crystallization and evidence of evaporative growth. Cross-sections showed solid and dendritic layers very similar to those seen in laser nitrided TiN. It was also noted that convection assists the permeation of nitrogen into the titanium melt, similar to the convective currents found in laser nitriding.

In addition to SEM and EDS, a focused ion beam was used to take cross-sections of the crystals on the surface for transmission electron microscope (TEM) examination. Diffraction indicates a deformed cubic structure, while electron energy loss spectroscopy (EELS) showed that the crystals have low levels of oxygen which may cause the deformation of the lattice and indicate that the crystals grow while the surface is cooling after the LSP was extinguished.

The regions of high nitrogen concentration, the convective movement within the melt pool, and the surface growth are the most significant structures seen in the LSP nitrided Ti. The faceted crystal growth on the surface and the dendritic layer below it suggest that there are two growth mechanisms

at work during LSP nitriding: one in the melt and another from the vapor.

**Word Count: 868**

- [1] Caron RN and Staley JT. Titanium and Titanium Alloys, in: Dieter GE (Ed.). ASM Handbook, vol. 20. Materials Park, OH: ASM International; 1997.
- [2] Zhang J, Fan D, Sun Y, Zheng Y. Key Eng Mater 2007; 353-358:1745.
- [3] Guo B, Zhou J, Zhang S, Huidi Z, Pu Y, Chen J. Mater Sci Eng A 2008;480:404.
- [4] Tavares J, Coulombe S, Meunier J-L. J Phys D: Appl Phys 2009;42:1020011.
- [5] Wu M. J Alloys Compd 2009; 486:223.
- [6] Spies H-J. Surf Eng 2010; 26:126.
- [7] Akarapu RK, Dua P, Campbell A, Scott D, Nassar A, Todd JA, Copley SM. Proc Mater Res Soc Symp 2007; 1040:Q08.
- [8] Höche D, Rapin G, Kaspar J, Shinn M, Schaaf P. Appl Surf Sci 2007; 253:8041.
- [9] Thomann AL, Sicard E, Boulmer-Leborgne C, Vivien C, Hermann J, Andreatza-Vignolle C, Andreatza P, Meneau C. Surf Coat Technol 1997; 97:448.
- [10] Chen X, Wu G, Wang R, Guo W, Yang J, Cao S, Wang Y, Han W. Surf Coat Technol 2007; 201:4843.
- [11] Kloosterman AB. Surface Modification of Titanium with Lasers. Groningen: Groningen University Press; 1998.
- [12] Jianglong L, Qiquan L, Zhirong Z. Surf Coat Technol 1993; 57:191.
- [13] Raaif M, El-Hossary FM, Negm NZ, Khalil SM, Kolitsch A, Höche D, Kaspar J, Mändl S, Schaaf P. J Phys D: Appl Phys 2008; 41:085208.
- [14] Mridna S, Baker TN. J Mater Process Technol 1998; 77:115.
- [15] Keefer D. Laser-Induced Plasmas and Applications. Radziemski LJ, Cremers DA (Ed.). New York, NY: Marcel Dekker, Inc.; 1989.
- [16] Bolshakov AP, Konov VI, Vostrikov VG, Dubrovskii VY, Kosyrev FK, Naumov VG, Shachkin LV. Quantum Electron 2008; 38:165.
- [17] Schwarz J, Meteva K, Grigat A, Schubnov A, Metev S, Vollertsen F. Diamond Relat Mater 2005; 14:305.
- [18] Varnin VP, Laptev VA, Ralchenko VG. Inorg Mater 2006; 42:S1.
- [19] Weerasinghe VM, West DRF, de Damborenea J. J Mater Process Technol 1996; 58:79.
- [20] Kato A, Tamari N. J Cryst Growth 1975; 29:55.
- [21] Kurtz SR, Gordon RG. Thin Solid Films 1986; 140:277.
- [22] Wu HZ, Chou TC, Mishra A, Anderson DR, Lampert JK, Gujrathi SC. Thin Solid Films 1990; 191:55.

## FROM LAB TO CLINIC: A MICROFLUIDIC BASED FULLY INTEGRATED ON-CHIP FLOW CYTOMETER.

*Ahmad Ahsan NAWAZ, Xiaole Mao, Sz-Chin Steven Lin, Michael Lapsley, Yanhui Zhao and Tony Jun Huang.*

Engineering Science and Mechanics Department, Penn State, PA-16802, USA

Flow cytometry is widely used to rapidly and quantitatively analyze biological samples such as blood cells, tumor cells, bio-particles or even DNA molecules.<sup>1-7</sup> To perform this analysis, the particles in the sample are passed in a single-file line through an optical detection region, where a focused laser beam interrogates each particle. The resulting scattered light and fluorescence emissions are collected by detectors and analyzed in order to provide valuable information about the sample, such as the size, complexity, and health of cells. Due to its ability to rapidly analyze heterogeneous samples at rates of up to several thousand cells per second, flow cytometry has many applications in the fields of immunology, cancer biology, and clinical diagnostics.<sup>10</sup> For example, in HIV diagnostics, flow cytometry is used to monitor levels of CD4+ T lymphocytes; this information is used to determine the progression of the disease and develop effective treatments. Although flow cytometry has proven to be an extremely powerful tool for the analysis of biological samples, the high cost of these devices, along with their mechanical complexity and bulky nature, has greatly limited their use in point-of-care diagnostic applications. In addition, specialized personnel are required to operate flow cytometers and multiple sample pre-treatment steps are often necessary, resulting in significant operational costs.

After having computationally and experimentally optimizing our 3D hydrodynamic focusing via curved microfluidic channel, in this research work we have taken a major step towards moving our research into clinical studies. As shown in equation 1,  $(D_1 - D_0)$  is the decrease in thickness of the sample flow in the Y direction, which directly results from the interfacial shear rate and is proportional to the elongation of the sample flow along the axial direction of the channel;  $\beta$  is the material parameter of the sample flow, similar to the Passions ratio, and dependent on liquid properties of sample flow such as viscosity and density;  $\dot{\gamma}$  is the interfacial shear rate which depends on the velocity difference between sample flow and sheath flow;  $t_0$  is the initial time at the inlet when two co-flowing fluids interact;  $t$  is the co-flowing time or the time of the shearing action applied on the interface of the two co-flowing fluids;  $U_v$  is the velocity of the vertical sheath flow;  $U_s$  is the velocity of the sample flow;  $a$  is the average thickness of the sample flow; and  $(L_1 - L_0)$  indicates the stretched length (elongation) of the co-flow interface.

$$(D_1 - D_0) \propto \int_{t_0}^t \beta \dot{\gamma} dt \propto \int_{t_0}^t \beta \left( \frac{U_v - U_s}{a} \right) dt \propto \beta (L_1 - L_0), \quad (1)$$

Figure 1 is the heart of the prototype flow cytometer, showing a fully integrated microfluidic based flow cytometer. The 3D hydrodynamic focusing is attained by utilizing the phenomenon of “microfluidic drifting”<sup>8</sup> within the curved microfluidic channel. This is achieved in a two-step procedure as shown in Figure 1. Presently we have one laser integrated into the chip via single mode optical fiber and three detection fibers for forward scattering, side scattering and fluorescent scatter.

In the second part of this work, we aimed to install everything inside a box to move towards prototyping out flow cytometer. The microfluidic chip is installed inside the box shown in figure 2: A Prototype of a fully functional flow cytometer. The prototype flow cytometer is the first step from lab to clinical use of this work. Moreover, our aim is to show a fully functional low cost, simpler, smaller and easy-to-use flow cytometer.

**Word Count: 547**

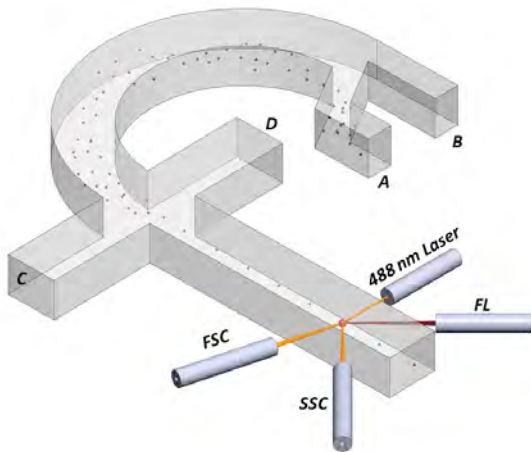


Figure 1: A fully integrated microfluidic flow cytometry device. The device has one input fiber that shines 488nm laser onto the cells of flowing inside the chip. Three detection fibers detect scattering signals.



Figure 2: Phase I prototype of a fully functional flow cytometer with customizable PMT voltages (LCDs). The heart of the flow cytometer, microfluidic 3D cell focusing device, is installed inside the upper compartment of the prototype.

## REFERENCES:

- 1 D. W. Inglis, J. A. Davis, T. J. Zieziulewicz, D. A. Lawrence, R. H. Austin and J. C. Sturm, *J. Immuno. Methods*, 2008, **329**, 151–156.
- 2 D. W. Inglis, K. J. Morton, J. A. Davis, T. J. Zieziulewicz, D. A. Lawrence, R. H. Austin and J. C. Sturm, *Lab Chip*, 2008, **8**, 925–931.
- 3 O. D. Laerum, T. Farsund, *Cytometry Part A*, 1981, **2**, 1-13.
- 4 H. M. Shapiro, R. C. Leif. *Practical flow cytometry*: Wiley-Liss New York, 2003.
- 5 M. Brown, C. Wittwer, *Clin.chem.* 2000, **46**, 1221-1229.
- 6 P. K. Dagur, A. Biancotto, L. Wei, H. N. Sen, M. Yao, W. Strober, R. B. Nussenblatt, and J. P. McCoy, Jr., *J. Autoimmun.* 2011, **37**, 319-327.
- 7 X. Cai, G. Pacheco-Rodriguez, Q. Y. Fan, M. Haughey, L. Samsel, S. El-Chemaly, H. P. Wu, J. P. McCoy, W. K. Steagall, J. P. Lin, T. N. Darling, and J. Moss, *Am. J. Respir. Crit. Care Med.* 2010, **182**, 1410-1418.
- 8 X. Mao, A. A. Nawaz, S. C. S. Lin, M. I. Lapsley, Y. Zhao, J. P. McCoy, W. S. El-Deiry, and T. J. Huang, *Biomicrofluidics*, 2012, **6**, 024113.

# POSTERS

# EXCITATION OF MULTIPLE SURFACE-PLASMON-POLARITON WAVES AT METAL/CHIRAL-SCULPTURED-THIN-FILM INTERFACES

*Sema Erten and Akhlesh Lakhtakia*

The Pennsylvania State University, Department of Engineering Science and Mechanics,  
212 EES Building, University Park, PA USA 16802

---

The aim of this study was to excite multiple surface-plasmon-polariton (SPP) waves guided by the planar interface of a metal and a periodically nonhomogeneous sculptured thin film (STF) at an optical frequency [1].

We excited multiple surface-plasmon-polariton (SPP) waves guided by the interface of a metal and a chiral sculptured thin film (STF). Chiral STFs made by thermally evaporating NaF and either 3, 4, or 5 periods in thickness were deposited on a metal film by oblique angle deposition accompanied by substrate rotation, each period being 300 nm, for plasmonic investigations in the Turbadar-Kretschmann-Raether (TKR) configuration. Reflectances were measured for a range of incidence angles for both p- and s-polarization states of the incident monochromatic light. Several reflectance minimums independent of the thickness of the chiral STF were obtained, indicating that multiple SPP waves had been excited.

Thermal evaporation method was chosen to deposit metal thin films as well as chiral STF samples reported in this study. The first step was to cut pre-cleaned glass slides in to approximately 2 cm × 2 cm pieces. The glass slides were then sonicated for 10 min each side. If further cleaning was necessary, they were cleaned by hand using ethanol and deionized water. After the cleaning process, glass slides were attached to a substrate holder which is a plate placed in the vacuum chamber. The glass slides were positioned as close as possible to the center of the substrate holder for a reasonable uniformity in the film thickness.

The second step to prepare a sample for optical experiments was to deposit an aluminum film approximately 30 nm in thickness on a pre-cleaned glass slide. The aluminum film was deposited by thermal evaporation and the thickness was monitored *in situ* by a QCM. Prior to deposition, the vacuum chamber was pumped down to a base pressure of  $\sim 10^{-6}$  Torr. In order to evaporate the source material, a current of  $\sim 32$  A was passed through a tungsten boat containing bulk aluminum. The glass slide was located normal to the incoming aluminum vapor flux. During deposition, the substrate holder was rotated about the

axis passing normally through its surface at a constant angular speed of 2 rps.

Following the deposition of aluminum, a chiral STF of sodium fluoride was deposited. The substrate was held at an oblique angle, referred as  $\chi_v$ , which is measured between the direction of incoming vapor flux and the substrate plane. For this study,  $\chi_v$  was fixed at either 10° or 15°. To obtain a chiral morphology, the substrate was stepwise rotated about the normal axis at 18°/step with a 54.25 s break between steps. The chiral STFs fabricated were of 3, 4, or 5 periods, each period being 300 nm in thickness.

The experimental set-up used to detect the excitation of surface-plasmon-polariton waves was based on the Turbadar-Kretschmann-Raether (TKR) configuration [2]. This set-up was implemented on an optical bench. The TKR configuration uses a high-refractive-index prism to couple incident light to a metal/dielectric interface, in order to excite SPP waves if possible. A 45°-90°-45° BK7 prism was used.

The overall reflectance was detected by a photomultiplier detector. The measured photodetector voltage for the incident light is denoted by  $U_{inc}$  and the measured photodetector voltage for the reflected light is indicated by  $R$ . The graphs showing the reflectance  $R/U_{inc}$  of the incident light versus the angle  $\theta$  were plotted. The results were classified according to thickness of the deposited STFs, the linear polarization state of the incident light (p-polarized or s-polarized). The arrows in the graphs indicate the reflectance minimum points.

The optical data for 30-nm-thick aluminum film deposited on a glass substrate were taken for both p- and s- polarization states of the incident light. The data presented in Fig. 1 show that there is no reflectance dip; instead, the reflectance increases as  $\theta$  increases. In contrast, for p-polarized incident light in Fig. 2 there is a reflectance minimum at  $\theta = 44.20^\circ$ . These results are well matched with the previous experiments of others [3] as well as with theory [4, 5].

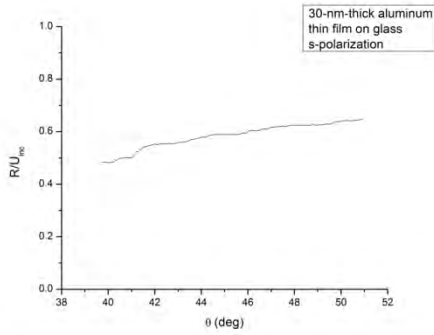


Figure 1. Measured reflectance  $R/U_{inc}$  as a function of the angle of incidence  $\theta$ , for a 30-nm-thick aluminum thin film. The incident plane wave is s-polarized and the free-space wavelength is 633 nm. The TKR configuration with a 45°-90°-45° prism was used.

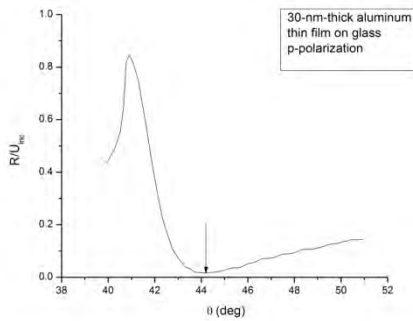


Figure 2. Same as Figure 1 except that the incident plane wave is p-polarized.

Experiments conducted for Glass-slide/Aluminum/NaF-Chiral-STF structure have shown that there are reflectance minimums independent of the thickness of the chiral STF. These dips in Figs. 3 and 4 indicate the launch of up to six different SPP waves, three by incident p-polarized light and three by incident s-polarized light.

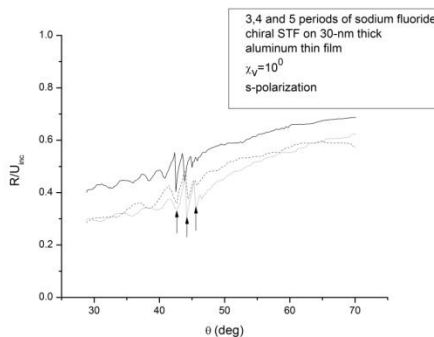


Figure 3. Measured reflectance  $R/U_{inc}$  as a function of the angle of incidence  $\theta$ , for a 900-nm-, 1200-nm- or 1500-nm-thick sodium fluoride chiral STF on a 30-nm-thick aluminum film. The incident plane wave was s-polarized and the free-space wavelength was set 633 nm. The TKR configuration with a 45°-90°-45° prism was used.

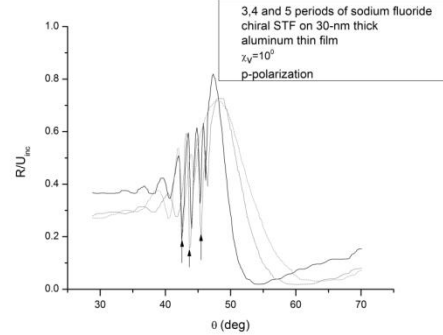


Figure 4. Same as Figure 3 except that the incident plane wave is p-polarized.

The experimental observation of multiple SPP waves confirms the theoretical predictions [4, 6] and experimental studies done earlier [7]. The number of different SPP waves is very likely equal to 3, all of which were launched by both p- and s-polarized incident light.

For further research, different materials can be used to deposit both sculptured thin films and metal thin films. Other deposition methods can be used to prepare samples. To ensure that the reflectance minimums found are evidence of excited SPP waves but not of waveguide modes, more experiments should be conducted.

## REFERENCES

- [1] Erten, S., Excitation of Multiple Surface-Plasmon-Polariton Waves at Metal/Chiral-Sculptured-Thin-Film Interfaces, M. S. Thesis, Pennsylvania State University, University Park PA, USA (2011).
- [2] Kretschmann, E. and Raether, H., "Radiative Decay of Nonradiative Surface Plasmons Excited by Light," *Z. Naturforsch. A* **23**, 2135-2136 (1968).
- [3] Simon, H. J., Mitchell, D. E. and Watson, J. G., "Surface Plasmons in Silver Films-A Novel Undergraduate Experiment," *Am. J. Phys.* **43**, 630-636 (1975).
- [4] Polo, Jr., J. A. and Lakhtakia, A., "On the Surface Plasmon Polariton Wave at the Planar Interface of a Metal and a Chiral Sculptured Thin Film," *Proc. R. Soc. Lond. A* **465**, 87-107 (2009).
- [5] Mansuripur, M. and Li, L., "What in The World Are Surface Plasmons," *Opt. Photon. News* **8** (5), 50-55 (1997 May issue).
- [6] Motyka, M. A. and Lakhtakia, A., "Multiple Trains of Same-Color Surface Plasmon Polaritons Guided by the Planar Interface of a Metal and a Sculptured Nematic Thin Film," *J. Nanophoton.* **2**, 021910 (2008).
- [7] Gilani, T. H., Duskhkina, N., Freeman, W. L., Numan, M. Z., Talwar, D. N. and Pulsifer, D. P., "Surface Plasmon Resonance due to the Interface of a Metal and a Chiral Sculptured Thin Film," *Opt. Eng.* **49**, 120503 (2010).

## A FRACTIONAL PRESSURE-VOLUME MODEL OF CEREBROSPINAL FLUID DYNAMICS IN HYDROCEPHALUS

*Justin Kauffman* \*

Department of Engineering Science and Mechanics  
Pennsylvania State University  
University Park, PA 16802, USA  
Email: jak5378@psu.edu

*Corina S. Drapaca*

Department of Engineering Science and Mechanics  
Pennsylvania State University  
University Park, PA 16802, USA  
Email: csd12@psu.edu

### ABSTRACT

*Hydrocephalus is a brain disorder caused by abnormalities in the cerebrospinal fluid (CSF) circulation. The treatment is surgical in nature and often has poor outcomes. The first mathematical model for studying the CSF pressure-volume relationship in hydrocephalus was proposed by Marmarou in the 1970s. In this paper we generalize Marmarou's model using fractional calculus. Our model captures the multiscaling temporal behavior of the CSF dynamics that has not been studied so far.*

### INTRODUCTION

Hydrocephalus is a serious brain disease caused by abnormalities in the cerebrospinal fluid (CSF) circulation resulting in ventricular dilation, brain compression and sometimes an increase in the intracranial pressure. The treatment is surgical in nature and aims to reverse the dilation of the ventricles by diverting the CSF flow. However, the response of patients with hydrocephalus to treatment continue to be poor [1]. Therefore, there is an urgent need to design better therapy protocols for hydrocephalus.

An important step in this direction is the development of predictive mathematical models that better explain the fundamental science behind this disorder. Marmarou [2] proposed the first mathematical model of CSF pressure-volume relationship for studying hydrocephalus. However, the model fails to fully capture the complex CSF dynamics controlled by CSF-brain tissue interactions. In this paper we propose a generalization of Marmarou's model using fractional calculus. By replacing the first order temporal derivative in Marmarou's model by a fractional order derivative we introduce an inhomogeneous clock that continuously connects the global macroscopic and the local mi-

croscopic time scales. We use the modified Adomian decomposition method proposed in [3] to solve analytically the proposed fractional order differential equations. In the case of constant CSF infusion, our results show temporal multiscaling behavior of the CSF dynamics.

### FRACTIONAL MODEL OF CSF DYNAMICS

The conservation law of CSF hydrodynamics says that the rate of CSF formation  $I_f$  equates the sum of the rate of change of CSF volume  $V$  stored in the brain ventricles  $\frac{dV}{dt}$  and the rate of CSF absorption defined in [2] as  $\frac{P-P_d}{R}$ , where  $P$  is the CSF pressure,  $P_d$  is the pressure of the venous system and  $R$  is the resistance of CSF to absorption. We consider two cases: 1)  $\frac{dV}{dt} = \frac{1}{K} \frac{dP}{dt}$ , and 2)  $\frac{dV}{dt} = \frac{1}{KP} \frac{dP}{dt}$  (from [2]), where  $K > 0$  is a constant. We model the effect of the complex (and barely known) CSF-brain dynamics on the CSF pressure by using the fractional order Caputo derivative of order  $0 < \alpha \leq 1$ :

$$D_0^\alpha P(t) = \frac{1}{\Gamma(1-\alpha)} \int_0^t \frac{dP}{d\tau} (t-\tau)^{-\alpha} d\tau, \quad (1)$$

where  $\Gamma(z) = \int_0^\infty e^{-t} t^{z-1} dt$  is the Gamma function. Thus the conservation laws of the CSF hydrodynamics for the two proposed cases are respectively:

$$D_0^\alpha P + \frac{K}{R} P - K \left( I_f + \frac{P_d}{R} \right) = 0. \quad (2)$$

\*Address all correspondence to this author.

and

$$D_0^\alpha P + \frac{K}{R} P^2 - K \left( I_f + \frac{P_d}{R} \right) P = 0. \quad (3)$$

Eq.2 is a fractional linear differential equation, while Eq.3 is a fractional Riccati differential equation for  $P$  which reduces to Marmarou model when  $\alpha = 1$ . Both equations are solved for the initial condition  $P(0) = P_0$ . We consider the case of constant CSF infusion when  $I_f = F = \text{constant}$ . Using the modified Adomian decomposition method [3], the solutions to Eqs.2 and 3 are given by:

$$P(t) = \sum_{n=0}^{\infty} a_n t^{n\alpha} \quad (4)$$

For simplicity we take  $P_d = P_0$ . The solution to Eq.2 is therefore:

$$P(t) = P_0 + \frac{FK}{\Gamma(\alpha+1)} t^\alpha - \frac{FK^2}{R\Gamma(2\alpha+1)} t^{2\alpha} + \dots \quad (5)$$

The solution to Eq.3 is of the form (4) where  $a_0 = P_0$ ,  $a_{n+1} = \frac{\Gamma(n\alpha+1)}{\Gamma(n\alpha+\alpha+1)} (-\beta_1 a_n - \beta_2 A_n)$ ,  $n = 1, 2, 3, \dots$ ,  $\beta_1 = -K(F + P_d/R)$ ,  $\beta_2 = K/R$  and the so-called Adomian polynomials are given by:  $A_n = \sum_{k=0}^{\infty} a_{n-k} a_k$ ,  $n = 0, 1, 2, \dots$

## RESULTS

We used the following parameters [2]:  $P_0 = P_d = 100$  [mmH<sub>2</sub>O],  $K = 1/0.4343$  [mL<sup>-1</sup>min<sup>-α</sup>],  $R = 609$  [mmH<sub>2</sub>O/mL/min],  $F = .02$  [ml/min]. The solutions to Eqs.2 and 3 for different values of  $0 < \alpha \leq 1$  are plotted in Figs.1 and 2, respectively. In both cases the initial slope of the pressure decreases as  $\alpha$  increases. Also, for a given  $\alpha < 0.5$  the shapes of the solutions to Eqs. 2 and 3 are similar.

During the slow development of hydrocephalus when CSF accumulates in the ventricles due to a constant CSF infusion, the CSF pressure increases abruptly initially and then its increase slows down due to controllers such as special proteins in the brain that provide volume regulation and osmotic pressures. The shapes of the CSF pressure for  $\alpha < 0.5$  shown in Figs.1 and 2 capture this physics of the CSF-brain interactions.

## CONCLUSION

In this paper we presented a fractional pressure-volume model for the CSF dynamics for studying hydrocephalus. Our model captures some aspects of the CSF-brain interactions which have not been modeled so far.

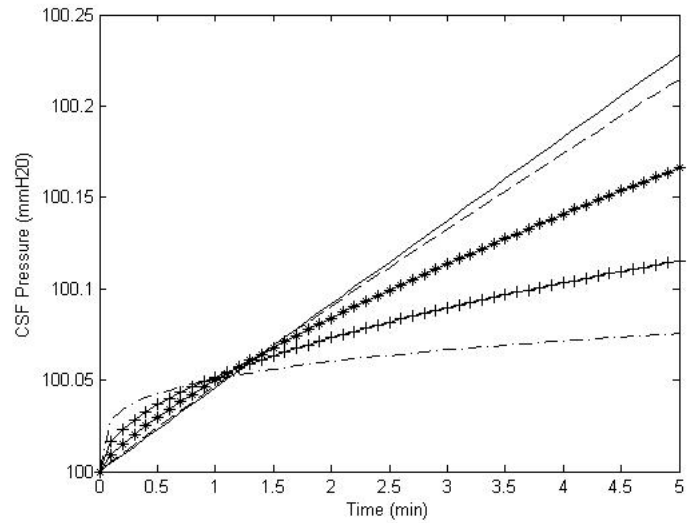


**FIGURE 1.** The shapes of the CSF pressure for Eq.2:  $\alpha = 0.25$  (-),  $\alpha = 0.5$  (+-),  $\alpha = 0.75$  (\*-),  $\alpha = 0.95$  (-),  $\alpha = 1$  (solid line).

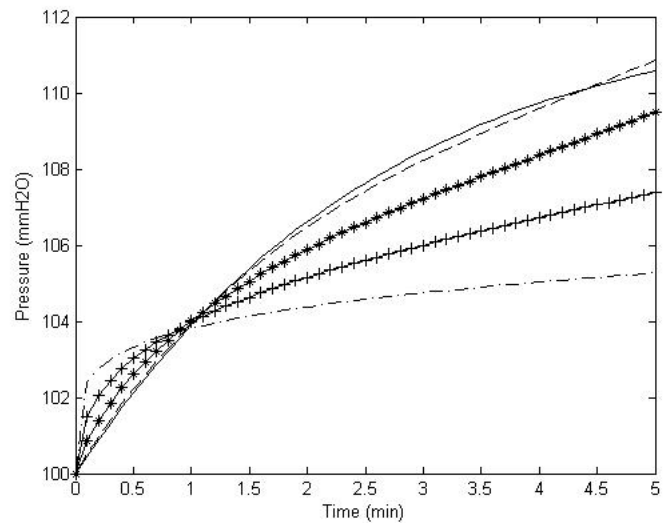


**FIGURE 2.** The shapes of the CSF pressure for Eq.3:  $\alpha = 0.25$  (-),  $\alpha = 0.5$  (+-),  $\alpha = 0.75$  (\*-),  $\alpha = 0.95$  (-),  $\alpha = 1$  (solid line).

## REFERENCES

- [1] Tuli S. *et al.* *Pediatric Neurosurg.*, **30**(1):11-15, 1999.
- [2] Marmarou A. *et al.* *J.Neurosurg.*, **48**: 332-344, 1978.
- [3] Duan J.-S. *et al.* *Appl.Math.Comp.* **218**: 8370-8392, 2012.

## A NOVEL TECHNIQUE IN THIN FILM GROWTH: BIASED TARGET DEPOSITION

*Hitesh A. Basantani,<sup>1,2</sup> William R. Drawl,<sup>2</sup> Mark W. Horn,<sup>1</sup> Thomas. N. Jackson.<sup>2</sup>*

<sup>1</sup>Department of Engineering Sciences, the Pennsylvania State University, University Park, PA 16802, USA

<sup>2</sup>Materials Research Institute, the Pennsylvania State University, University Park, PA 16802, USA

<sup>3</sup>Department of Electrical Engineering, the Pennsylvania State University, University Park, PA 16802, USA

Thin films form an essential component of all microelectronic and micro-mechanical systems. This poster will introduce a novel sputtering tool recently installed in the Nanofab known as the *Biased Target Deposition System (BTD)*. BTD combines the versatility of both conventional sputtering and ion beam deposition to offer unique advantages in a host of thin-film areas including *magnetic materials, binary/ternary alloys, and reactive thin-film growth*.

In conventional sputtering methods either the plasma for sputtering can only be struck at higher operating pressures or at moderately low pressures (2-100 mTorr) where a permanent magnet is used to concentrate the electrons and thereby ignite the plasma. However, these methods are limited in their capability by operating pressures, limited parameter space in conditioning of the growing films.

The BTD technique on the other hand uses an external plasma source (broad beam, unfocused, low energy ion gun) to remotely create plasma that illuminates the sputtering target and the substrate. Because the energy of the ions created is less than the sputter threshold, no sputtering as a result of this ion beam takes place. The target is then negatively biased to values that cause sputtering of the target material. Figure 1 describes the geometry of the BTD tool. Because the ion gun geometrically faces the substrate, the ion energy of the gun can be tailored to 'condition' the growing film. The absence of a magnet facilitates sputtering of magnetic materials as well as the **uniform erosion** (>90%) of the target material.

A built in Residual Gas Analyzer (RGA) offers real time monitoring and control of process gases making it useful in reactively sputtering. The nature of the tool makes precise atomically controlled, smooth and

repeatable deposition of magnetic materials such as Nickel, Cobalt, and Iron thin-films possible. These characteristics make it indispensable for applications ranging from shape memory alloys (NiTi), to magnetic sensors and magneto-optical devices.

Thin films of magnetic elements elements such as nickel, cobalt and iron have been explored. Initial results show high deposition rates ( $\approx 1\text{\AA}/\text{s}$ ), smooth (Figure 2, Roughness  $<5\text{\AA}$  by AFM) and uniform ( $\geq\pm 4\%$  on 4" wafer, determined by lithography and profilometry) thin films have been deposited. The electrical resistivity of these films (Figure 3) is comparable to those found in the literature. The inherent stress in as deposited thin films is shown to be a function of sputtering voltage (essentially a function of arriving ion/atom ratio on the substrate).

Thin insulating films of  $\text{SiO}_2$  are often required in many microelectronic applications including gate oxides in MOSFETs, passivation layer in devices etc. With the option to control the ad-atom mobility and the arriving ion/atom ratio, BTD  $\text{SiO}_2$  thin films were reactively deposited using a 99.99% pure silicon target. The leakage current of the thin film (shown in Figure 4) is found to be  $5 \times 10^{-6} \text{ A/cm}^2$  at 2.5MV/cm (three orders of magnitude higher than that of thermally grown oxide); the breakdown field is found to be 13.9MV/cm (comparable to that of thermal oxide) and the dielectric constant is found to be  $\epsilon = 3.95$  ( $\epsilon_{\text{thermal SiO}_2} = 3.9$ ). Optical characterization of the thin films reveal a refractive index,  $n = 1.48$  ( $n_{\text{thermal SiO}_2} = 1.46$ ) indicating a slight oxygen deficiency.

These initial results show promising prospects for these techniques, especially in depositing magnetic and reactively sputtered materials.

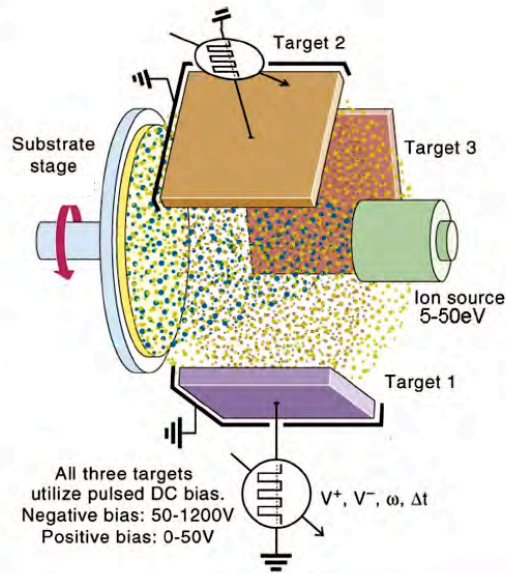


Figure 1. Schematic of Biased Target Deposition

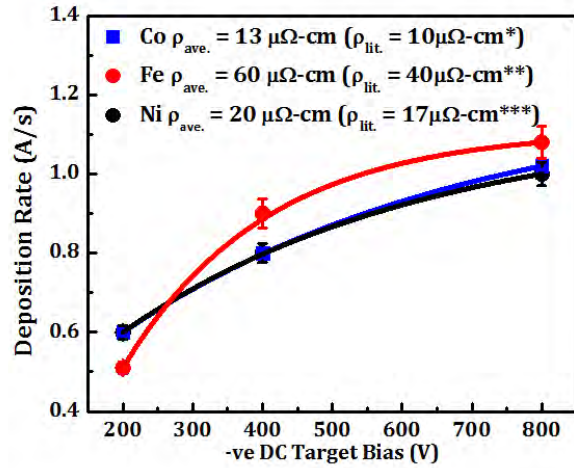


Figure 2. Deposition Rate as a function of target bias

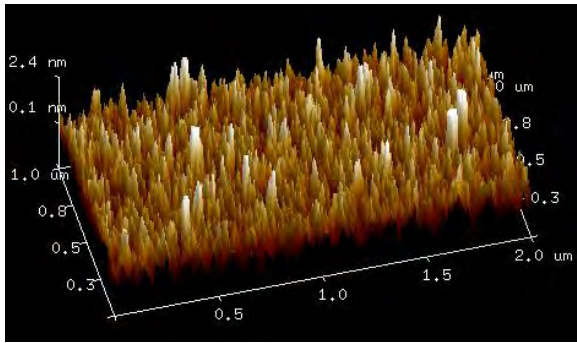


Figure 3. AFM data showing smoothness of Deposited Ni Films as a function of Target Bias (V)

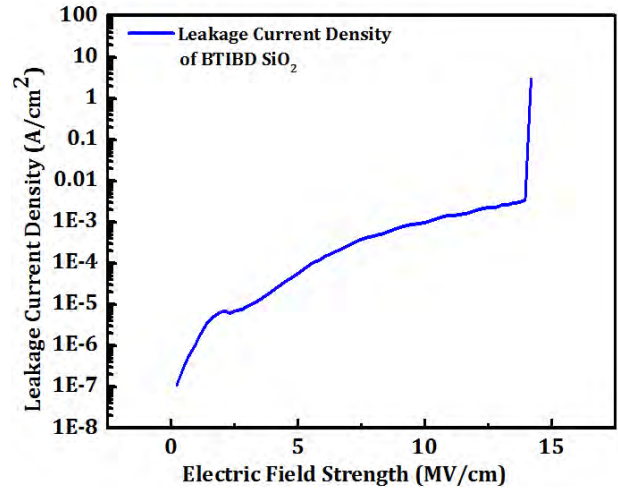


Figure 4. Leakage Current and breakdown field of BTIBD  $\text{SiO}_2$

## REFERENCES:

- \* Ivanova, A. R. *J. Electrochem. Soc.* 1999, Volume 146, Issue 6, Pages 2139-2145.
- \*\* Naoue, M., M. Yamaga, and N. Terada. *IEEE Transactions on Magnetics* 21.5 (1985): 1900-902.
- \*\*\* Johnson, B. C. *Journal of Applied Physics* 67.6 (1990): 3018.

# COARSE-GRAINED MODELING OF RECEPTOR-MEDIATED ENDOCYTOSIS OF NANOPARTICLES

Changjin Huang, Yao Zhang, and Sulin Zhang\*

Department of Engineering Science and Mechanics, The Pennsylvania State University,  
University Park, Pennsylvania 16802, USA.

Receptor-mediated endocytosis is a process by which cells engulf and internalize nanometer-sized targets, driven by the specific binding of the ligands on the surface of targets with vary both in size and shape. As cells encounter targets with such diversity, one wonders how target geometry impacts endocytosis. Several *in vitro* studies have been conducted to address this question<sup>1,2</sup>. However, a fundamental understanding of the kinetics of endocytosis is still lacking, owing to the insufficient resolution in real-time imaging of the endocytic dynamics. Analytical models have exclusively focused on spherical targets mainly because of the intractable mathematical treatment of membrane bending energy in wrapping nonspherical targets<sup>3-5</sup>. In theory, computational models can simulate endocytosis of targets of any geometry. However, owing to the high computational costs, existing numerical models often use very high ligand and receptor densities in order to accelerate the simulations<sup>6,7</sup>. This imposes unrealistically very high driving force to endocytosis, which not only concealed the role of target shape in endocytosis, but also created an inaccurate picture of the actual role of target size. As a result, the role of target size and shape remains largely elusive.

Herein, we report that, using a coarse-grained fluid membrane model, both target size and shape modulate endocytic kinetics. Generally, all the NPs are able to initiate wrapping. However, membrane wrapping is retarded or inhibited at a later stage of wrapping due to the increased

the receptors on the membrane of cells. Examples of targets include viruses of various kinds and synthetic nanoparticles (NPs) for bioimaging and drug delivery carriers, all of which membrane curvature energy barrier. At given ligand density, size decisively determines the completion of the endocytosis. Shape, on the other hand, primarily impacts the endocytosis pathways and the angle of entry. Taking the endocytic time as a quantitative measure of the kinetics of endocytosis, we point out that NP size, and shape must be optimized in a concerted manner in order to achieve maximized cellular uptake of the NPs.

## REFERENCES:

- [1] B. D. Chithrani, A. A. Ghazani, & W. C. W. Chan. "Determining the size and shape dependence of gold nanoparticle uptake into mammalian cells", *Nano Letters* 6, pp 662-668, 2006.
- [2] F. Zhao *et al.* "Cellular Uptake, Intracellular Trafficking, and Cytotoxicity of Nanomaterials", *Small* 7, pp 1322-1337, 2011.
- [3] S. Zhang, J. Li, G. Lykotrafitis, G. Bao, & S. Suresh. "Size-dependent endocytosis of nanoparticles", *Advanced Materials* 21, pp 419-424, 2009.
- [4] H. Y. Yuan, C. J. Huang, & S. L. Zhang. "Virus-Inspired Design Principles of Nanoparticle-Based Bioagents", *PLoS One* 5, pp e13495, 2010.
- [5] H. J. Gao, W. D. Shi, & L. B. Freund. "Mechanics of receptor-mediated endocytosis", *Proc. Natl. Acad. Sci. U. S. A.* 102, pp 9469-9474, 2005.
- [6] R. Vacha, F. J. Martinez-Veracoechea, & D. Frenkel. "Receptor-Mediated Endocytosis of Nanoparticles of Various Shapes", *Nano Letters* 11, pp 5391-5395, 2011.
- [7] Y. Li, T. Yue, K. Yang, & X. Zhang. "Molecular modeling of the relationship between nanoparticle shape anisotropy and endocytosis kinetics", *Biomaterials* 33, pp 4965-4973, 2012.

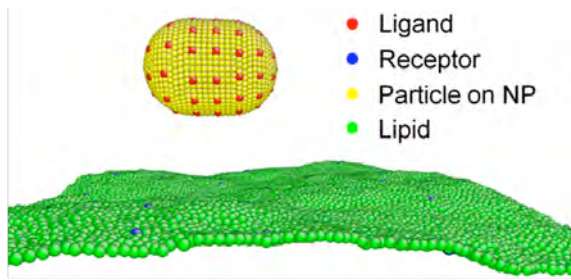


Figure 1. Coarse-grained molecular dynamics model of receptor-mediated endocytosis.

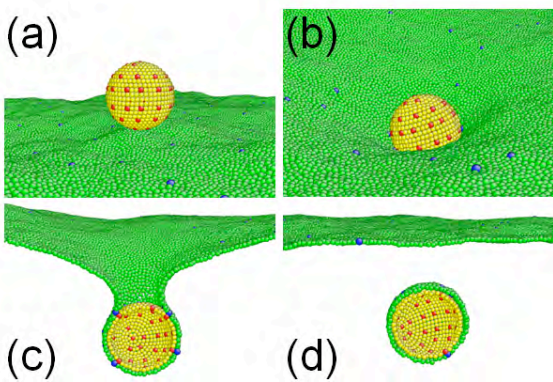


Figure 2. Representative snapshots of the endocytosis dynamics of a spherical NP: (a) docking ( $t=0\tau$ ); (b) partially wrapped ( $t=2850\tau$ ); (c) necking ( $t=25000\tau$ ); (d) fully endocytosed ( $t=27400\tau$ ).

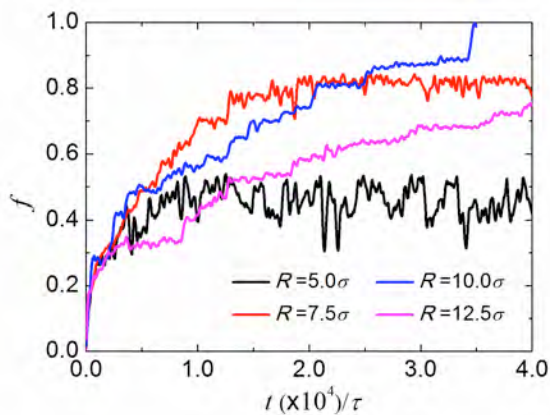


Figure 3. Effect of particle size on the endocytosis process.

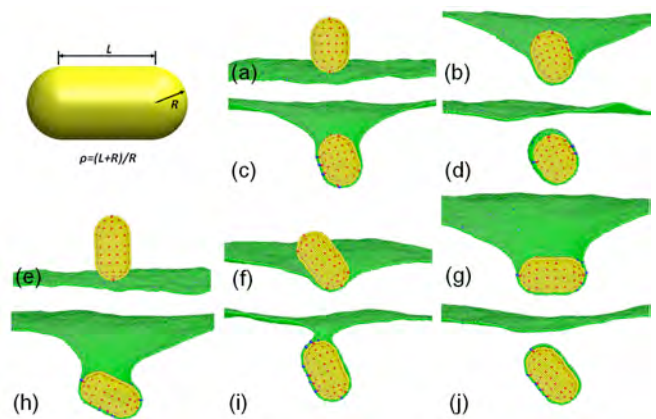


Figure 4. Representative snapshots showing the endocytosis dynamics of rod-like NPs with different aspect ratios: (a-d)  $\rho=2$ , and (e-j)  $\rho=3$ .

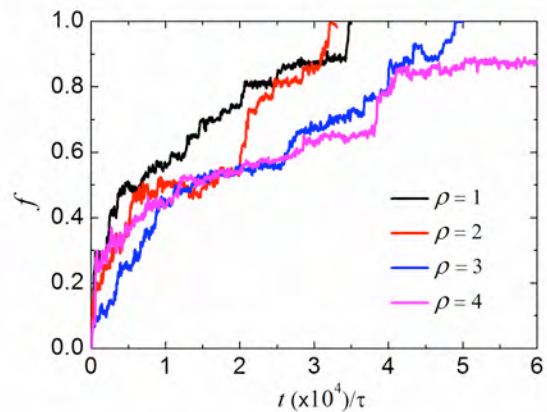


Figure 5. Effect of particle shape on the endocytosis process.

## **MACRO FIBER COMPOSITE TRANSDUCERS: USES IN SONAR APPLICATIONS**

*B. Golder and R. Meyer*

Engineering Science and Mechanics Department, Penn State, PA-16802, USA

The Macro Fiber Composite patch (MFC) is a low profile actuator and sensor invented by NASA in 1996 [1]. The MFC utilizes a layer of rectangular piezo-ceramic rods that are encapsulated between layers of adhesive, polyimide film and electrodes as seen in Figure 1. The MFC is assembled in a sealed package which makes them durable and easy to incorporate into established and novel sonar structures [1]. The MFC is bonded to a steel plate resulting in a bimorph transducer. The ease of assembly along with the price of the MFC itself makes this a very cost effective transducer to produce. The MFC's are manufactured in a variety of configurations and materials providing many extra possible design parameters.

The unique configuration of the MFC provides a new tool in the development of transducers for underwater sound. MFC can be easily incorporated into traditional sonar structures such as the flexural transducer structures seen in Figure 2a. MFC's also provide an opportunity to develop novel structures which take advantage of the unique properties of the MFC as seen in Figure 2b. The structure would convert the radial bend of the bimorph to a linear response. The structure will provide the unidirectional sound path while maintaining the high power low frequency performance of traditional flexural transducers.

The Finite Element Analysis (FEA) program Atila has built in features for MFC's which allows for easy testing of designs. Comparison of FEA to experimental results did not agree and warranted further investigation. The disagreement is clearly observed in the model of the MFC alone which is shown in Figure 4. The first resonance frequency of the model does agree with the experimental values, however the first anti-resonance and all higher resonance frequencies do not agree. Not seen in Figure 4 is a large disagreement in the value of impedance. The impedance was normalized to compare resonances of the sets of data, in actuality the impedance of the model is many orders of magnitude less than the experimental data.

A simple transducer was made by bonding an MFC to an eighth inch steel plate using epoxy. As with the MFC by itself the impedance was again many orders of magnitude less for the model. For the simple transducer the first two resonance frequencies have reasonable agreement with the model.

Further systematic analysis of modeling parameters is needed in order to make the model exactly match the resonance and deformation of the experimental transducer.

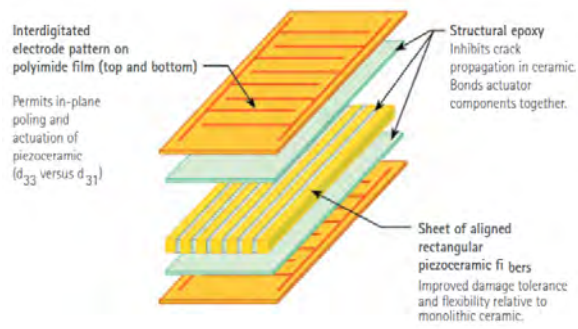


Figure 1: MFC structure schematic [1]

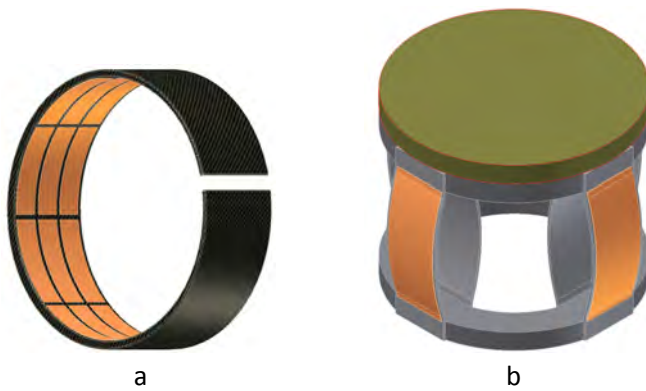


Figure 2: Two designs for sonar devices incorporating MFC's

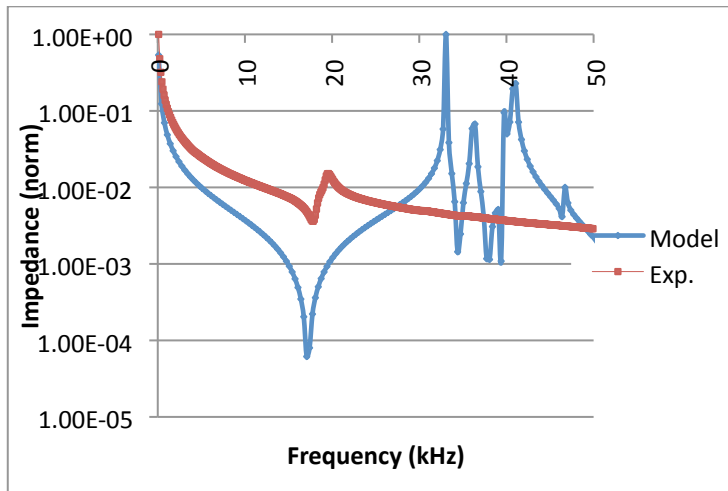


Figure 4: Plot of impedance vs. frequency for MFC model & experimental data

**References:**

[1] Smart materials corp, "Data Sheets," 2012. [Online]. Available: <http://www.smart-material.com/Datasheets.html>. [Accessed 7 August 2012].

**Paper**

**Poster**

## **COARSE-GRAINED MODELING OF HUMAN ERYTHROCYTE MEMBRANE**

*Yao Zhang, Changjin Huang and Sulin Zhang*

Department of Engineering Science and Mechanics, Pennsylvania State University,  
University Park, Pennsylvania 16802, USA

The human erythrocyte (red blood cell, RBC) is the most common blood cell which transports oxygen from lung to human tissues through blood circulation. RBC frequently squeezes through narrow capillaries during its 120-days life span and shows remarkable ability to undergo reversible large deformation. This extraordinary ability stems from the unique structure of its membrane. Compared with phospholipid membranes of other cells, RBC membrane possesses an additional spectrin network tethered to phospholipid layer. This spectrin network provides extra resistance to the shear. In previous studies, RBC membrane

models only including fixed spectrin-network were used to capture the deformability of RBC. However, those models missed the fluidity of membrane and could not simulate the remodeling of cytoskeleton since the spectrin networks were fixed. Experiments show that the remodeling of spectrin network plays an essential role on the RBC shape and its remarkable deformability[1]. On the base of a one-particle thick membrane model[2], we propose a coarse-grained model of RBC membrane including both spectrin network and phospholipid layer to study mechanical properties of RBC membrane.

Paper

Poster

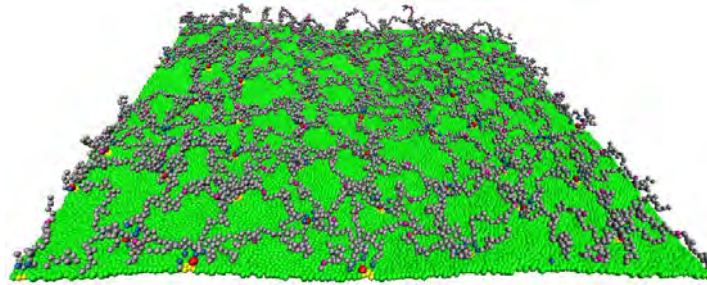


Figure 1. schematic of RBC membrane model

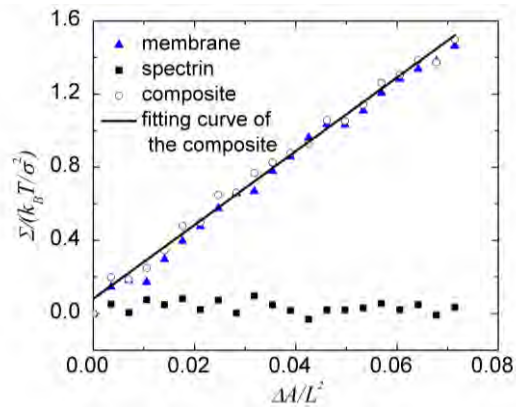


Figure 2. Area compression modulus of RBC membrane model

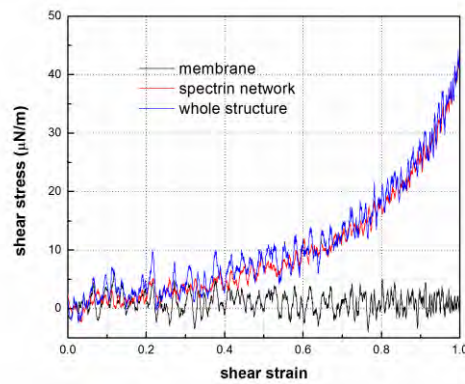


Figure 3. shear stress-strain response of RBC membrane model

#### REFERENCE:

1. Li, J., et al., Cytoskeletal dynamics of human erythrocyte, in PNAS. 2007. p. 4937-4942.
2. Yuan, H., et al., One-particle-thick, solvent-free, coarse-grained model for biological and biomimetic fluid membranes. Physical Review E. **82**(1): p. 011905.

**Paper**  
**Poster**

## **IN SITU TEM STUDY LITHIATION-DELITHIATION OF GALLIUM NANODROPLETS**

*Wentao Liang, Sulin Zhang*

Department of Engineering Science and Mechanics, Pennsylvania State University,  
University Park, Pennsylvania 16802, United States

Anode materials, such as Si and Ge, have recently attracted enormous attentions for their much higher theoretical capacity than the conventional Li-graphite anodes. However, the potentiality of these anode materials is significantly comprised due to the lithium insertion/extraction induced huge volume change and subsequent fracture. Here we report in situ transmission electron microscopy (TEM) studies of the electro-chemical cycling behavior of gallium

nanodroplets. We observed void nucleation, growth and diminishment during the lithiation/delithiation cycles, demonstrating the self-repairability of the Gallium Nanodroplets (GaNDs). We attribute the void growth and diminishment to the repeated liquid-to-solid phase transitions during lithiation/delithiation cycles. The self-healing capability of liquid gallium suggests the promise of hybrid anodes consisting of high-capacity materials such as Si and liquid gallium.

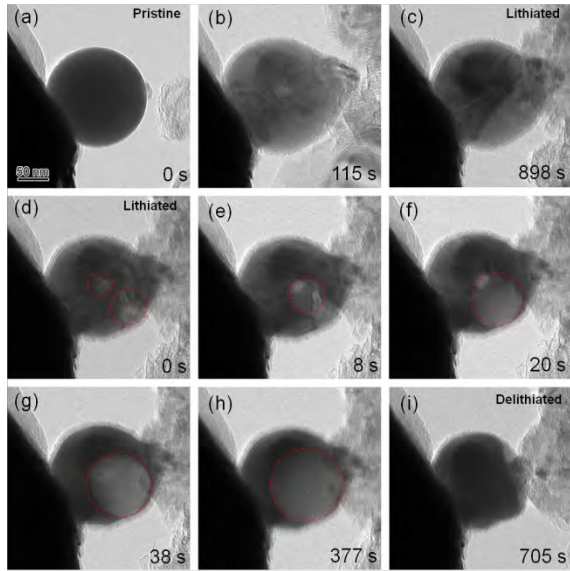


Fig. 1. Morphology evolution of the Gallium nanodrop during the first cycle.

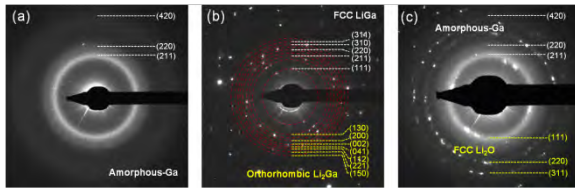


Fig. 2. The typical EDPs (Electron Diffraction Patterns) showing the phase transformations from amorphous Ga phase to crystalline  $Li_xGa$  phase and back to amorphous Ga phase during cycling process.

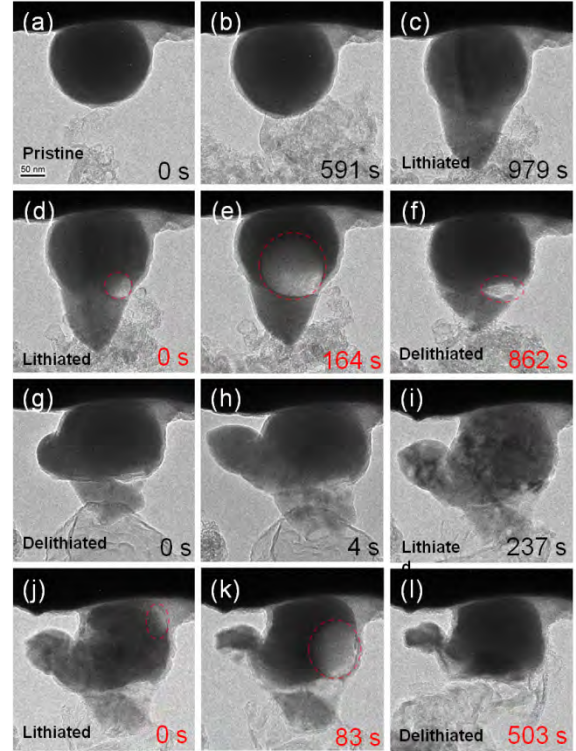


Fig. 3. Morphology evolution during multiple cycling process of Gallium nanodrop.

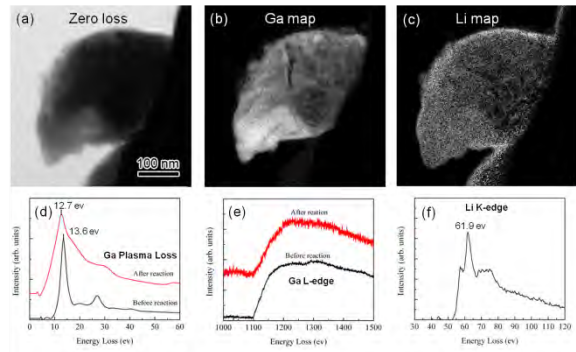


Fig. 4. EELS spectra and maps of Ga, and Li elements of Ga nanodrop after lithiation.

# Alkali Free Boroaluminosilicate Glasses for High Energy Density High Temperature Power Electronic Capacitors

*P. Dash<sup>1,2</sup>, E. Furman<sup>2</sup>, C. G. Pantano<sup>2,3</sup>, M. T. Lanagan<sup>1,2</sup>*

<sup>1</sup>Department of Engineering Science and Mechanics, Penn State, PA, 16802

<sup>2</sup>Materials Research Institute, Penn State, PA, 16802

<sup>3</sup>Department of Material Science and Engineering, Penn State, PA, 16802

One of the biggest engineering innovations in the 20<sup>th</sup> century was the development of capacitor, a solid-state power conversion device, which led to dramatic changes in the way electric power is stored and distributed. New technology in power electronic products like hybrid electric vehicles, implantable medical devices and high power microwave systems require ultra-capacitors with decreased volume, weight, cost and energy densities greater than 30 J/cm<sup>3</sup>. Recently, thin low alkali borosilicate glasses have shown promising trends to be used as high energy density material with energy density as high as 35 J/cm<sup>3</sup> owing to their high dielectric breakdown strength (12 MV/cm). These glasses maintain low dielectric loss up to temperatures of 200°C which is critical for automotive applications with extreme environmental conditions. In addition, thin glass sheets are sufficiently flexible to be wound into a compact capacitor structure. The possibility of fabricating multilayer storage capacitors with this thin glass has created considerable interest in recent years for potential application to DC-bus capacitors in electric vehicles. So far polypropylene is the most commonly used dielectric in hybrid vehicles but they have low relative permittivity (2.1), energy densities approaching 10 J/cm<sup>3</sup>, they occupy significant volume in the capacitors and have limited high temperature capabilities. If these polymer based capacitors are replaced by glass capacitors it would result in five times decrease in capacitor volume which would certainly have a significant impact on the growth of hybrid vehicles which have increased by more than ten fold over the last few years.

Therefore, this study focuses on understanding the complex phenomenon of dielectric breakdown by studying intrinsic material properties (electrical conductivity and dielectric constant), extrinsic microstructural features (surface roughness and inclusions) and experimental conditions. This would help in further enhancing the energy density of these glass capacitors.

Breakdown studies have shown increase in breakdown strength with decreasing glass thickness. The characteristic electrical breakdown field strength increased from 400 MV/m to 1100

MV/m as the glass substrate thickness decreased from 58 μm to 5 μm, respectively. To further investigate structural changes resulting in dielectric breakdown, the glass was poled under several voltage and temperature conditions. Thermoelectric treatment of these glasses under high voltage (500V-2000V) and temperature (250°C-550°C) leads to depletion layer formation beneath the anode due to migration of monovalent and divalent cations.

Activation energies for ionic conduction of alkaline earth and alkali ions in these glasses have been estimated using thermally stimulated depolarization current (TSDC) and AC impedance spectroscopy techniques. TSDC measurements confirm the transport of Na<sup>+</sup> and Ba<sup>2+</sup> cations from below the anode with activation energy of 0.8 eV and 1.7 eV for Na and Ba motion respectively. This ionic transport contributes to ionic conduction in glasses. Low frequency impedance spectroscopy results have also confirmed inhomogeneity in a poled glass due to formation of cation depleted space charge layer.

Migration of positive cations from the depletion layer increases the resistance of that layer resulting in all the voltage dropping across the thin depleted layer. This enables the glass to support fields closer to its intrinsic breakdown strength. Second order non-linear optical measurements demonstrate that the thickness of this depletion layer depends on mobile ion concentration in the glass, poling temperature, applied electric field and is limited by the intrinsic breakdown strength of the glass. Beyond this field, electronic conduction in the depleted layer results in eventual breakdown of the sample. The electronic conduction observed was mainly due to Pool Frenkel emission of electrons in the space charge region.

Using high field TSDC and low frequency AC impedance spectroscopy we have demonstrated a technique to determine the activation energy for alkali and alkaline earth ion transport in glasses. We have also reported mixed alkaline earth effect on electrical conduction in glasses, which to the best of our knowledge has not been reported elsewhere. Due to the high dielectric breakdown strength of these glasses we were also able to study

electronic conduction under high electric fields and understand mechanisms contributing to dielectric breakdown in glasses.

Summarizing these results it is suggested that the combination of high intrinsic breakdown strength, high intrinsic Weibull modulus, high-temperature performance stability, low dielectric loss and graceful failure observed in thin glass samples all point to their potential use as high energy storage devices.

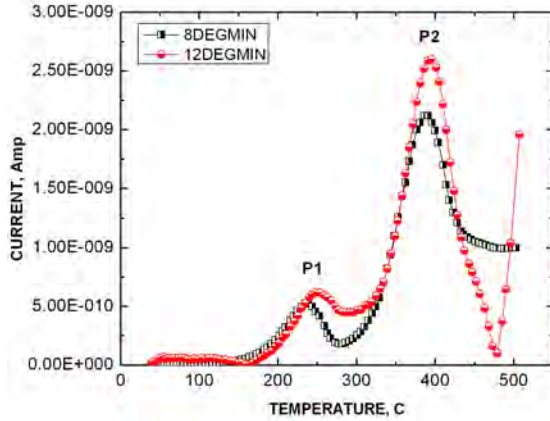


Figure 1: TSDC plot for 50  $\mu\text{m}$  thick AF45 glass poled under a DC bias of 2 kV for two hours at 550°C. P1 and P2 shows the peak associated with the relaxation of Na and Ba cations respectively.

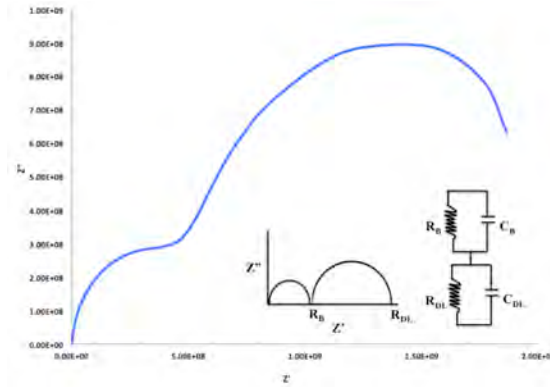


Figure 2: Complex resistivity plot of poled AF45 at 823 K in a frequency range of 0.01 to 1000 Hz. The insets show an ideal Cole-Cole plot for a two RC circuit model.  $R_b$ ,  $R_{DL}$ ,  $C_b$ ,  $C_{DL}$  are the resistance and capacitance of the bulk and depletion layer respectively in the thermoelectrically poled glass.

Table 1 Variation of depletion layer thickness with applied electric fields.

Poling Field (kV)	Depletion Layer thickness ( $\mu\text{m}$ )	Internal Field ( $10^9 \text{ V/m}$ )
22	6.8	3.23
20	6.4	3.12
15	4	3.75
10	7	1.42

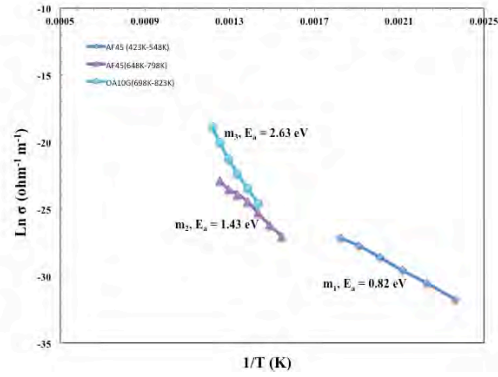


Figure 3: Variation of  $\ln$  conductivity with temperature for AF45 and OA10G at 0.05 Hz obtained from the complex capacitance data.



Figure 4: Second harmonic microscopy image showing depletion layer thickness in 50  $\mu\text{m}$  Ba-Boroaluminosilicate glass poled at 22 KV and 25°C.

## Reference

- [1] N. J. Smith, B. Rangarajan, M. T. Lanagan, C. G. Pantano, Materials Letters 63 (2009) 1245-1248.
- [2] D. E. Carlson, K. W. Hang, G. F. Stockdale, J. Amer. Ceram. Soc. 57 (1974) 295-300.
- [3] Akira Doi, J. of Mater. Sc. 22 (1987) 761-769.
- [4] G. De Mey and W. De Wilde, Elsevier sequoia S.A, (1974) 301-304.
- [5] A.E.Owen, Phys. and Chem. of Glasses 7 (1976) 174-192.
- [6] P.A. Timson, P. Wickens, Elsevier Sequoia S.A. (1970) R55-R58.
- [7] A. Servini, A. K. Jonscher, Thin Solid Films, 3 (1969) 341-365.
- [8] R. M. Catchings, J. Appl. Phys. 50 (1979) 2813-2816.

## **Composite Ni-Encapsulated Particles for Cold-Spray: Hexagonal Boron Nitride, Aluminum, Nickel**

Maryam Neshastehriz, Ivi Smid, Al Segall, Tim Eden

Self-lubricating coatings can improve the performance of contacting surfaces and extend component lifetimes by reducing the coefficient of friction and/or specific wear. In this study, self-lubricating coatings of several metal- and hexagonal-boron-nitride particles in a nickel matrix were investigated. The self-lubricating coatings were created via cold spray. Relatively thick nickel encapsulation was required to aid in coating bonding and formation, and was achieved via electroless Ni plating. The encapsulation process was found to be scalable and amenable to relatively small particles. Once deposited on (e.g.) aluminum or titanium substrates, the coatings were analyzed for bond-strength, micro-hardness, coefficient of friction, and reciprocating wear behavior. The cold spray process can be used for the deposition of such composite particles to produce coatings which possess very attractive physical and mechanical properties, such as reciprocating wear resistance, reduced friction, and high adhesive strengths relative to pure Ni coatings.

# A COMPARISON OF FLUID-STRUCTURE INTERACTION COUPLING ALGORITHMS USING THE FINITE ELEMENT METHOD

*J. Sheldon*

Engineering Science and Mechanics Department, Penn State, PA-16802, USA

The modern design process depends heavily on computational models which simulate experiments that would be difficult or expensive to perform physically. These models utilize governing equations which mathematically reproduce the desired physics. Structural experiments are often modeled using computational solid mechanics packages, while flow problems are simulated with computational fluid dynamics packages; however, there are many multi-physics problems which cannot be properly modeled without including the coupled fluid-structure interaction (FSI). Such models have been used in the medical field for blood flow through blood vessels [1] or heart valves [2], in the Naval field for underwater explosions [3] and implosions [4], and in the aerospace field for parachute clusters [5], to give only a few examples.

The main challenge in FSI is coupling the effects from solid deformation with those of the fluid flow on the fluid-structure interface. There are two canonical coupling methods for FSI, partitioned and monolithic. The partitioned method involves solving the governing equations in a segregated manner until an equilibrium solution is reached, while in the monolithic method they are solved simultaneously in a combined system of equations. The partitioned approach ranges from weakly-coupled to strongly-coupled, where the strength of coupling, from a physical sense, refers to how much deformation the fluid causes on the solid, with more deformation requiring stronger coupling and therefore more coupling iterations.

We present a third coupling strategy, which we call the “partly-monolithic” method, that combines aspects of both the partitioned and monolithic methods. In this approach, diagrammed in Figure 1, the physical domains (the solid and fluid domains) are solved monolithically, while the non-physical computational mesh is solved iteratively.

Typically, partitioned schemes for FSI are viewed as easier to implement than monolithic schemes and as requiring less computational resources. Conversely, monolithic schemes are viewed as challenging to implement and necessitating longer run-times [6]. The trade off comes in that monolithic coupling is always strongly-coupled, and therefore will generally produce more accurate results than a weakly-coupled partitioned method [7].

We developed a finite-element FSI model using the open source finite element library deal.ii. We model our fluids as incompressible, linearly viscous fluids with the Navier-Stokes equations in the arbitrary Lagrangian-Eulerian reference frame. Our solids are modeled as St. Venant-Kirchhoff materials with a two-field formulation of the elasticity equations in the Lagrangian reference frame. Our mesh is modeled by an elastostatics equation for a neo-Hookean material with arbitrarily defined material properties. The standard Galerkin finite-element formulation is used for the solid, fluid, and mesh, with Taylor-Hood elements used for the fluid. The Crank-Nicolson method is implemented for the time discretization.

Using the method of manufactured solutions, we verify that the individual fluid and solid components produce solutions which accurately solve their governing equations. We perform a numerical validation study against results provided by Turek and Hron [8].

Turek and Hron [8] also provide an FSI benchmark case with results. The domain for this benchmark is shown in Figure 2 and a visualization of results is shown in Figure 3. We present a comparison between Turek and Hron's results to this benchmark case and those from our FSI software, for each different coupling algorithm we implemented: partitioned coupling, monolithic coupling, and partly-monolithic coupling. We examine how the different algorithms perform based on their accuracy to Turek and Hron's results and the speed at which they generate a solution.

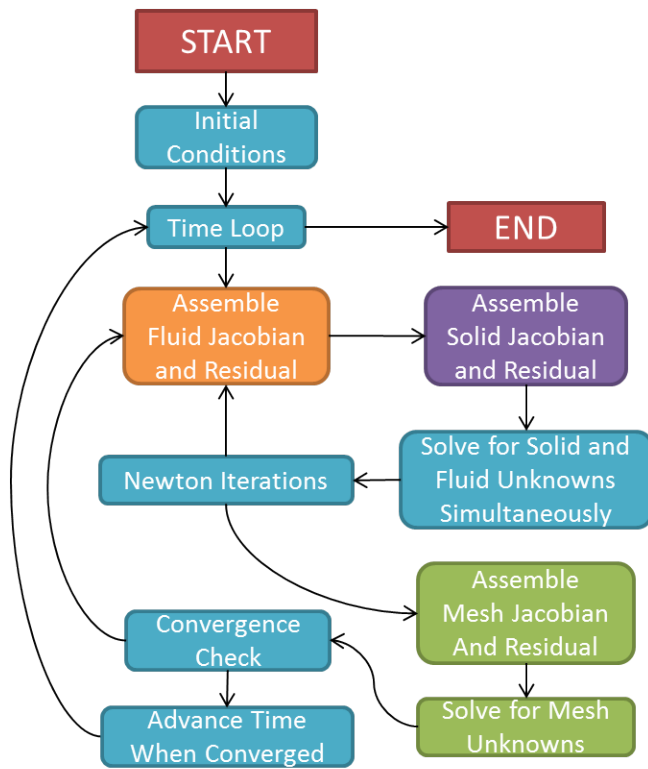


Figure 1. Flowchart demonstrating the partly-monolithic FSI algorithm.

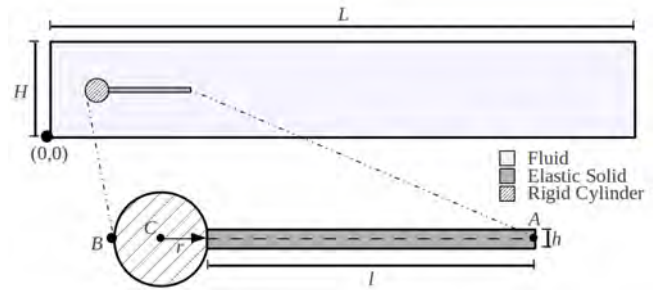


Figure 2. Turek and Hron [8] FSI benchmark domain: a two-dimensional FSI problem where a fluid is flowing through a channel from left to right. Slightly offset from the middle of the channel is a rigid cylindrical obstruction with an elastic flag attached to it.

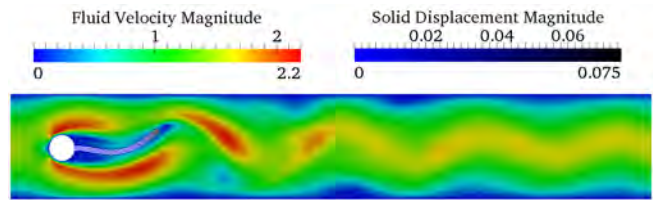


Figure 3. Visualization of FSI benchmark: flow field and solid deformation at  $t = 14.5[s]$ . Solid displacement and fluid velocity are shown with their own color scales.

## REFERENCES:

- [1] Bazilevs, Y., V. Calo, Y. Zhang, and T. Hughes (2006) "Isogeometric fluid–structure interaction analysis with applications to arterial blood flow," *Computational Mechanics*, 38(4), pp. 310–322.
- [2] De Hart, J., G. Peters, P. Schreurs, and F. Baaijens (2000) "A two-dimensional fluid-structure interaction model of the aortic valve," *Journal of Biomechanics*, 33(9), pp. 1079–1088.
- [3] McCoy, R. and C. Sun (1997) "Fluid-structure interaction analysis of a thick-section composite cylinder subjected to underwater blast loading," *Composite structures*, 37(1), pp. 45–55.
- [4] Wang, K., A. Rallu, J. Gerbeau, and C. Farhat (2011) "Algorithms for interface treatment and load computation in embedded boundary methods for fluid and fluid–structure interaction problems," *International Journal for Numerical Methods in Fluids*, 67(9), pp. 1175–1206.
- [5] Takizawa, K., S. Wright, C. Moorman, and T. Tezduyar (2011) "Fluid–structure interaction modeling of parachute clusters," *International Journal for Numerical Methods in Fluids*, 65(1-3), pp. 286–307.
- [6] Campbell, R. and E. Paterson (2011) *Fluid–structure interaction analysis of flexible turbomachinery*, Ph.D. thesis, The Pennsylvania State University.
- [7] Michler, C. (2004) "A monolithic approach to fluid-structure interaction," *Computers & Fluids*, 33, p. 839848.
- [8] Turek, S. and J. Hron (2006) "Proposal for numerical benchmarking of fluid-structure interaction between an elastic object and laminar incompressible flow," *Fluid-Structure Interaction*, pp. 371–385.

**Paper  
Poster**

**ESM TODAY**

**IN SITU LITHIATION MECHANICS OF SILICON NANO-ELECTRODES**

*Hui Yang and Sulin Zhang*

Department of Engineering Science and Mechanics  
The Pennsylvania State University  
University Park, PA 16802

**ABSTRACT**

We present an atomistically informed continuum chemo-mechanical model to study the phase evolution, morphological changes, stress generation, large plastic flow, and failure in lithiated silicon nanowires. Our model couples the reaction-diffusion of lithium with the lithiation-induced elasto-plastic deformation. The simulation results show that the lithiation-induced volume expansion in silicon nanowires is highly anisotropic, with predominant expansion along the  $\langle 110 \rangle$  direction, but negligibly small expansion along the  $\langle 111 \rangle$  direction, which agree striking well with existing independent experimental observations. Such kind of apparent anisotropic swelling is critically controlled by the orientation-

dependent lithiation reaction rate at the atomically sharp phase boundary between the crystalline core and amorphous shell, namely the mobility of an atomically sharp amorphous-crystal interface (ACI). Our modeling results also underscore the importance of structural relaxation by plastic flow behind the moving phase boundary. The atomistically informed modeling framework not only sheds light on the lithiation-mediated failure in nanowire-based electrodes, but also provides a basis for simulating the morphological evolution, stress generation, and failure in high-capacity electrodes for the next-generation lithium-ion batteries.

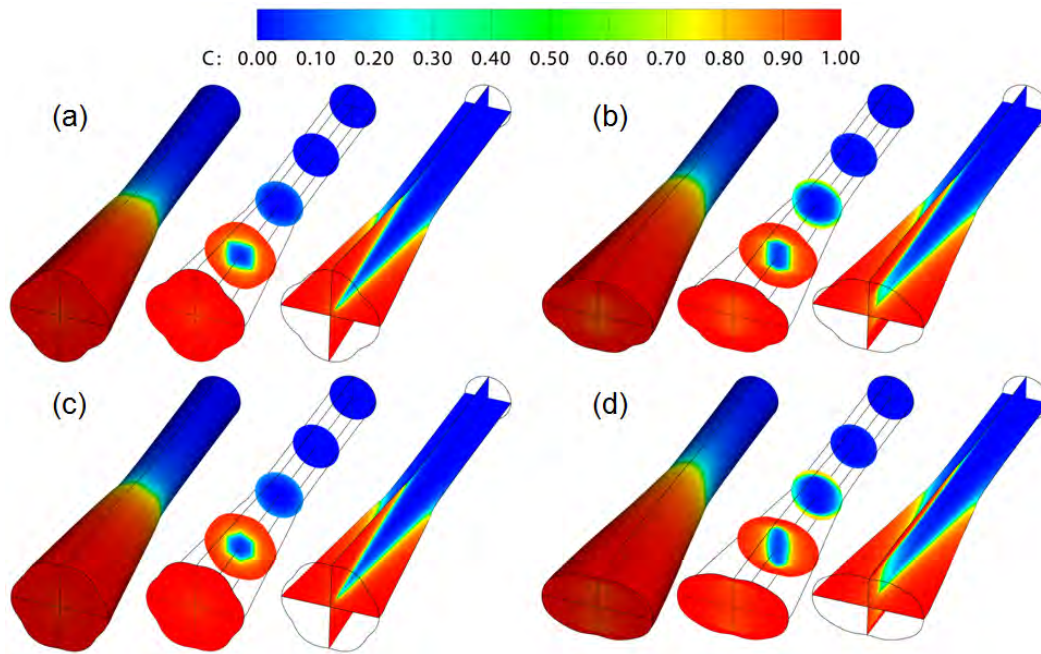


Figure 1: Chemomechanical modeling of the phase transitions and morphological evolutions in (a):  $\langle 100 \rangle$ , (b):  $\langle 110 \rangle$ , (c):  $\langle 111 \rangle$ , and (d):  $\langle 112 \rangle$  silicon nanowires upon lithiation. Colors in the image represent the normalized lithium concentration: red denotes the fully lithiated amorphous silicon ( $\text{Li}_{3.75}\text{Si}$ ), and blue the crystalline silicon. Lithium distributions on different cross-sections of the nanowires are also shown in the second and third columns of each case.

## References

- [1] S. W. Lee, M. T. McDowell, J. W. Choi, Y. Cui, "Anomalous Shape Changes of Silicon Nanopillars by Electrochemical Lithiation", *Nano Lett.*, vol. 11, pp. 3034-3039, 2011.
- [2] X. H. Liu, H. Zheng, L. Zhong, S. Huang, K. Karki, L. Q. Zhang, Y. Liu, A. Kushima, W. T. Liang, J. W. Wang, J.-H. Cho, E. Epstein, S. A. Dayeh, S. T. Picraux, T. Zhu, J. Li, J. P. Sullivan, J. Cumings, C. Wang, S. X. Mao, Z. Z. Ye, S. Zhang, J. Y. Huang, "Anisotropic Swelling and Fracture of Silicon Nanowires during Lithiation", *Nano Lett.*, vol. 11, pp. 3312-3318, 2011.
- [3] X. H. Liu, J. W. Wang, S. Huang, F. Fan, X. Huang, Y. Liu, S. Krylyuk, J. Yoo, S. A. Dayeh, A. V. Davydov, S. X. Mao, S. T. Picraux, S. Zhang, J. Li, T. Zhu, J. Y. Huang, "In situ atomic-scale imaging of electrochemical lithiation in silicon", *Nat. Nanotechnol.*, vol. 7, pp. 749-756, 2012.
- [4] H. Yang, S. Huang, X. Huang, F. Fan, W. Liang, X. H. Liu, L.-Q. Chen, J. Y. Huang, J. Li, T. Zhu, S. Zhang, "Orientation-Dependent Interfacial Mobility Governs the Anisotropic Swelling in Lithiated Silicon Nanowires", *Nano Lett.*, vol. 12, pp. 1953-1958, 2012.

## PROBING FAST BIOMOLECULAR PROCESS USING TIME-CONTROLLED CHEMICAL WAVEFORMS IN MICROFLUIDIC CHANNELS

Daniel Ahmed<sup>a</sup>, Hari S. Muddana<sup>c</sup>, Mengqian Lu<sup>a</sup>, Jarrod French<sup>b</sup>, Brian Kiraly<sup>a</sup>, Xiaole Mao<sup>a</sup>,  
Xiaoyun Ding<sup>a</sup>, Peter J. Butler<sup>c</sup>, Andreas Manz<sup>d</sup>, Stephen J. Benkovic<sup>b,1</sup> and Tony Jun  
Huang<sup>a,d,1,2</sup>

<sup>a</sup>Department of Engineering Science and Mechanics, <sup>b</sup>Department of Chemistry, <sup>c</sup>Department of Bioengineering, The Pennsylvania State University, University Park, PA 16802 USA

Generating chemical waveforms and switches in microfluidic devices with the flexibility to control the various signal attributes has important implications for high-throughput characterization of dynamic chemical<sup>1</sup> and biological processes<sup>2</sup>. For example, dynamic switching or concurrent application of different chemical stimuli is desired for studying dynamic systems such as cell signaling pathways<sup>1</sup> or cascades of chemical reactions.<sup>2</sup> Although considerable progress has been achieved in spatial regulation of chemical stimuli, *i.e.*, generation of chemical gradients<sup>1</sup>, the temporal regulation has received little attention. To date little progress has been made in achieving chemical waveforms or switching of multiple stimuli with milliseconds temporal resolution, which is important to study some of the fastest processes in cells.

In this work we demonstrated ultrafast, programmable chemical waveform and switching generation using acoustically activated bubbles. The schematic diagram of our chemical waveform concept is shown in Fig. 1a. The two inlets were infused with dye and buffer solutions respectively. An air bubble was trapped at the fluid-fluid interface within the horse-shoe structure. An air bubble trapped in a liquid medium acts as a focusing agent of acoustic energy in the presence of an acoustic field. Upon activation of the bubble, the microstreaming rapidly transported and interchanged the liquids in the double-ring recirculation regions. Consequently, when the bubble stops oscillating, the mixing developed by microstreaming stops and the concentrations revert to their original states. Direct translation of electrical signals into chemical waveforms enables programming all the typical features of a function generator (Fig. 2).

Fig. 3a shows the schematic diagram of the device used to demonstrate switching between two different chemical signals, *i.e.* a binary logic circuit. Two horseshoe traps with different dimensions with resonant frequencies of 29.5 kHz and 14.7 kHz respectively were positioned at the two liquid-liquid interfaces (Fig. 3a). The widths of these horse-shoe structures were selected based on their independent actuation. Minimal cross-excitation of these bubbles at the above frequencies was negligible as determined by a microstreaming bead test (Fig. 3b). When bubble A alone is activated at  $f = 14.7$  kHz, the red dye mixed with water filling the region of interest with red dye (Fig. 3c and d, bottom panel). Conversely, when bubble B alone is activated at  $f = 29.5$  kHz, the blue dye mixes with water filling the region of interest with blue dye (Fig. 3d, top panel). Switching between the red and blue dyes was achieved by programming the piezoelectric transducer to alternate between the two excitation frequencies in an oscillatory fashion, such that when bubble A is excited, bubble B remains stationary, and vice versa (Fig. 3e). One could program the transducer to achieve any desired combination of the two signals and each signal may independently access all of the functions of the waveform generator, including frequency and amplitude modulation.

**Word Counts: 440**

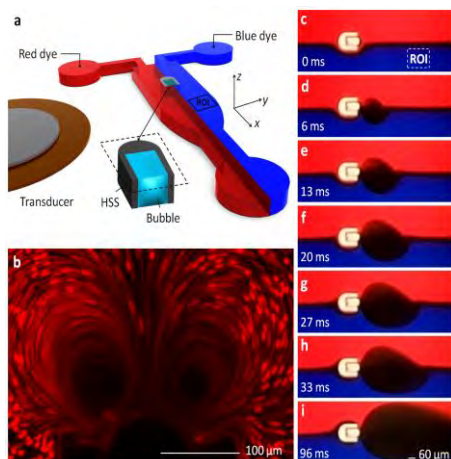


Figure 1: Concept of waveform generation. (a) Schematic of the experimental setup. The piezoelectric transducer, which generates low intensity acoustic waves, is placed adjacent to the microfluidic channel on a cover glass slide. The acoustic waves drive the bubble trapped in the HSS. (b) Microstreaming on particles during bubble oscillation on the x-y plane. (c-i) The mixing of red and blue dyes by microstreaming is captured by high-speed imaging technique.

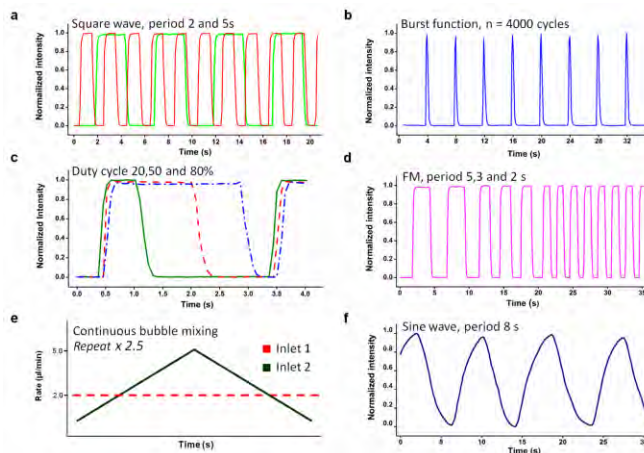


Figure 2: Generation of various chemical waveforms. The region of interest for the output waveform was chosen 500  $\mu\text{m}$  past the recirculation zone, in the bottom half of the channel, Fig 1(c). (a) Square wave. (b) Burst mode (c) Duty cycle. (d) Tunable frequency. (e) Graph of flow rate utilized in achieving amplitude modulation. (f) Sine wave.

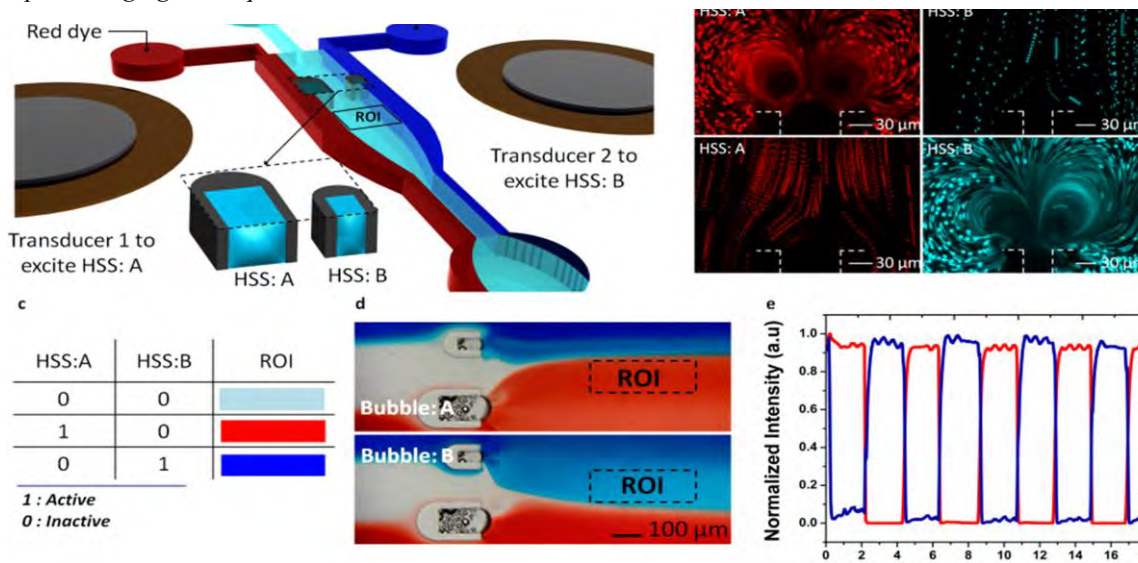


Figure 5: Bubble based switching of blue and red food dyes. (a) Schematic of the experiment setup. The microfluidic fluidic channel contains HSSs of different. (b), Top, microstreaming visualization (red) of bubble trapped in HSS: A, while no streaming is observed in bubble trapped in HSS: B at an excitation frequency of 14.7 kHz. Bottom, microstreaming effect (blue) in bubble trapped in HSS A and no effect on HSS: B at an excitation frequency of 29.5 kHz. (c) Table showing the concept of binary logic circuitry. (d) Result showing the switching mechanism between blue and red dyes. (e) Graph of experimental data for switching between red and blue food dyes in our selected ROI marked in d

## REFERENCES:

- [1] Rocheleau, J. V. *et al.*, Microfluidic glucose stimulation reveals limited coordination on intracellular  $\text{Ca}^{2+}$  activity oscillations in pancreatic islet. *Proc. Natl Acad. Sci. USA* **101**, 12899-12903 (2004).
- [2] T.S Shimizu, Y. Tu, and H. C Berg, "A modular gradient-sensing network for chemotaxis in Escherichia coli revealed by responses to time-varying stimuli". *Molecular system Biology*, 2010, **6:382**. doi:10.1038/msb.2010.37

## ACOUSTIC SOFT SWIMMERS AND ITS MOTION AT INTERFACES

*Daniel Ahmed<sup>1</sup>, Mengqian Lu<sup>1</sup>, Hari Mudanna<sup>2</sup>, Nitesh Nama<sup>1</sup>, Vincent Crespi<sup>3</sup>, and Tony Jun Huang<sup>1,2</sup>*

<sup>1</sup>Department of Engineering Science and Mechanics, <sup>2</sup>Department of Bioengineering, <sup>3</sup>Department of Physics. The Pennsylvania State University, University Park, PA 16802 USA

**Introduction:** Microswimmers promises in revolutionizing numerous aspects of medicine, such as, delivering drugs or radioactive sources to remote tumor sites within a body. Furthermore, these devices could potentially act as occlusions to intentionally clog a blood vessel to inhibit recirculation of circulating tumor cells (CTCs), and much more in a non-invasive fashion [1]. To this end, we fabricated hollow cylindrical containers that trap asymmetric bubbles. Excitation by an external acoustic field induces propulsion such as translation, rotation and revolution motion, and these characteristics were analyzed in this study.

**Materials and Methods:** The microswimmers were fabricated by sandwiching a droplet of poly (ethylene glycol) (PEG) containing photosensitive initiator within two glass slides separated by 1-150  $\mu\text{m}$  spacers. Hollow cylindrical structures are formed by exposing oligomer to ultraviolet (UV) light for  $< 0.2$  s through an array of ring-shaped transparency masks attached to the field stop of an inverted microscope. Asymmetrical bubbles were obtained by confining air within the cylindrical containers. The particles were then chemically treated, thus allowing repeatable trapping of asymmetric bubbles within the hollow structures when immersed in liquid.

**Results:** Two different PEG swimmers were designed to produce translational motion. One type contains a single bubble and the other contains two bubbles of equal size. The swimmers are placed in a water reservoir (**Fig 1a** for the experimental setup) and are excited by ultrasonic acoustic waves. The bubbles oscillate, acting like micro transducers, in the acoustic field and generate forces thus propelling the swimmer. **Fig 1d-i, Fig 1j-o** show the propulsion for a single-bubble PEG system and a two-bubble PEG system, respectively. The propulsion mechanism is based on the asymmetric bubble configurations. For a single bubble system, there exists one air-liquid interface at which a force can be developed, as seen in the free body diagram in **Fig 1b**. Thus, an unbalance force is applied to the system causing it to accelerate. In the case of two-bubble system, there exist four air-liquid interfaces and each generating force to the surrounding liquid, as shown in the free body diagram in **Fig. 4c**. Since both bubbles trapped within the hollow cylinders are asymmetric and identical, the two curvatures of air-liquid interface on one side are smaller than those on the other. Thus, an unbalanced resultant force is applied in-line with the center of mass. The direction of each swimmer is only determined by their initial orientation, as the force is applied in-line with the objects center of mass. To obtain revolution, a PEG structure was generated with two asymmetric bubbles of different sizes as shown in **Fig. 1p**. Since the bubbles are different in size each of the four air-liquid interfaces has difference curvature and each generates a different force. Again an unbalanced force is generated; however in this case the force is slightly off centre, generating revolution.

**Conclusion:** A novel concept of propulsion demonstrating different type of propulsion: translation, rotation and revolution. Though early stage, we believe that these swimmers will find themselves useful in non-invasive medical surgical needs such as targeted drug delivery, brachytherapy, ablation, etc.

**References:** 1. Nelson BJ, *et al.* 2010. Microrobots for minimally invasive medicine. *Annu. Rev. Biomed. Eng.* 12: 55-85.

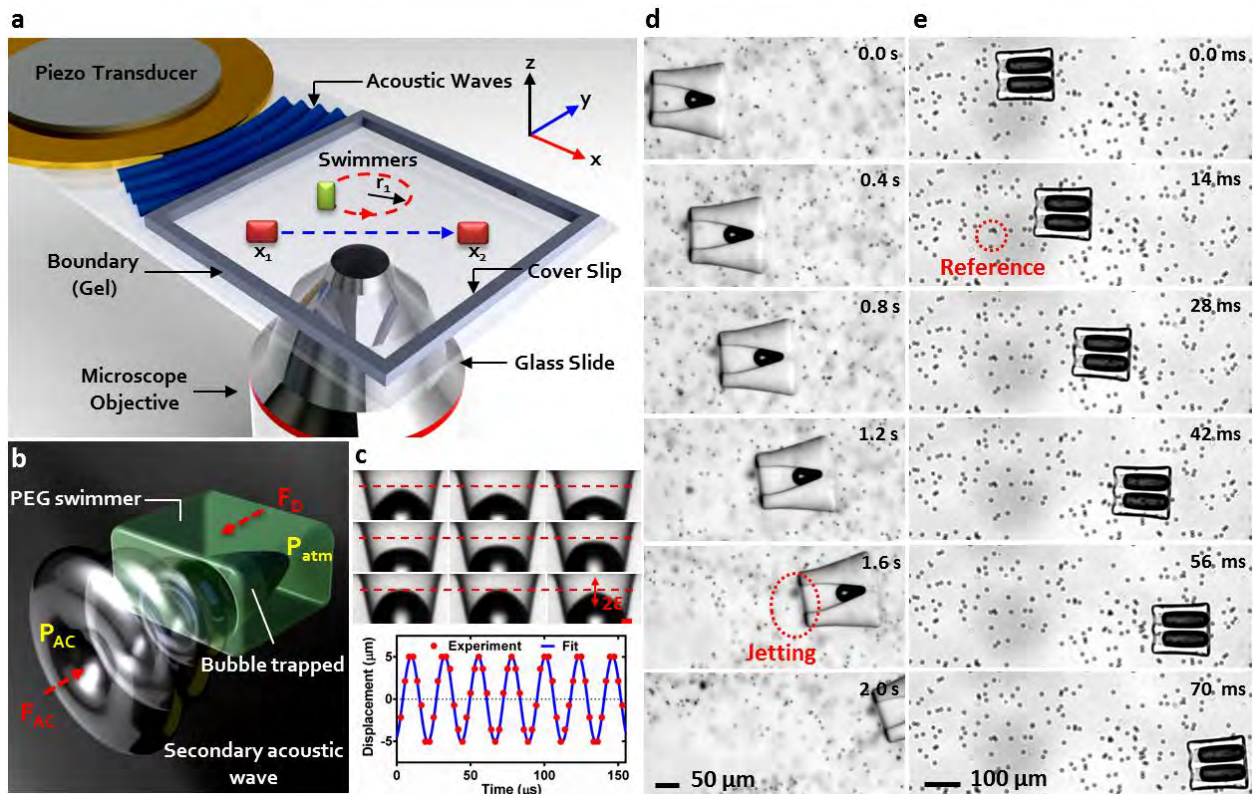


**Fig. 2 Setup, concept and linear motion.** *a.* Schematic of the experimental setup. A piezoelectric transducer, which generates low-intensity acoustic waves is placed adjacent to a cell (water reservoir). Gel or clay was used at the boundary to minimize reflection of acoustic waves. *b.* Free body force diagrams of a bubble PEG composite systems. *c.* Image sequence taken by high-speed recording at 360,000 fps demonstrating the oscillation of bubble, fitted to a sine (solid line). *d.* Image sequence of linear motion (moving left to right) of a PEG swimmer with a bubble trapped at the centre when exposed to an acoustic field (see also Supporting Movie M2). Note the expulsion of particles at 1.6 seconds. *e.* Image sequence of a linear motion (moving left to right) of a PEG swimmer trapping multiple bubbles within the containers (see also Supporting Movie M3). The swimmers propel in the same trajectory as their initial orientation. Note. Attached polystyrene particles on the substrate serves as a reference point for propulsion.

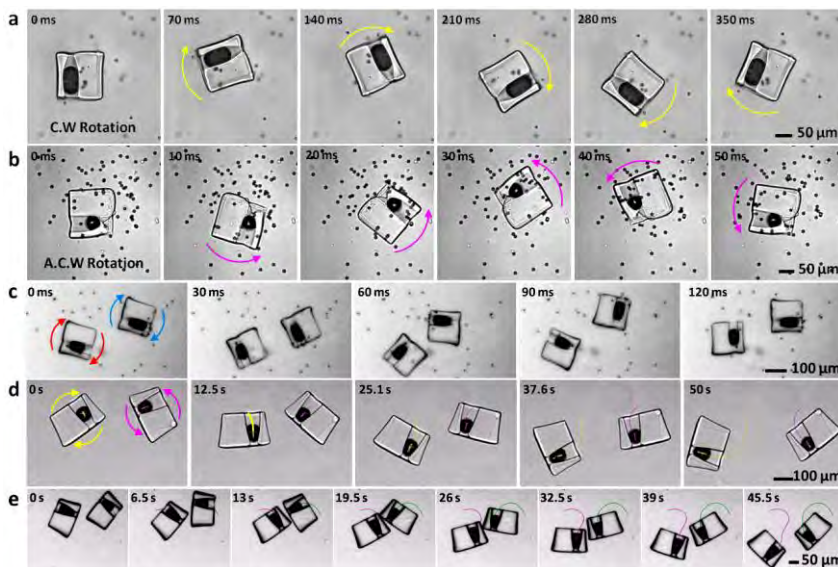


**Fig. 2 Rotational motion.** *a.* Clockwise rotation of a PEG swimmer in water mixed with beads with a bubble trapped off-centered from the center of the mass during bubble oscillation. *b.* Anticlockwise rotation of a PEG swimmer in water when the bubble is trapped opposite to the arrangement, shown in (figure 3a). *c.* Anticlockwise rotation of Multiple swimmer in water. Image sequence of *a, b* and *c* are taken by high-speed recording at 10,000 fps. *d.* Multiple swimmers rotating independently in clockwise and anticlockwise direction in gel. *e.* Swimmers come into contact with each other. *d* and *e* are taken by high-speed recording at 15 fps.

# CHARACTERIZATION OF TITANIUM NITRIDE FORMED VIA LASER-SUSTAINED PLASMA INTERACTION WITHOUT DIRECT IRRADIATION OF THE SUBSTRATE

*A. N. Black, S. M. Copley and J. A. Todd*

Engineering Science and Mechanics Department, Penn State, University Park, PA, 16802, USA

Industries ranging from aerospace to biomedical utilize titanium and its alloys due to their superior strength, high strength-to-weight ratio, low density, high melting point, excellent corrosion resistance, high fracture toughness, good heat transfer properties, gold appearance, and biocompatibility [1, 2]. The poor tribological characteristics of these metals, however, reduce their applicability under severe wear conditions [3]. To enhance these properties, titanium nitride (TiN) coatings are often employed due to their extreme hardness, excellent corrosion and wear resistances, high thermal conductivity, important transport properties, chemical inertness, and gold appearance [4]. Thus, TiN is commonly used for protective coatings on cutting tools and drill bits, diffusion barriers in microelectronics, metal smelting crucibles, optical coatings, and decorative features [5].

Laser nitriding is a process in which laser irradiation melts a titanium surface while under a nitrogen-containing atmosphere. It has been investigated since the 1980s because of its potential as a fast, effective TiN synthesis technique [6]. During laser nitriding, the interaction of the laser melt and species evaporated from the surface produces near-surface plasma. The impact of this laser-induced plasma is a subject of much discussion; some consider it to enhance the coating process [7-9], others say it is detrimental to nitridation [10, 11], while most ignore its potential effects [12-14]. The research to be presented investigates the effect of plasma on a Ti surface without direct laser melting by utilizing laser-sustained plasma (LSP).

LSP, originally referred to as a “continuous optical discharge” is plasma generated by a laser beam in a gaseous atmosphere that can be sustained indefinitely away from any potentially interacting surface [15]. While LSP has been successfully used to deposit diamond [16-18], its potential contributions to the formation of a broad range of hard coating compositions has not been systematically explored. LSP is an optical discharge plasma, similar to a laser-induced plasma. While this optical discharge plasma can be used to melt a surface, it also provides a novel method for studying the influence of plasma on a Ti substrate without the laser beam interacting directly with the surface.

There is an important distinction between the experimental process being presented and conventional laser nitriding. In laser nitriding, the main heat source responsible for melting is the laser beam. In the process under consideration, LSP is the heat source responsible for melting the titanium

substrate. The term LSP nitriding is used to indicate that LSP, and not the laser, is being used as the heat source. The laser is used only to maintain the LSP and does not have any direct interaction with the material being nitrided.

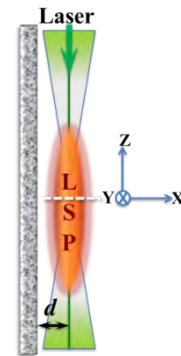


*Figure 1: A side view of the experimental setup showing  $d$ , the distance between the laser centerline (indicated by the green line) and substrate surface. The size and shape of the LSP are shown schematically. The green arrow indicates the direction of the laser beam, while the white, dashed line indicates the location of the laser's focal plane.*

In order to melt the surface without irradiating it, the LSP is translated to a location some distance,  $d$ , from the substrate, as shown in Figure 1. In all cases, it was determined there was no effect from the laser beam on the substrate without the LSP being present. Values for  $d$  tested were between 2 mm and 5 mm. Each distance produced a different melt pattern, as shown in Figure 2. These tests were performed on ASTM grade 2, commercially pure (< 99.5%) titanium plates. Some were processed with the as-received, unpolished, milled surface, while others were polished mechanically prior to LSP exposure. In addition, length of exposure was considered.

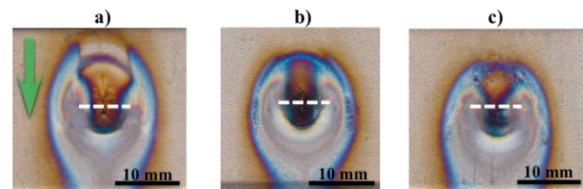


*Figure 2: Macroscale images for the LSP parallel configuration after 5 seconds at: a)  $d = 2$  mm; b)  $d = 2.5$  mm; and c)  $d = 3$  mm.*

During processing, images were collected via a CCD camera with appropriate filters to minimize oversaturation and modified frame-grabbing software, so processing could be visually monitored (see Figure 3). Scanning electron microscopy (SEM) with a backscattered electron (BSE) detector and energy-dispersive x-ray spectroscopy (EDS) were utilized to analyze the initial products of the process, as well as transverse and longitudinal metallographic cross-sections.

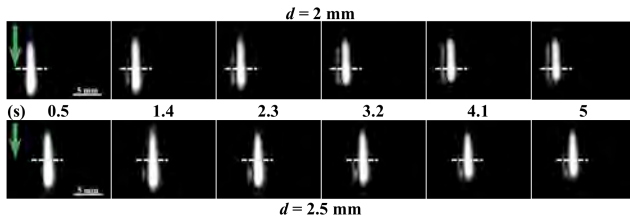


Figure 3: Progression of growth as seen through a 870 nm bandpass filter with 0.6 neutral density filter. The brightest portion of each image shows the LSP with the plate to the left. The green arrows indicate the direction of the laser beam, while the white, dashed lines indicates the location of the laser's focal plane.

Using EDS results in conjunction with the macroscale images seen in Figure 2 and previous literature on nitriding, it was determined that hypo-stoichiometric, near-stoichiometric [19], and hyper-stoichiometric [20] TiN developed at the main impact site. Also present were regions of TiO<sub>2</sub> [21] and locations where a nanoscale layer of TiO<sub>2</sub> covered a deeper layer of TiN [22].

Surface morphologies varied widely between the three values for  $d$  tested.  $d = 3$  mm showed little structure, while the  $d = 2$  mm and  $d = 2.5$  mm samples showed more mature crystallization and evidence of evaporative growth. Cross-sections showed solid and dendritic layers very similar to those seen in laser nitrided TiN. It was also noted that convection assists the permeation of nitrogen into the titanium melt, similar to the convective currents found in laser nitriding.

In addition to SEM and EDS, a focused ion beam was used to take cross-sections of the crystals on the surface for transmission electron microscope (TEM) examination. Diffraction indicates a deformed cubic structure, while electron energy loss spectroscopy (EELS) showed that the crystals have low levels of oxygen which may cause the deformation of the lattice and indicate that the crystals grow while the surface is cooling after the LSP was extinguished.

The regions of high nitrogen concentration, the convective movement within the melt pool, and the surface growth are the most significant structures seen in the LSP nitrided Ti. The faceted crystal growth on the surface and the dendritic layer below it suggest that there are two growth mechanisms

at work during LSP nitriding: one in the melt and another from the vapor.

**Word Count: 868**

- [1] Caron RN and Staley JT. Titanium and Titanium Alloys, in: Dieter GE (Ed.). ASM Handbook, vol. 20. Materials Park, OH: ASM International; 1997.
- [2] Zhang J, Fan D, Sun Y, Zheng Y. Key Eng Mater 2007; 353-358:1745.
- [3] Guo B, Zhou J, Zhang S, Huidi Z, Pu Y, Chen J. Mater Sci Eng A 2008;480:404.
- [4] Tavares J, Coulombe S, Meunier J-L. J Phys D: Appl Phys 2009;42:1020011.
- [5] Wu M. J Alloys Compd 2009; 486:223.
- [6] Spies H-J. Surf Eng 2010; 26:126.
- [7] Akarapu RK, Dua P, Campbell A, Scott D, Nassar A, Todd JA, Copley SM. Proc Mater Res Soc Symp 2007; 1040:Q08.
- [8] Höche D, Rapin G, Kaspar J, Shinn M, Schaaf P. Appl Surf Sci 2007; 253:8041.
- [9] Thomann AL, Sicard E, Boulmer-Leborgne C, Vivien C, Hermann J, Andreatza-Vignolle C, Andreatza P, Meneau C. Surf Coat Technol 1997; 97:448.
- [10] Chen X, Wu G, Wang R, Guo W, Yang J, Cao S, Wang Y, Han W. Surf Coat Technol 2007; 201:4843.
- [11] Kloosterman AB. Surface Modification of Titanium with Lasers. Groningen: Groningen University Press; 1998.
- [12] Jianglong L, Qiquan L, Zhirong Z. Surf Coat Technol 1993; 57:191.
- [13] Raaif M, El-Hossary FM, Negm NZ, Khalil SM, Kolitsch A, Höche D, Kaspar J, Mändl S, Schaaf P. J Phys D: Appl Phys 2008; 41:085208.
- [14] Mridna S, Baker TN. J Mater Process Technol 1998; 77:115.
- [15] Keefer D. Laser-Induced Plasmas and Applications. Radziemski LJ, Cremers DA (Ed.). New York, NY: Marcel Dekker, Inc.; 1989.
- [16] Bolshakov AP, Konov VI, Vostrikov VG, Dubrovskii VY, Kosyrev FK, Naumov VG, Shachkin LV. Quantum Electron 2008; 38:165.
- [17] Schwarz J, Meteva K, Grigat A, Schubnov A, Metev S, Vollertsen F. Diamond Relat Mater 2005; 14:305.
- [18] Varnin VP, Laptev VA, Ralchenko VG. Inorg Mater 2006; 42:S1.
- [19] Weerasinghe VM, West DRF, de Damborenea J. J Mater Process Technol 1996; 58:79.
- [20] Kato A, Tamari N. J Cryst Growth 1975; 29:55.
- [21] Kurtz SR, Gordon RG. Thin Solid Films 1986; 140:277.
- [22] Wu HZ, Chou TC, Mishra A, Anderson DR, Lampert JK, Gujrathi SC. Thin Solid Films 1990; 191:55.

# CHARACTERIZATION OF TITANIUM NITRIDE FORMED VIA LASER-SUSTAINED PLASMA INTERACTION WITHOUT DIRECT IRRADIATION OF THE SUBSTRATE

*A. N. Black, S. M. Copley and J. A. Todd*

Engineering Science and Mechanics Department, Penn State, University Park, PA, 16802, USA

Industries ranging from aerospace to biomedical utilize titanium and its alloys due to their superior strength, high strength-to-weight ratio, low density, high melting point, excellent corrosion resistance, high fracture toughness, good heat transfer properties, gold appearance, and biocompatibility [1, 2]. The poor tribological characteristics of these metals, however, reduce their applicability under severe wear conditions [3]. To enhance these properties, titanium nitride (TiN) coatings are often employed due to their extreme hardness, excellent corrosion and wear resistances, high thermal conductivity, important transport properties, chemical inertness, and gold appearance [4]. Thus, TiN is commonly used for protective coatings on cutting tools and drill bits, diffusion barriers in microelectronics, metal smelting crucibles, optical coatings, and decorative features [5].

Laser nitriding is a process in which laser irradiation melts a titanium surface while under a nitrogen-containing atmosphere. It has been investigated since the 1980s because of its potential as a fast, effective TiN synthesis technique [6]. During laser nitriding, the interaction of the laser melt and species evaporated from the surface produces near-surface plasma. The impact of this laser-induced plasma is a subject of much discussion; some consider it to enhance the coating process [7-9], others say it is detrimental to nitridation [10, 11], while most ignore its potential effects [12-14]. The research to be presented investigates the effect of plasma on a Ti surface without direct laser melting by utilizing laser-sustained plasma (LSP).

LSP, originally referred to as a “continuous optical discharge” is plasma generated by a laser beam in a gaseous atmosphere that can be sustained indefinitely away from any potentially interacting surface [15]. While LSP has been successfully used to deposit diamond [16-18], its potential contributions to the formation of a broad range of hard coating compositions has not been systematically explored. LSP is an optical discharge plasma, similar to a laser-induced plasma. While this optical discharge plasma can be used to melt a surface, it also provides a novel method for studying the influence of plasma on a Ti substrate without the laser beam interacting directly with the surface.

There is an important distinction between the experimental process being presented and conventional laser nitriding. In laser nitriding, the main heat source responsible for melting is the laser beam. In the process under consideration, LSP is the heat source responsible for melting the titanium

substrate. The term LSP nitriding is used to indicate that LSP, and not the laser, is being used as the heat source. The laser is used only to maintain the LSP and does not have any direct interaction with the material being nitrided.

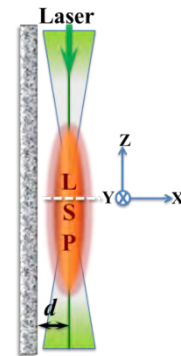


*Figure 1: A side view of the experimental setup showing  $d$ , the distance between the laser centerline (indicated by the green line) and substrate surface. The size and shape of the LSP are shown schematically. The green arrow indicates the direction of the laser beam, while the white, dashed line indicates the location of the laser's focal plane.*

In order to melt the surface without irradiating it, the LSP is translated to a location some distance,  $d$ , from the substrate, as shown in Figure 1. In all cases, it was determined there was no effect from the laser beam on the substrate without the LSP being present. Values for  $d$  tested were between 2 mm and 5 mm. Each distance produced a different melt pattern, as shown in Figure 2. These tests were performed on ASTM grade 2, commercially pure (< 99.5%) titanium plates. Some were processed with the as-received, unpolished, milled surface, while others were polished mechanically prior to LSP exposure. In addition, length of exposure was considered.

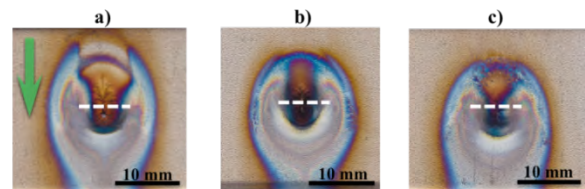


*Figure 2: Macroscale images for the LSP parallel configuration after 5 seconds at: a)  $d = 2$  mm; b)  $d = 2.5$  mm; and c)  $d = 3$  mm.*

During processing, images were collected via a CCD camera with appropriate filters to minimize oversaturation and modified frame-grabbing software, so processing could be visually monitored (see Figure 3). Scanning electron microscopy (SEM) with a backscattered electron (BSE) detector and energy-dispersive x-ray spectroscopy (EDS) were utilized to analyze the initial products of the process, as well as transverse and longitudinal metallographic cross-sections.

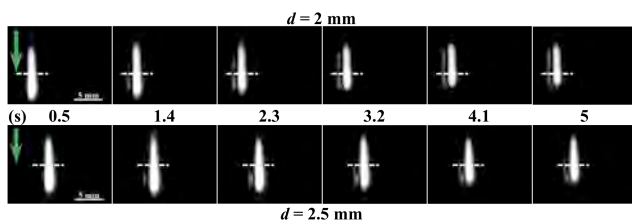


Figure 3: Progression of growth as seen through a 870 nm bandpass filter with 0.6 neutral density filter. The brightest portion of each image shows the LSP with the plate to the left. The green arrows indicate the direction of the laser beam, while the white, dashed lines indicates the location of the laser's focal plane.

Using EDS results in conjunction with the macroscale images seen in Figure 2 and previous literature on nitriding, it was determined that hypo-stoichiometric, near-stoichiometric [19], and hyper-stoichiometric [20] TiN developed at the main impact site. Also present were regions of TiO<sub>2</sub> [21] and locations where a nanoscale layer of TiO<sub>2</sub> covered a deeper layer of TiN [22].

Surface morphologies varied widely between the three values for  $d$  tested.  $d = 3$  mm showed little structure, while the  $d = 2$  mm and  $d = 2.5$  mm samples showed more mature crystallization and evidence of evaporative growth. Cross-sections showed solid and dendritic layers very similar to those seen in laser nitrided TiN. It was also noted that convection assists the permeation of nitrogen into the titanium melt, similar to the convective currents found in laser nitriding.

In addition to SEM and EDS, a focused ion beam was used to take cross-sections of the crystals on the surface for transmission electron microscope (TEM) examination. Diffraction indicates a deformed cubic structure, while electron energy loss spectroscopy (EELS) showed that the crystals have low levels of oxygen which may cause the deformation of the lattice and indicate that the crystals grow while the surface is cooling after the LSP was extinguished.

The regions of high nitrogen concentration, the convective movement within the melt pool, and the surface growth are the most significant structures seen in the LSP nitrided Ti. The faceted crystal growth on the surface and the dendritic layer below it suggest that there are two growth mechanisms

at work during LSP nitriding: one in the melt and another from the vapor.

**Word Count: 868**

- [1] Caron RN and Staley JT. Titanium and Titanium Alloys, in: Dieter GE (Ed.). ASM Handbook, vol. 20. Materials Park, OH: ASM International; 1997.
- [2] Zhang J, Fan D, Sun Y, Zheng Y. Key Eng Mater 2007; 353-358:1745.
- [3] Guo B, Zhou J, Zhang S, Huidi Z, Pu Y, Chen J. Mater Sci Eng A 2008;480:404.
- [4] Tavares J, Coulombe S, Meunier J-L. J Phys D: Appl Phys 2009;42:1020011.
- [5] Wu M. J Alloys Compd 2009; 486:223.
- [6] Spies H-J. Surf Eng 2010; 26:126.
- [7] Akarapu RK, Dua P, Campbell A, Scott D, Nassar A, Todd JA, Copley SM. Proc Mater Res Soc Symp 2007; 1040:Q08.
- [8] Höche D, Rapin G, Kaspar J, Shinn M, Schaaf P. Appl Surf Sci 2007; 253:8041.
- [9] Thomann AL, Sicard E, Boulmer-Leborgne C, Vivien C, Hermann J, Andreazza-Vignolle C, Andreazza P, Meneau C. Surf Coat Technol 1997; 97:448.
- [10] Chen X, Wu G, Wang R, Guo W, Yang J, Cao S, Wang Y, Han W. Surf Coat Technol 2007; 201:4843.
- [11] Kloosterman AB. Surface Modification of Titanium with Lasers. Groningen: Groningen University Press; 1998.
- [12] Jianglong L, Qiquan L, Zhirong Z. Surf Coat Technol 1993; 57:191.
- [13] Raaif M, El-Hossary FM, Negm NZ, Khalil SM, Kolitsch A, Höche D, Kaspar J, Mändl S, Schaaf P. J Phys D: Appl Phys 2008; 41:085208.
- [14] Mridna S, Baker TN. J Mater Process Technol 1998; 77:115.
- [15] Keefer D. Laser-Induced Plasmas and Applications. Radziemski LJ, Cremers DA (Ed.). New York, NY: Marcel Dekker, Inc.; 1989.
- [16] Bolshakov AP, Konov VI, Vostrikov VG, Dubrovskii VY, Kosyrev FK, Naumov VG, Shachkin LV. Quantum Electron 2008; 38:165.
- [17] Schwarz J, Meteva K, Grigat A, Schubnov A, Metev S, Vollertsen F. Diamond Relat Mater 2005; 14:305.
- [18] Varnin VP, Laptev VA, Ralchenko VG. Inorg Mater 2006; 42:S1.
- [19] Weerasinghe VM, West DRF, de Damborenea J. J Mater Process Technol 1996; 58:79.
- [20] Kato A, Tamari N. J Cryst Growth 1975; 29:55.
- [21] Kurtz SR, Gordon RG. Thin Solid Films 1986; 140:277.
- [22] Wu HZ, Chou TC, Mishra A, Anderson DR, Lampert JK, Gujrathi SC. Thin Solid Films 1990; 191:55.

## FROM LAB TO CLINIC: A MICROFLUIDIC BASED FULLY INTEGRATED ON-CHIP FLOW CYTOMETER.

*Ahmad Ahsan NAWAZ, Xiaole Mao, Sz-Chin Steven Lin, Michael Lapsley, Yanhui Zhao and Tony Jun Huang.*

Engineering Science and Mechanics Department, Penn State, PA-16802, USA

Flow cytometry is widely used to rapidly and quantitatively analyze biological samples such as blood cells, tumor cells, bio-particles or even DNA molecules.<sup>1-7</sup> To perform this analysis, the particles in the sample are passed in a single-file line through an optical detection region, where a focused laser beam interrogates each particle. The resulting scattered light and fluorescence emissions are collected by detectors and analyzed in order to provide valuable information about the sample, such as the size, complexity, and health of cells. Due to its ability to rapidly analyze heterogeneous samples at rates of up to several thousand cells per second, flow cytometry has many applications in the fields of immunology, cancer biology, and clinical diagnostics.<sup>10</sup> For example, in HIV diagnostics, flow cytometry is used to monitor levels of CD4+ T lymphocytes; this information is used to determine the progression of the disease and develop effective treatments. Although flow cytometry has proven to be an extremely powerful tool for the analysis of biological samples, the high cost of these devices, along with their mechanical complexity and bulky nature, has greatly limited their use in point-of-care diagnostic applications. In addition, specialized personnel are required to operate flow cytometers and multiple sample pre-treatment steps are often necessary, resulting in significant operational costs.

After having computationally and experimentally optimizing our 3D hydrodynamic focusing via curved microfluidic channel, in this research work we have taken a major step towards moving our research into clinical studies. As shown in equation 1,  $(D_1 - D_0)$  is the decrease in thickness of the sample flow in the Y direction, which directly results from the interfacial shear rate and is proportional to the elongation of the sample flow along the axial direction of the channel;  $\beta$  is the material parameter of the sample flow, similar to the Passions ratio, and dependent on liquid properties of sample flow such as viscosity and density;  $\dot{\gamma}$  is the interfacial shear rate which depends on the velocity difference between sample flow and sheath flow;  $t_0$  is the initial time at the inlet when two co-flowing fluids interact;  $t$  is the co-flowing time or the time of the shearing action applied on the interface of the two co-flowing fluids;  $U_v$  is the velocity of the vertical sheath flow;  $U_s$  is the velocity of the sample flow;  $a$  is the average thickness of the sample flow; and  $(L_1 - L_0)$  indicates the stretched length (elongation) of the co-flow interface.

$$(D_1 - D_0) \propto \int_{t_0}^t \beta \dot{\gamma} dt \propto \int_{t_0}^t \beta \left( \frac{U_v - U_s}{a} \right) dt \propto \beta (L_1 - L_0), \quad (1)$$

Figure 1 is the heart of the prototype flow cytometer, showing a fully integrated microfluidic based flow cytometer. The 3D hydrodynamic focusing is attained by utilizing the phenomenon of “microfluidic drifting”<sup>8</sup> within the curved microfluidic channel. This is achieved in a two-step procedure as shown in Figure 1. Presently we have one laser integrated into the chip via single mode optical fiber and three detection fibers for forward scattering, side scattering and fluorescent scatter.

In the second part of this work, we aimed to install everything inside a box to move towards prototyping out flow cytometer. The microfluidic chip is installed inside the box shown in figure 2: A Prototype of a fully functional flow cytometer. The prototype flow cytometer is the first step from lab to clinical use of this work. Moreover, our aim is to show a fully functional low cost, simpler, smaller and easy-to-use flow cytometer.

**Word Count: 547**

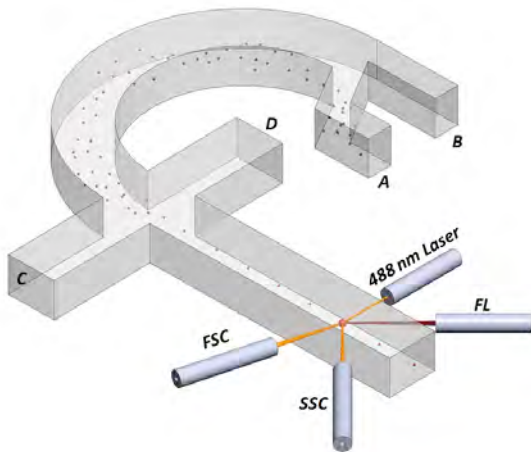


Figure 1: A fully integrated microfluidic flow cytometry device. The device has one input fiber that shines 488nm laser onto the cells of flowing inside the chip. Three detection fibers detect scattering signals.



Figure 2: Phase I prototype of a fully functional flow cytometer with customizable PMT voltages (LCDs). The heart of the flow cytometer, microfluidic 3D cell focusing device, is installed inside the upper compartment of the prototype.

## REFERENCES:

- 1 D. W. Inglis, J. A. Davis, T. J. Zieziulewicz, D. A. Lawrence, R. H. Austin and J. C. Sturm, *J. Immuno. Methods*, 2008, **329**, 151–156.
- 2 D. W. Inglis, K. J. Morton, J. A. Davis, T. J. Zieziulewicz, D. A. Lawrence, R. H. Austin and J. C. Sturm, *Lab Chip*, 2008, **8**, 925–931.
- 3 O. D. Laerum, T. Farsund, *Cytometry Part A*, 1981, **2**, 1-13.
- 4 H. M. Shapiro, R. C. Leif. *Practical flow cytometry*: Wiley-Liss New York, 2003.
- 5 M. Brown, C. Wittwer, *Clin.chem.* 2000, **46**, 1221-1229.
- 6 P. K. Dagur, A. Biancotto, L. Wei, H. N. Sen, M. Yao, W. Strober, R. B. Nussenblatt, and J. P. McCoy, Jr., *J. Autoimmun.* 2011, **37**, 319-327.
- 7 X. Cai, G. Pacheco-Rodriguez, Q. Y. Fan, M. Haughey, L. Samsel, S. El-Chemaly, H. P. Wu, J. P. McCoy, W. K. Steagall, J. P. Lin, T. N. Darling, and J. Moss, *Am. J. Respir. Crit. Care Med.* 2010, **182**, 1410-1418.
- 8 X. Mao, A. A. Nawaz, S. C. S. Lin, M. I. Lapsley, Y. Zhao, J. P. McCoy, W. S. El-Deiry, and T. J. Huang, *Biomicrofluidics*, 2012, **6**, 024113.